UNIVERSITY OF CALIFORNIA

SANTA CRUZ

CHIP SCALE OPTOFLUIDIC DEVICES

A dissertation submitted in partial satisfaction
of the requirements for the degree of

DOCTOR OF PHILOSOPHY

in

ELECTRICAL ENGINEERING

by

Jennifer Black

December 2018

The Dissertation of Jennifer Black
is approved by:

_____
Professor Holger Schmidt, chair

_____
Professor Marco Rolandi

_____
Professor Ali Yanik

_____

Lori Kletzer
Vice Provost and Dean of Graduate Studies

Table of Contents

List of Figures

List of Tables

Abstract

CHIP SCALE OPTOFLUIDICS

by

Jennifer Black

Within this dissertation, several optofluidic devices are presented for applications in atom-optics and on-chip biosensing. Oxide-based optofluidic devices compatible with alkali vapors designed for all-optical atomic cooling and for slow and stopped light based photonic devices are presented. Also presented are polydimethylsiloxane-based optofluidic devices with single virus detection sensitivities. By controlling the liquid flow characteristics through such polydimethylsiloxane optofluidic devices, chip-based detection of single viruses is enhanced using hydrodynamic focusing and velocity multiplexing is demonstrated using a stacked-channel design. Lastly, a novel on-chip distributed feedback dye laser is presented which is fabricated with an integrated fluidic detection channel.

Acknowledgements

First, I wish to thank my advisor, Dr. Holger Schmidt, for his infinite patience and continued support through the years. Much of our group's work is collaborative and I'd like to thank Dr. Aaron Hawkins for his support and collaboration. My committee has been very supportive as well and I am grateful to Dr. Ali Yanik and Dr. Marco Rolandi for their guidance, useful discussions and helpful feedback.

I am so unbelievably grateful to the peers I have had the pleasure to interact with over my years as a graduate student. Thanks for all the useful professional feedback and discussions. Thank you also for non-work related chats at the water cooler, coffee breaks, climbing dates, hiking trips in the Sierra, meals and bike rides along the Pacific coast. Santa Cruz is such a gorgeous place and the community within and outside of the University has been a nurturing place for me to grow. I appreciate all the people that I have met and fostered friendships with within the community. My family, though many miles away, has been unendingly supportive of this seemingly strange endeavor. Thank you for all your unconditional love and support. Lastly, I wish to thank my very best friend, Dr. Jonathan Bruce.

Chapter 1

Introduction

Optofluidics is an interdisciplinary field which is comprised of optics and microfluidics [1]. Light-matter interactions with fluids (e.g. liquids and vapors) have long been of interest across many fields long before experimental demonstrations of coherent light. However, with the advent of lasers and semiconductor technologies, spectroscopy and microfabrication techniques became more precise and readily available. As a result of the development of microfabrication techniques, chip-scale optical waveguides and microfluidics have become relatively simple to fabricate. Separately, chip-scale waveguides and microfluidic channels allow precise control of photons and fluids on a small scale. Eventually, these technologies merged on-chip with increased interest in full “lab-on-chip” devices [2]. Initially, optofluidic devices focused on photonic applications [3] and since then, both chemical and biological detection [4] and energy applications [5] have additionally flourished. This dissertation focuses on chip-scale optofluidic devices for light-matter interactions with atomic vapors [6], [7], on-chip biosensing [8], [9] and integrated coherent sources.

Optical interactions with alkali vapors are appealing on a chip-scale due to a small overall footprint as well as the small modes employed in optical waveguides. Such small optical modes allow high intensities to be achieved with low powers and for non-linear regimes to be reached far more easily than in free space. Optofluidics is also well suited for biological detection of single particles on-chip thanks to the integration of chip-scale optical waveguides with fluidic channels. Using on-chip light sources is appealing for the creation of a full lab-on-chip platform. This document describes several oxide- and polydimethylsiloxane-based optofluidic devices with applications suitable for applications in atom optics as well as on-chip biosensing.

First, this thesis presents an all-optical approach to atomic cooling based on an inhomogeneous AC Stark shift. Using this approach, two oxide-based chip designs are described for the all-optical cooling of Sodium atoms to speeds comparable to Zeeman slowers. Additionally, oxide-based device designs are presented for integrated atom filled waveguides for the creation of photonic devices and a novel perforated hollow waveguide for quick filling of devices with alkali vapor is discussed. Two all-polymer optofluidic devices are presented for on-chip biosensing with single virus sensitivity. These devices improve on current designs by enhancing the optical collection efficiency off-chip using hydrodynamic focusing and by implementing velocity and spectral multiplexing for particle discrimination. Lastly, a novel on-chip distributed feedback dye laser is presented using Rhodamine 6G in a corrugated sidewall microfluidic channel.

Chapter 2 presents a theoretical framework and relevant background information necessary for the discussion of the devices mentioned above. Section 2.1 focuses on the atom-optics applications and section 2.2 discusses on-chip biosensing and on-chip dye lasers. A discussion of leaky optical waveguides is presented in Chapter 3 and discusses the theoretical losses present in both capillary and anti-resonant reflecting optical waveguides in which light is guided through a low-index core medium. Additionally, section 3.3 presents an overview of the fabrication steps necessary for both types of leaky optical waveguides. Chapter 4 presents the atom-optics designs for alkali vapors and includes a discussion on the challenges of fabricating such devices. Chapter 5 discusses two polydimethylsiloxane-based optofluidic devices for the enhanced and multiplexed detection of single fluorescently labelled viruses. Chapter 6 presented a novel on-chip distributed feedback dye laser using a corrugated sidewall structure. Lastly, Chapter 7 summarizes the work presented within this text and discusses future goals for such optofluidic devices.

Chapter 2

Background

The aim of this chapter is to describe relevant background as the framework for the text to follow. This chapter is broken into two parts describing pertinent theory, previous work and motivation for atom-optics and biosensing applications.

2.1 On-Chip Atom Optics

Long before the advent of the laser, vapors were studied with incoherent light [10]. Lasers, however, have allowed for very precise spectroscopy [11], [12] and time keeping [13]. Alkali vapors are an appealing candidate for many light-matter interactions due to their relatively large absorption cross section [14]. Many interesting light-matter interactions have been demonstrated with bulk glass cells filled with alkali vapors in free space including: slow [15] and stopped [16] light, precise detection of magnetic fields [17], observation of quantum states [18], and precision metrology (including the most precise time keeping devices known to man) [19]. Many of these applications require or benefit from the cooling of atoms due to the decrease in Doppler broadening. These advances would not be possible without the realization that atoms could be cooled with lasers [20], [21], [22]. Therefore, with the advent of the laser, atomic spectroscopy proceeded to advance rapidly.

Modern interest has been given to the shrinking of such experiments in order to provide not only a smaller footprint but also to allow for the use of smaller optical powers or to achieve high intensities over long distances to investigate non-linear effects [23], [24]. There have been several approaches to miniaturizing these experiments in both small cells for use in free space [25], [26], [27] and with optical waveguides [28], [29], [30], [31]. Both chip-scale and optical fiber waveguide applications have been demonstrated both with evanescent fields [28], [30] and with hollow waveguides filled with the vapor [29], [32]. Alkali filled waveguides allow all of the guided mode to interact with the vapor, but it has proven difficult to fill such devices with vapor as the atoms themselves attach to the walls of the device and therefore take a large amount of time to fill ("ripening") [33], [34]. This will be discussed further in Chapter 4 in regards to the devices presented here. Evanescent field interaction with atoms eliminate the requirement that vapors fill a tight channel, but only a portion of their mode will guide in (and thereby interact with) the vapor.

This thesis presents an all-optical approach to atomic cooling and designs are presented for on-chip cooling of Sodium atoms using anti-resonant reflecting optical waveguides as an example of the method. Also presented herein is a device layout for the creation of photonic devices which utilize electromagnetically induced slow and stopped light in alkali vapors. This chapter provides a discussion of the hyperfine energy structure of two alkali vapors of interest (sodium and rubidium), radiation pressure, atomic cooling approaches, and electromagnetically induced transparency.

2.1.1 Fine and Hyperfine Structure

Within an atom, an orbiting electron will produce a magnetic moment from its loop current with a corresponding orbital angular momentum, $\vec{L}$. The electron itself also carries an intrinsic spin angular momentum, $\vec{S}$. These two angular momenta may couple ("spin-orbit" coupling) which results in an internal lifting of degeneracies (Zeeman splitting) which is known as the fine structure. The total angular momentum that results from this spin-orbit coupling is denoted $\vec{J} = \vec{L} + \vec{S}$ and may have a magnitude, J which lies within $|L - S| \leq J \leq |L + S|$. Alkali atoms like sodium (Na) and rubidium (Rb) (which we will be concerned with in the text) all have one electron outside of their other filled shells. Therefore, they behave similarly to hydrogen with one large core and a single orbiting electron in the outer shell. Their ground states have $L = 0$ and $S = 1/2 = J$. The first excited state has $L = 1$ and S= $1/2$, leaving two possibilities for $J = 1/2\ ,3/2$.

An atomic energy level is described by its principle quantum number, angular momentum and spin. The nomenclature used to describe the ground state for Na would be written as: $3^2S_{1/2}$ where the first number is the principle quantum number of the outer shell electron and the superscript is called the term which is given by: $2S' + 1$ where here $S' = \sum_i s_i$ is the sum of the spin for each electron in the system. The 'S' corresponds to the angular momentum where each L value has an indicator letter: $L = 0,1,2,3,4 \rightarrow S, P, D, F, G$ [35].

The hyperfine structure then goes a step further and describes the more closely spaced energy levels which result from the coupling of $\vec{J}$ and the total nuclear angular momentum, $\vec{I}$. The resulting total atomic angular momentum is then given by $\vec{F} = \vec{J} + \vec{I}$ and has values lying within $|J - I| \leq F \leq |J + I|$. Na has one stable isotope, ^{23}Na [36] which has $I = 3/2$, so its ground state ($L = 0, S = 1/2$) has $F = 1, 2$. Its excited states have either $L = 0, 1$ ($3^2P_{1/2}$, $3^2P_{3/2}$) and are known as the D_1 and D_2 levels and transitions respectively. The associated wavelengths for the ^{23}Na transitions are 589.6 nm for D_1 and 589.2 nm for D_2. Rubidium, however, has two naturally occurring isotopes, ^{87}Rb [37] and ^{85}Rb [38] which appear with abundances of 72.17 and 27.83 % respectively. Their D_1 and D_2 wavelengths are near 795.0 and 780.2 nm, respectively. The hyperfine transitions for ^{23}N a can be found in Fig. 2.1. The ^{87}Rb and ^{85}Rb isotope hyperfine transitions are seen in Fig. 2.2. Interest in light-matter interactions with alkali vapors have resulted in the availability of narrow linewidth diode laser sources at the relevant wavelengths. Light-matter interactions with the hyperfine structures of Na and Rb will be integral to the discussion presented in Chapter 4.

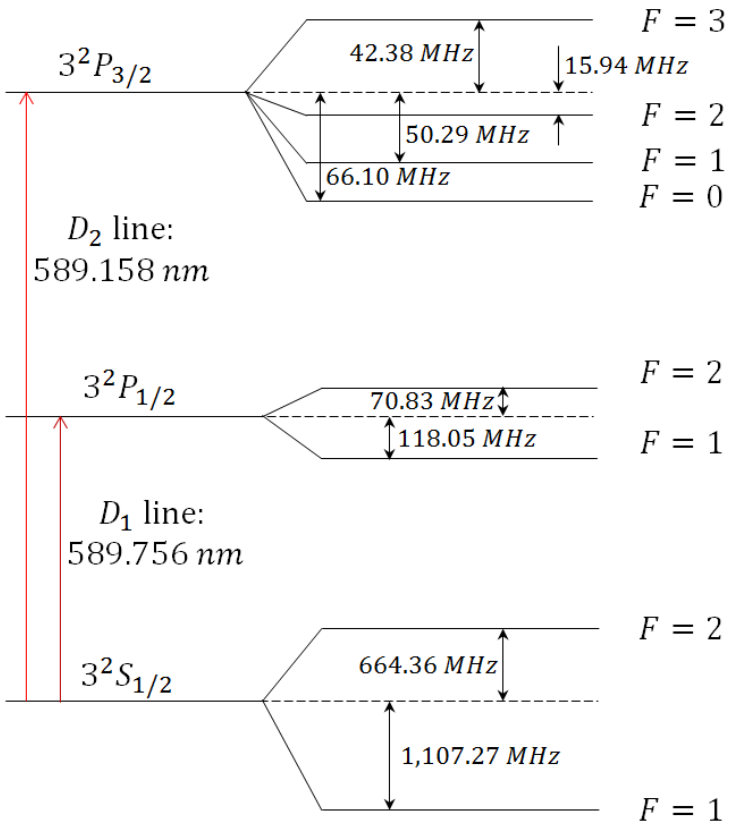

Fig. 2.1 The $\boldsymbol{D_1}$ and $\boldsymbol{D_2}$ hyperfine structure of ^{23}Na. Not drawn to scale.

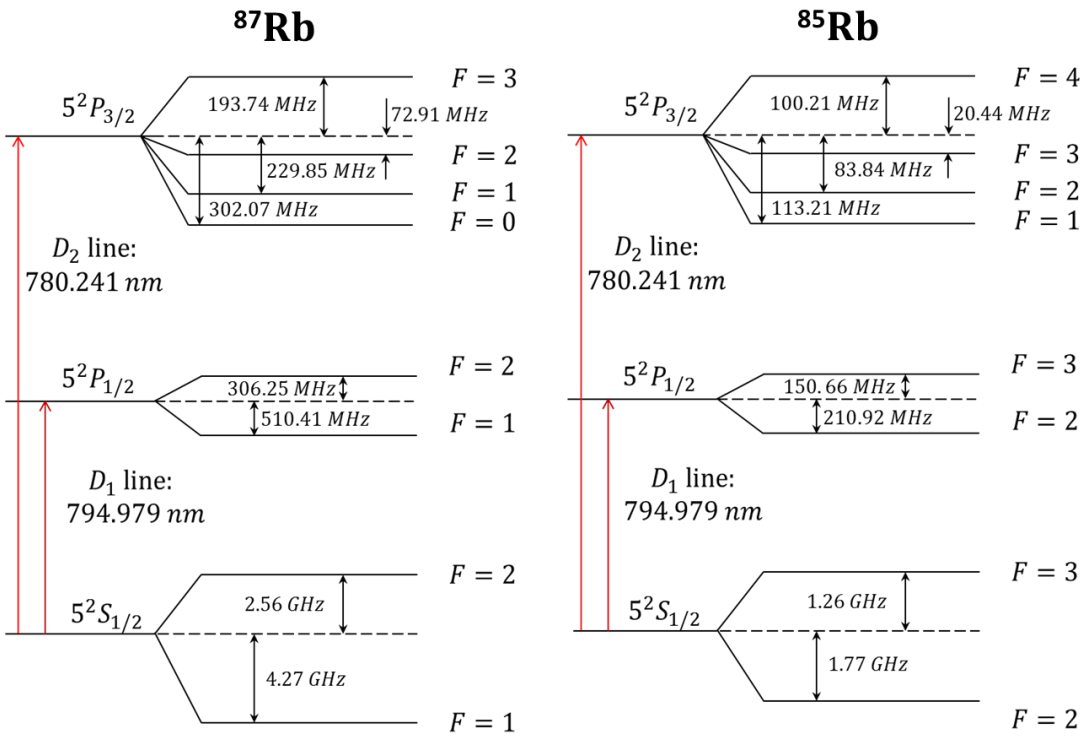

Fig. 2.2 The $\boldsymbol{D_1}$ and $\boldsymbol{D_2}$ hyperfine structure of ^{87}Rb (left) and ^{85}Rb (right). Not drawn to scale.

2.1.2 Radiation Pressure

Over many cycles of absorption and emission of photons (scattering), conservation of momentum results in a pressure exerted on an atom [22]. Consider an atom that is counter-propagating with a laser (as seen in Fig. 2.3) whose wavevector is $k = \frac{2\pi}{\lambda} = |\vec{\boldsymbol{k}}|$ where λ is the laser's wavelength. If λ appears near an atomic resonance, then a photon can be absorbed by the atom and through conservation of momentum, the atom's new momentum is given by $mv - \hbar k$ where m is the atom's mass, v is the atom's speed and $\hbar$ is the reduced Plank's constant. Consequently, the

atom decelerates and is then able to spontaneously emit a photon which again results in a momentum change of magnitude $\hbar k$. The net change in momentum from isotropic spontaneous emission over many scattering cycles is zero, thus allowing for the atom to decelerate.

Fig. 2.3 If a counter-propagating photon with momentum $\hbar\vec{\boldsymbol{k}}$ appears on resonance to an atom with momentum $\boldsymbol{m\vec{v}}$, the photon is absorbed and the resulting atomic momentum is $\boldsymbol{mv} - \hbar\boldsymbol{k}$.

The change in momentum after a cycle of absorption and emission results in a change in velocity known as the recoil velocity and is given by $v_r = \frac{\hbar k}{m}$. A ^{23}Na atom absorbing light near its D_2 hyperfine resonance, $\lambda = 589.16$ nm, has $m = 0.3818$ x 10^{-25} kg thereby resulting in a recoil velocity of v_r =2.9461 cm/s. This change in velocity may seem quite small, but an atom is able to absorb many photons over a short period of time. The rate at which an atom can go through this scattering cycle is aptly named the scattering rate and is given by [36]:

$$R = \left(\frac{\Gamma}{2}\right)\frac{\left(I/I_{sat}\right)}{1 + 4\left(\Delta/\Gamma\right)^2 + \left(I/I_{sat}\right)} \qquad (2.1)$$

Where Γ is the lifetime of an atomic transition, $\Delta = \omega_L - \omega_o$ is the detuning of angular frequency of the laser, ω_L, from resonance, ω_o, I is the intensity of the light and I_{sat} the saturation intensity given by equation (2.2).

$$I_{sat} = \frac{c\varepsilon_o \Gamma^2 \hbar^2}{4|\hat{\varepsilon} \cdot \vec{\mu}|^2} \quad (2.2)$$

Where c is the speed of light, ε_o is the permittivity of free space, $\hat{\varepsilon}$ is the polarization unit vector and $\vec{\mu}$ is the atomic dipole moment for the relevant transition. When a high intensity beam is present ($I \gg I_{sat}$), the scattering rate (2.1) goes to $\frac{\Gamma}{2}$. The magnitude of deceleration of an atom due to this scattering process is $a = \frac{|\Delta \vec{p}|}{m\Delta t} = \frac{\hbar R}{m\lambda}$ which goes to $\frac{\hbar \Gamma}{2m\lambda}$ in the saturated limit. For the ^{23}Na D_2 hyperfine transitions, the magnitude of saturation limited deceleration is $9.0643 \times 10^5 \frac{m}{s^2}$.

The mean speed and temperature of an atom are related by equation (2.3):

$$v = \sqrt{\frac{8k_B T}{\pi m}} \quad (2.3)$$

Where k_B is the Boltzmann constant and T is the atom's temperature in Kelvin. From equation (2.3), ^{23}Na isotopes near room temperature (T ~ 300 K) have a mean velocity of 525.6 m/s. In order to slow them to a final velocity of 10 m/s, the ^{23}Na atoms must absorb $N = \frac{(525.6-10)\, m/s}{v_r} \approx 1.75 \times 10^4$ photons which in the saturated limit will take 0.54 ms. Using the Galilean equations of motion, the necessary length, L, to cool the atoms from room temperature to a speed of 10 m/s can be determined: $L = \frac{(10\, m/s)^2 - (525.6\, m/s)^2}{-2*(9.0643 \times 10^5\, m/s^2)} = 15.23$ cm. Thus, the length necessary for the slowing of ^{23}Na atoms to speeds of tens of meters per second are achievable on the chip scale (~ centimeters). Some relevant atomic parameters for ^{23}Na and both Rb isotopes can be found in appendix A [36].

An important point not discussed above is that there is equal probability that a spontaneously emitted photon will be emitted in any one of three dimensions. For cooling, we ideally want all re-emitted photons to cool the atom (emit in one direction only). Therefore, there is a probability (~ 2/3) of the recoil velocity vector's direction happening in the (unwanted) transverse direction. Over time, the recoil velocity will increase in the transverse direction and the average speed picked up transversely will be $\langle v \rangle = \frac{2Nv_R}{3}$. As the final cooling velocity is typically much smaller than the initial velocity we can write $\langle v \rangle = v_o - v_f \approx v_o = \sqrt{\frac{8k_BT}{\pi m}}$. Relating the man speed equations, one finds that $N \propto \sqrt{m}$. The relationship between mean speed and the atom's mass is then $\langle v \rangle \propto m^{-1/2}$. Therefore, transverse heating is more pronounced when dealing with heavier atoms. To prohibit transverse cooling, a system of cooling beams can be used (e.g. six beams, two of which are counter-propagating for each of the three spatial dimensions).

Alternatively, a gradient force can be utilized to prohibit transverse cooling. Consider the cross section of a tightly collimated Gaussian laser beam. The center of the beam contains the highest intensity which decreases radially from the center of the beam. An energy level shift analogous to the Zeeman shift exists for electric fields. This intensity dependent shift is known as the AC Stark shift and does not saturate with intensity [36]. Therefore, in a Gaussian laser beam, there is a spatially varying intensity profile and thus a varying AC Stark shift which provides a force across the gradient of the intensity profile. Thereby, a potential well or hill can be

created within the laser beam depending on the sign of the detuning. Red-detuned light creates a potential well ($\Delta E < 0$) and blue-detuned light creates a potential hill ($\Delta E > 0$) as seen in Fig. 2.4.a. Thus, the gradient force can be used to confine atoms to move along the direction parallel with the collimated laser and prevent transverse de-collimation if a red-shifted beam is used as seen in Fig. 2.4.b. Conversely, atoms can be pushed away from a blue-shifted beam as seen in 2.4.c [20]. The gradient force is very effective in waveguides due to the ability to sustain large gradients (small beam diameters) over long distances.

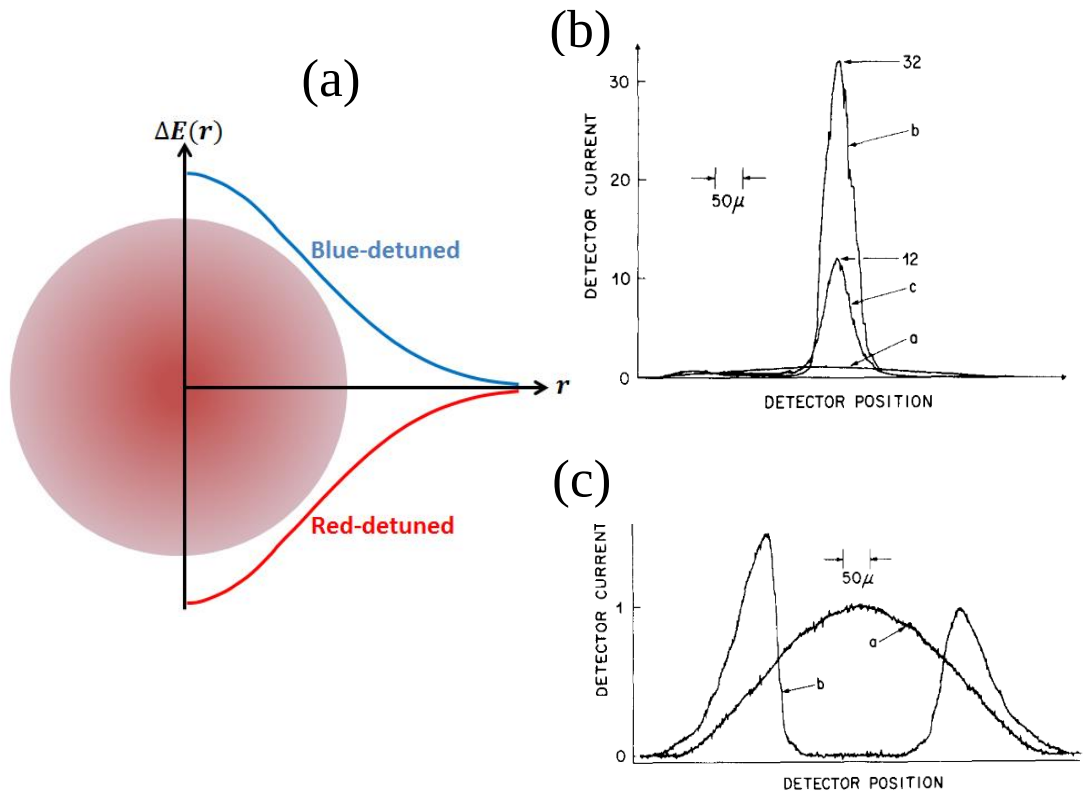

Fig. 2.4 (a) Radial dependence of the AC Stark shift ($\Delta \boldsymbol{E}(\boldsymbol{r})$) for a blue- and red-detuned laser. (b) Increased atomic concentration is demonstrated with a red-detuned laser for varying powers. “a”, “b” and “c” correspond to optical powers of 0, 250 and

25 mW respectively. (c) Atom repulsion is demonstrated with a blue-detuned laser with optical powers of 0 and 160 mW ("a" and "b"). Both (b) and (c) taken from [20].

2.1.3 Approaches to Atomic Cooling

A laser with fixed frequency in the lab's rest frame has a wavevector, $\vec{k}$. If this laser is counter-propagating with an atom traveling with a velocity, $\vec{v}$, then the laser's frequency will appear Doppler shifted to the atom. The amount of detuning perceived by the atom is given by: $\Delta = \delta_L - \vec{k} \cdot \vec{v}$ where δ_L is the detuning of the laser from an atomic resonance in the lab reference frame. The Doppler shift is given by $-\vec{k} \cdot \vec{v}$. The previous section of this chapter described how scattering cycles can be used to slow atoms [39]. However, in order for the atom to be able to absorb the atoms as it cools, the laser must continue to appear near resonance. Consider a laser which is locked to an atomic resonance for the ^{23}Na isotope ($\delta_L = 0\,MHz$). If the laser is counter-propagating with the atom's motion, it will appear blue shifted to the atom because $\vec{k} \cdot \vec{v} < 0$. Therefore, as seen in Fig. 2.5, one must lock the laser frequency, ω_L to be red-detuned by the appropriate Doppler shift ($-\vec{k} \cdot \vec{v}$) in order to make the laser appear on resonance.

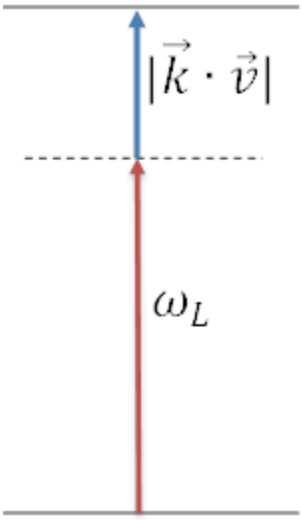

Fig. 2.5 A counter-propagating laser can be absorbed if it is red-detuned by the appropriate Doppler shift, thus making it appear on resonance.

Since a ^{23}Na atom near room temperature has a speed of ~ 500 m/s, a non-negligible Doppler shift is produced (~ $2\pi \cdot 0.9$ GHz) and therefore the Doppler cooling laser must be red shifted in the lab frame ($\delta_L < 0$) in order to compensate for this perceived shift. Now the atom may absorb the light, but as it cools, the laser offset will no longer match the cooled atom's Doppler shift and will be unable to absorb additional photons. Therefore, continuous adjustment of the detuning is necessary. One common approach to remedy this dynamic Doppler shift when cooling atoms is to use Zeeman assisted cooling.

Zeeman assisted cooling uses a fixed frequency Doppler cooling beam and a spatially varying magnetic field [39], [40]. The Doppler cooling beam can be fixed to resonance or offset in the lab reference frame. The spatially varied magnetic field produces a varied Zeeman shift along the direction of motion of the atom in order to

compensate for the dynamic Doppler shift as the atom cools. As described above, a laser locked to resonance in the lab reference frame will appear blue shifted to a counter-propagating atom as seen in Fig. 2.6 (a). If a magnetic field is present, it will provide a Zeeman shift of the ground state (ΔE) which can be used to compensate for the blue shift and allow the atom to absorb the photon as seen in Fig. 2.5 (b).

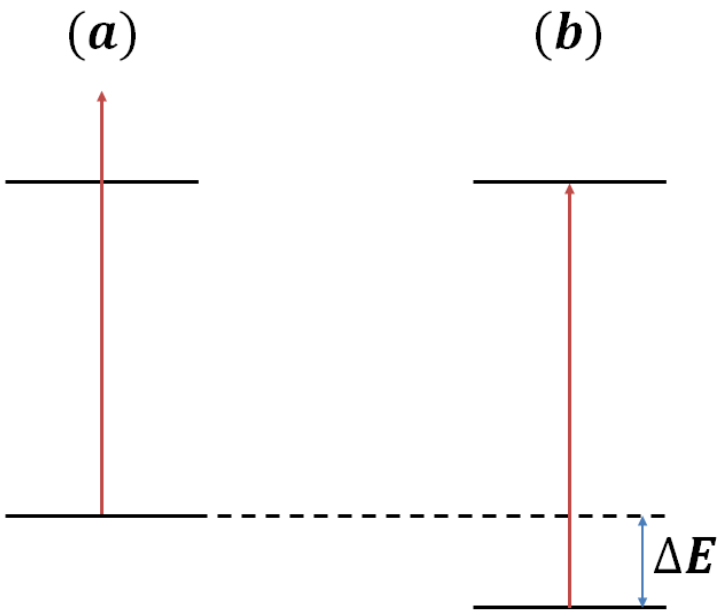

Fig. 2.6 (a) A laser locked to resonance in the lab reference frame appears blue-shifted by a counter-propagating atom and therefore is not absorbed. (b) A magnetic field is present which Zeeman shifts the ground state by ΔE resulting in the laser appearing resonant and allowing the atom to absorb a photon.

For a single speed and a fixed frequency laser, the appropriate Zeeman shift can be calculated in order to provide absorption of photons. However, as the atom cools, the Doppler shift changes and to keep the atom absorbing photons, the Zeeman shift must change as well. To provide such an inhomogeneous magnetic field, an

intricate solenoid is constructed with a varied number of coils along the direction of deceleration (z-direction). To determine the appropriate magnetic field profile, the Doppler shift along the z-direction must be determined. The deceleration due to constant absorption of photons in the saturated limit is given by $|\vec{\mathrm{a}}| = \frac{h\Gamma}{2m\lambda}$ as described in section 2.1.2 and the velocity along the z-direction is $v(\mathrm{z}) = \sqrt{{v_\mathrm{o}}^2 + 2\mathrm{az}}$ where v_o is determined by the initial temperature of the atoms (equation (2.3)). Therefore, the Doppler shift can be written as:

$$\Delta \mathrm{E_D}(\mathrm{z}) = \frac{h}{\lambda} v(\mathrm{z}) = \frac{h}{\lambda}\sqrt{{v_\mathrm{o}}^2 + 2\mathrm{az}} \quad (2.4)$$

The necessary Zeeman shift (ΔE_Z) must satisfy the following condition in order to ensure constant deceleration:

$$\Delta E_Z(z) + \Delta E_\mathrm{D}(z) = 0 \quad (2.5)$$

The linear Zeeman shift can be found using the interaction Hamiltonian:

$$H_{int} = \vec{\mu} \cdot \vec{B} = \frac{\mu_B}{\hbar}\left(g_L \vec{L} + g_S \vec{S} + g_I \vec{I}\right) \cdot \vec{B} \quad (2.6)$$

Where μ_B is the Bohr magneton, g_L, g_S and g_I are the electron orbital, spin and nuclear Landé g-factors respectively. Taking the magnetic field to be along the z-direction we can write:

$$H_{int} = \frac{\mu_B}{\hbar}(g_L L_z + g_S S_z + g_I I_z)B = \frac{\mu_B}{\hbar}(g_F F_z)B \quad (2.7)$$

Where $B \equiv \left|\overrightarrow{B(z)}\right|$ and $F = J + I = L + S + I$ (see section 2.1.1). Using first order perturbation theory, we can find the Zeeman light shift via [41]:

$$\Delta E_Z = \langle F, m_F | H_{int} | F, m_F \rangle = \frac{\mu_B}{\hbar} g_F B \langle F, m_F | F_z | F, m_F \rangle = \mu_B g_F m_F B \quad (2.8)$$

Using this along with equation (2.4) and (2.5), the magnetic field along z must take the following form:

$$B(z) = \frac{-h}{\lambda \mu_B g_F m_F} \sqrt{{v_o}^2 + 2az} \quad (2.9)$$

Now that the magnetic field profile is specified, one must construct such a field. Using the Biot-Savart Law, one can determine the number of loops the wire must make along the slowing axis within a step along z thus defining the shape of the taper the solenoid must make along z. A cartoon of such a Zeeman slower is shown in Fig. 2.7 after [42].

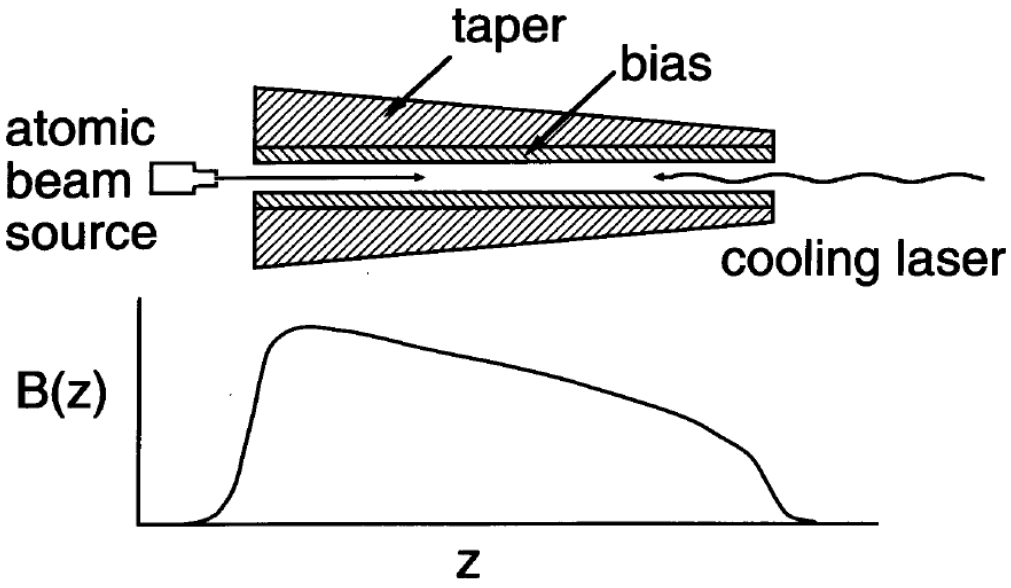

Fig. 2.7 A schematic of a typical Zeeman slower along with the corresponding inhomogeneous magnetic field along the direction of cooling, z. From ref [42].

Another method for Doppler cooling involves the chirping of the cooling beam. This means that the cooling beam's frequency is shifted in time in order to

compensate for the dynamic Doppler shift. In this orientation, the beam is originally red-shifted to match the initial Doppler shift and then the beam is chirped to increasingly higher frequencies in order to keep it on resonance as the atom cools. If the laser is chirped at a high enough rate then the atoms at different velocities will see an on resonance photon and can cool. Results from [43] are shown in Fig. 2.8 for a chirping experiment with varying scanning rates. Later chirping experiments resulted in stopped (and even reversing velocity) atoms [44].

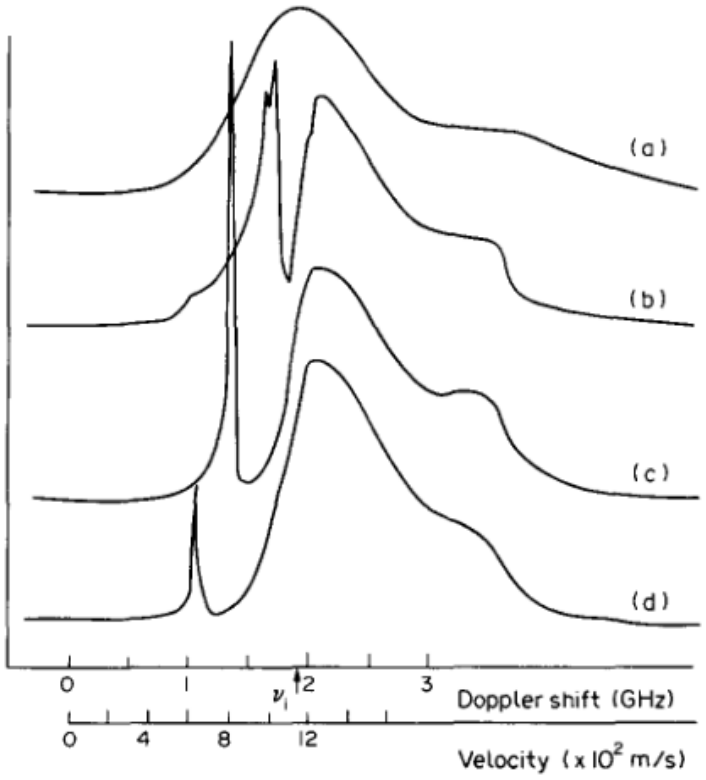

Fig. 2.8 Na atom velocity distributions for (a) no cooling laser, (b) cooling laser with no chirp, (c) chirped at 480 MHz and (d) chirped at 750 MHz. From [43].

In Chapter 4 a new approach to atomic cooling will be presented. This approach can be implemented on-chip and two designs are presented to cool ^{23}Na atoms to speeds comparable to those with Zeeman cooling.

2.1.4 Electromagnetically Induced Transparency

Electromagnetically induced transparency (EIT) is a quantum interference effect which arises in a three level atomic system [45]. The so-called lambda (Λ) energy level system can be seen in Fig. 2.9. The probe laser (angular frequency, ω_p) is detuned from the $|1> \rightarrow |3>$ by $\Delta_p = \omega_{31} - \omega_p$. In the absence of the coupling laser (angular frequency, ω_c) the probe beam would be absorbed near resonance ($\Delta_p = 0\ MHz$) resulting in a Lorentzian lineshape in the absence of Doppler broadening. Considering the effects of Doppler broadening, one would expect to see a Voigt profile (Lorentzian lineshape integrated over the Gaussian Maxwell-Boltzmann distribution [46]). However, in the presence of a strong coupling beam, transparency of the probe beam occurs at two-photon resonance, $\delta \equiv (\Delta_p - \Delta_c) = \omega_{31} - \omega_p - (\omega_{32} - \omega_c) = -\omega_p + \omega_c + \omega_{21}$ thanks to interference between the transition amplitude pathways.

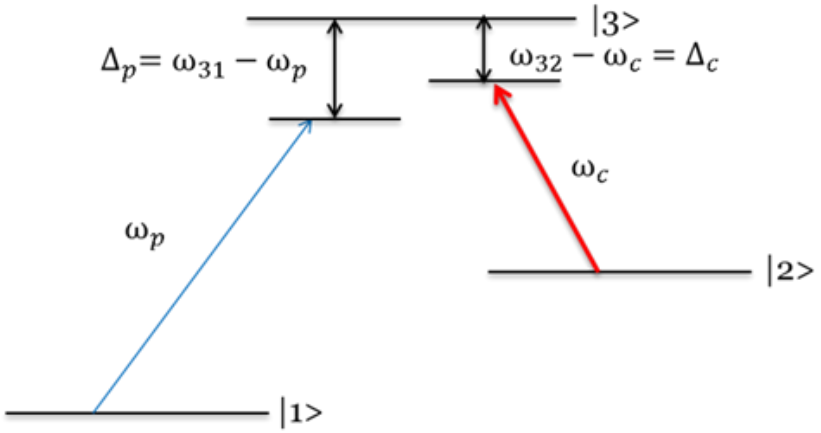

Fig. 2.9 Lambda energy level scheme. Energy levels $|\mathbf{1}>$ and $|\mathbf{2}>$ share a common excited state $|\mathbf{3}>$ and the transition between levels $|\mathbf{1}>$ and $|\mathbf{2}>$ are dipole forbidden. Two lasers co-propagate through the three level medium. The probe (coupling) beam has angular frequency $\boldsymbol{\omega_p}$ ($\boldsymbol{\omega_c}$) near resonance with the $|\mathbf{1}> - |\mathbf{3}>$ ($|\mathbf{2}> - |\mathbf{3}>$) transition. For EIT, the coupling beam has much higher intensity than the probe beam and through quantum interference of transition amplitudes the probe beam is rendered transparent on resonance.

To arrive at the expressions which describe EIT, we begin with the time-dependent Schrödinger equation:

$$i\hbar\frac{\partial}{\partial t}|\psi> = H|\psi> \qquad (2.10)$$

Which describes the atom's wavefunction, ψ, in response to the Hamiltonian operator, H ($\hbar$ is the reduced Planck constant). The Hamiltonian for the system can be written $H = H_o + V$ where the bare atom Hamiltonian, $H_o = \hbar\begin{pmatrix} 0 & 0 & 0 \\ 0 & \omega_{21} & 0 \\ 0 & 0 & \omega_{31} \end{pmatrix}$ (taking the ground state to be zero energy) and V is due to the applied probe and coupling electric fields. Using the Dipole approximation ($\lambda \gg$ atomic radius) $V \approx -\mu_{ab} \cdot E_{ab}$ where μ_{ab} is the dipole moment between two energy levels and E_{ab} is the

electric field applied near resonance between levels a and b. $\mu_{ab} = 0$ for a = b and here for ab = 13 (i.e. ab = 13 is dipole forbidden). Thus,

$$V = -\begin{pmatrix} 0 & 0 & \mu_{13} \cdot E_p \\ 0 & 0 & \mu_{23} \cdot E_c \\ \mu_{31} \cdot {E_p}^* & \mu_{32} \cdot {E_c}^* & 0 \end{pmatrix} \quad (2.11)$$

Where ${E_i}^*$ is the complex conjugate of $E_i = E_i \cos(\omega_i t) = \frac{E_i}{2}\left(e^{-i\omega_i t} + e^{i\omega_i t}\right)$ (i = c, p (coupling, probe beam)) and $\mu_{32} = {\mu_{23}}^*$. Introducing the Rabi frequency, $\Omega_i \equiv \frac{\mu E_i}{\hbar}$ [47], the Hamiltonian can be re-written:

$$H = \hbar\begin{pmatrix} 0 & 0 & -\frac{\Omega_p}{2}(e^{i\omega_p t} + e^{-i\omega_p t}) \\ 0 & \omega_{21} & -\frac{\Omega_c}{2}(e^{i\omega_c t} + e^{-i\omega_c t}) \\ -\frac{{\Omega_p}^*}{2}(e^{-i\omega_p t} + e^{i\omega_p t}) & -\frac{{\Omega_c}^*}{2}(e^{-i\omega_c t} + e^{i\omega_c t}) & \omega_{31} \end{pmatrix} (2.12)$$

Now, a rotating frame [35] of the probe beam can be assumed via the unitary transformation:

$$U = \begin{pmatrix} 1 & 0 & 0 \\ 0 & e^{-i(\omega_p - \omega_c)t} & 0 \\ 0 & 0 & e^{-i\omega_p t} \end{pmatrix} \quad (2.13)$$

The new Hamiltonian in the rotating frame is given by $\widetilde{H} = U^\dagger H U - i\hbar U^\dagger \frac{\partial U}{\partial t}$ which is the typical transformation, $U^\dagger H U$, with an additional time dependent element, $i\hbar U^\dagger \frac{\partial U}{\partial t}$, because a non-inertial reference frame is assumed. This is derived by taking equation (2.10) and multiplying both sides by $U^\dagger$:

$$i\hbar U^{\dagger}\frac{\partial}{\partial t}(|\psi>) = U^{\dagger}H|\psi \quad (2.14)$$

Also, since $U^{\dagger}$ is unitary, we can insert the identity matrix expressed as $UU^{\dagger}$ before the state ket on either side:

$$i\hbar U^{\dagger}\frac{\partial}{\partial t}(UU^{\dagger}|\psi>) = U^{\dagger}HUU^{\dagger}|\psi> \quad (2.15)$$

Defining the new state vector in the rotating state as $\tilde{\psi}> \equiv U^{\dagger}|\psi>$, we can now write the above as:

$$i\hbar U^{\dagger}\frac{\partial}{\partial t}(\mathrm{U}|\tilde{\psi}>) = U^{\dagger}H\mathrm{U}|\tilde{\psi}> = i\hbar U^{\dagger}[\frac{\partial U}{\partial t}|\tilde{\psi}> +\mathrm{U}\frac{\partial|\tilde{\psi}>}{\partial t}] \quad (2.16)$$

Finally, after some rearranging:

$$i\hbar\frac{\partial}{\partial t}|\tilde{\psi}> = (U^{\dagger}HU - i\hbar U^{\dagger}\frac{\partial U}{\partial t})|\tilde{\psi}> \quad (2.17)$$

Comparing this to the time-dependent Schrödinger equation, an analogy in the rotating frame can be written as $i\hbar\frac{\partial}{\partial t}|\tilde{\psi}> = \tilde{H}|\tilde{\psi}>$ where $\tilde{H}$ is the modified effective Hamiltonian in the rotating frame. Now, using equation (2.17) with the original Hamiltonian, H (equation (2.11)) and the transformation matrix, U (equation (2.12)), $\tilde{H}$ is found to be:

$$\tilde{H} = \hbar\begin{pmatrix} 0 & 0 & -\frac{\Omega_p e^{-i\omega_p t}}{2}\left(e^{i\omega_p t}+e^{-i\omega_p t}\right) \\ 0 & \omega_{21}-\omega_p+\omega_c & -\frac{\Omega_c e^{-i\omega_c t}}{2}\left(e^{i\omega_c t}+e^{-i\omega_c t}\right) \\ -\frac{{\Omega_p}^* e^{i\omega_p t}}{2}\left(e^{-i\omega_p t}+e^{i\omega_p t}\right) & -\frac{{\Omega_c}^* e^{i\omega_c t}}{2}\left(e^{-i\omega_c t}+e^{i\omega_c t}\right) & \omega_{31}-\omega_p \end{pmatrix}$$

$$= \hbar \begin{pmatrix} 0 & 0 & -\frac{\Omega_p}{2}(1 + e^{-2i\omega_p t}) \\ 0 & \delta & -\frac{\Omega_c}{2}(1 + e^{-2i\omega_c t}) \\ -\frac{\Omega_p{}^*}{2}(1 + e^{2i\omega_p t}) & -\frac{\Omega_c{}^*}{2}(1 + e^{2i\omega_c t}) & \Delta_p \end{pmatrix}$$

$$\approx \frac{\hbar}{2} \begin{pmatrix} 0 & 0 & -\Omega_p \\ 0 & 2\delta & -\Omega_c \\ -\Omega_p & -\Omega_c & 2\Delta_p \end{pmatrix} \quad (2.18)$$

Where, again, $\Delta_p = \omega_{31} - \omega_p$ is the detuning of the probe beam from the $|1> - |3>$ resonance and $\Delta_c = \omega_{21} - \omega_c$ is the detuning of the coupling beam from the $|1> - |2>$ resonance and $\delta = \omega_{21} - \omega_p + \omega_c$ is the two-photon detuning. The final expression uses the approximation that the probe and coupling beam are near resonance and thus $2\omega_p$ and $2\omega_c$ are largely detuned for this system and can be ignored.

Now $\tilde{H}$ can be used to find the electric susceptibility, χ, which describes how a medium responds to an electric field. χ is a complex expression whose real part is proportional to the index of refraction and its imaginary part is directly related to absorption as we'll see below. χ can be found either by solving the time dependent Schrodinger equation or via the Liouville equation (density matrix formalism).

The approach using the time dependent Schrödinger equation in the rotating frame takes the form:

$$i\hbar\frac{\partial}{\partial t}|\tilde{\psi}> = \tilde{H}|\tilde{\psi}> \quad (2.19)$$

Where $\tilde{\psi}$ is the atom's wavefunction in the rotating frame,

$$|\tilde{\psi}> \; = U^{\dagger}|\psi>. |\psi> = a(t)|1> \; + \mathrm{b(t)}e^{-i\omega_{21}t}|2> + \mathrm{c(t)}e^{-i\omega_{31}t}|3> \quad (2.20)$$

Which can be re-written in the rotating from as:

$$\tilde{\psi}> \; = U^{\dagger}|\psi> \equiv d(t)|1> \; + \; \mathrm{e(t)}|2> \; + \; \mathrm{f(t)}|3> \quad (2.21)$$

Plugging $\tilde{\psi}$ and $\tilde{H}$ into the Schrödinger equation and rearranging:

$$\begin{pmatrix} \dot{d(t)} \\ \dot{e(t)} \\ \dot{f(t)} \end{pmatrix} = i \begin{pmatrix} 0 & 0 & \frac{\Omega_p}{2} \\ 0 & -\tilde{\delta} & \frac{\Omega_c}{2} \\ \frac{\Omega_p}{2} & \frac{\Omega_c}{2} & -\widetilde{\Delta_p} \end{pmatrix} \begin{pmatrix} d(t) \\ e(t) \\ f(t) \end{pmatrix} \quad (2.22)$$

Where $\tilde{\delta} = \delta - i\frac{\Gamma_{21}}{2}$ and $\widetilde{\Delta_p} = \Delta_p - i\frac{\Gamma_{31}}{2}$ with Γ_{21} is the decoherence rate between the two ground states and Γ_{31} is the decay rate from the excited state. Note that Γ_{31} is a published value found experimentally (e.g. ^{87}Rb [37]) and Γ_{21} arises because of collisions and the limited interactions of the atoms with the laser (e.g. individual atoms within a gas will eventually leave the beam diameter at a rate dependent on the beam size and the atom speed if there is no buffer gas present. Even with a buffer gas, the atoms will eventually diffuse out of the laser). This decoherence rate can be decreased by the use of a buffer gas and wall coatings [48], [49].

Next, it's assumed that the electrons begin in the ground state (explicitly, $d(t) = 1$) and equation (2.22) is solved in the steady state ($\dot{e}(t) = \dot{f}(t) = 0$):

$$f(t) = \frac{2\Omega_p \tilde{\delta}}{4\tilde{\delta}\widetilde{\Delta_p} - {\Omega_c}^2} \quad (2.23)$$

This can be used to find the electric susceptibility through the relation:

$$P = \sum \frac{< \psi|\mu|\psi >}{V} = 2\varrho\mu_{31} f(t) = \varepsilon_o \chi E_o \quad (2.24)$$

Where ϱ is the density of the medium and μ_{31} is the dipole moment between the lower ground state and the excited state. Rearranging equation (2.24) for the electronic susceptibility:

$$\chi = \frac{4\varrho{\mu_{31}}^2 \tilde{\delta}}{\varepsilon_o \hbar(4\tilde{\delta}\widetilde{\Delta_p} - {\Omega_c}^2)} \quad (2.25)$$

Note that this is a complex value. Via several algebraic steps, one can separate the complex susceptibility into its real and imaginary parts:

$$Re(\chi) = \frac{4\varrho{\mu_{31}}^2}{\varepsilon_o \hbar}\left\{\frac{\delta\left(4\delta\Delta_p - \Gamma_{21}\Gamma_{31} - {\Omega_c}^2\right) - \Gamma_{21}\left(\Gamma_{31}\delta + \Gamma_{21}\Delta_p\right)}{\left(4\delta\Delta_p - \Gamma_{21}\Gamma_{31} - {\Omega_c}^2\right)^2 + 4\left(\Gamma_{31}\delta + \Gamma_{21}\Delta_p\right)^2}\right\} \quad (2.26)$$

$$Im(\chi) = \frac{4\varrho{\mu_{31}}^2}{\varepsilon_o \hbar}\left\{\frac{\frac{\Gamma_{21}}{2}\left(4\delta\Delta_p - \Gamma_{21}\Gamma_{31} - {\Omega_c}^2\right) + 2\delta(\Gamma_{31}\delta + \Gamma_{21}\Delta_p)}{(4\delta\Delta_p - \Gamma_{21}\Gamma_{31} - {\Omega_c}^2)^2 + 4(\Gamma_{31}\delta + \Gamma_{21}\Delta_p)^2}\right\} \quad (2.27)$$

As mentioned above, the significance of these expressions is related to observable quantities. The absorption coefficient (α) describes the amount of light absorbed as light propagates through a material (L is the length of propagation through the medium). The transmission (T) of optical intensity is given by the Beer-Lambert law:

$$T = e^{-\alpha L} \quad (2.28)$$

And the absorption coefficient is related to the electric susceptibility by [46]:

$$\alpha = k \cdot Im[\chi] \quad (2.29)$$

Where k is the wavenumber of the propagating light. It is important to remember that α is wavelength dependent.

The complex index of refraction is given by: $n' = \sqrt{1 + \chi} = n - i \cdot \kappa$

Where n is the real part of the refractive index (often referred to simply as "refractive index") and describes the phase velocity of light as it propagates through a material, $v = c/n$ where c is the speed of light. Since the electric susceptibility is complex then we can write the real part of the refractive index as:

$$n = \sqrt{1 + Re[\chi]} \quad (2.30)$$

κ is the imaginary part of the complex index of refraction and is called the extinction coefficient. The relationship between the extinction and absorption coefficients is given by:

$$\alpha = \frac{4\pi}{\lambda}\kappa \quad (2.31)$$

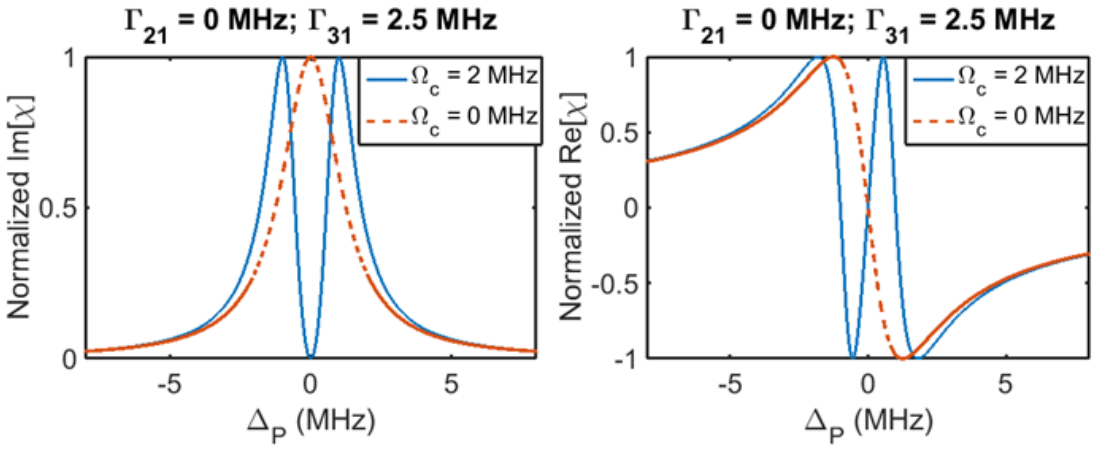

Fig. 2.10 Normalized plots for the imaginary and real parts of the electric susceptibility in the case without and with EIT (red and blue, respectively). The plots are formed from equations (2.26) and (2.27) with a coupling beam on resonance ($\Delta_C = 0$) and no decoherence ($\Gamma_{21} = 0\ MHz$). Without EIT (red curves) there is maximum absorption on resonance and a negative dispersion. With the application of a coupling beam (blue curves), EIT is present (dip in $Im[\chi]$) and a strong positive dispersion is created on resonance.

Therefore, the index of refraction is related to the real part of the electric susceptibility and the transmission through a material is dependent on the imaginary part of the electric susceptibility. Fig. 2.10 plots the normalized imaginary and real part of the electric susceptibility in the case of a single laser (no coupling beam; $\Omega_c = 0\ MHz$) and in the case of EIT ($\Gamma_{31} = 2.5\ MHz;\ \Omega_c = 2\ MHz$) from equations (2.26) and 2.27. This is the ideal case in which there is no decoherence ($\Gamma_{21} = 0\ MHz$). Notice the dip in the $Im[\chi]$ which experimentally results in a drop in absorption on resonance (Transmission at $\Delta_P = 0\ MHz$). Importantly, $Re[\chi]$ shows a steep positive

increase around resonance. Since $n = \sqrt{1 + Re[\chi]}$ then an increase in the index of refraction around resonance appears when $Re[\chi] > 0$. The group index describes the speed at which a pulse of light propagates through a material and is given by:

$$n_g = n(\omega) + \omega \frac{dn(\omega)}{d\omega} \quad (2.32)$$

Therefore n_g at a given frequency is dependent on the slope of the change of refractive index $\left(\frac{dn(\omega)}{d\omega}\right)$. As seen in Fig. 2.10, in the case of EIT, this term can be made extremely large ($n_g \gg 1$ [50]) resulting in a large group index. As mentioned above, the group index describes the speed at which a pulse of light propagates through a medium which is given by:

$$v_g = \frac{c}{n_g} \quad (2.33)$$

Thus, EIT provides not only transmission of light where normally it would be absorbed, but also results in the slowing of a pulse of light! Amazingly, if EIT is dynamically controlled while a pulse propagates through a slow light medium, the pulse can actually be stopped and later retrieved [51]. Let's consider the effect on the group index as a function of increasing coupling beam intensity ($\propto \Omega_c$). Fig. 2.11 plots the normalized imaginary and real part of the electric susceptibility for varying coupling beam Rabi frequencies ($\Omega_c = 0.5, 1, 3, 5\ MHz$) from equations (2.26) and 2.27. The results indicate that for increasing Ω_c, the width of the EIT transmission

(ΔT) window increases and n_g decreases (less slow light). Thus $\Delta T \propto \Omega_c$ and $n_g \propto 1/\Omega_c$.

Therefore, if Ω_c is decreased to 0 while the slowed pulse is propagating through the slow light medium then its group velocity will be driven to 0. The quantum information of the pulse is converted into the atomic medium as a spin wave (described by the so called "dark-state polariton" [52]). Experimentally, to achieve stored light, one needs only to vary the intensity of the co-propagating coupling laser beam in order to alter Ω_c [53], [16], [54], [55]. Chapter 4 presents experimental slow and stored light in bulk cell and designs for photonic devices in which EIT based slow and stopped light are utilized.

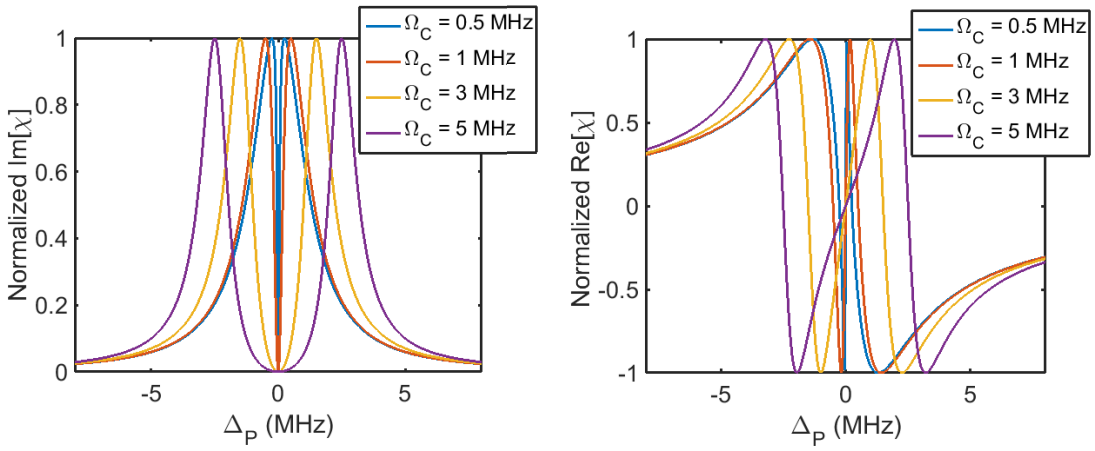

Fig. 2.11 Normalized plots for the imaginary and real parts of the electric susceptibility for different Rabi coupling frequencies: $\Omega_c = 0.5, 1, 3, 5\ MHz$ in blue, red, orange and purple respectively. As above, the plots are formed from equations (2.26) and (2.27) with a coupling beam on resonance ($\Delta_C = 0$) and no decoherence ($\Gamma_{21} = 0\ MHz$). With increased Ω_c, the EIT transparency window width is increased and the group index is decreased.

2.2 On-Chip Biosensing

Optofluidic devices have proven valuable tools for the detection of bioparticles. Detection of biological samples has long been carried out in bulk, but with the rise of microfluidics, smaller sample volumes can be used and a simpler approach to bulk experiments is available. Not only are small sample volumes used in microfluidics, but sample handling has been demonstrated by fluidic control techniques such as hydrodynamic focusing [56], mixing [57], droplet formation [58] and sorting [59]. Often detection takes place by monitoring a change in the refractive index of a liquid [4]. These experiments may utilize chip-based channels [60], [61], [62], photonic crystals [63], [64], Fabry-Perot interferometers [65], or plasmonic sensors [66], [67]. Surface enhanced Raman is also a popular technique for biological detection which has benefited from optofluidic architectures [68], [69]. Lastly, fluorescent detection of bioparticles has demonstrated single molecule sensitivities on-chip [70], [71].

Fully integrated bioassays have been demonstrated using silicon-dioxide and all-polymer based optofluidic devices [72], [8]. The devices work similar to a flow cytometer [73] in that fluorescent particles suspended within a liquid are pulled/pushed through a laser spot to produce light induced fluorescence. The devices introduce light to the fluidic channel which doubles as a leaky optical waveguide by intersecting the fluidic channel with a solid-core waveguide. Fluorescence is detected off-chip by collecting light from a perpendicularly intersecting solid-core waveguide. Further, the integration of multi-mode interference (MMI) waveguides allow a

method for multiplexing the detection of single particles [74], [75]. Integrating detection of particles on-chip provides a step towards a real lab-on-chip device which has all necessary components for an experiment on-chip. To that end, light sources have also been integrated on-chip [76], [77], [78], [79]. Dye-lasers lend well to the microfluidic platforms and have been demonstrated by using Bragg reflection [80], Fabry-Perot geometries [81] and via whispering gallery modes found in circular geometries (droplets [82] and resonators [83]).

This thesis presents two chip-scale all-polymer optofluidic devices which were used to detect single fluorescently labeled viruses. The first design utilizes hydrodynamic focusing to enhance the optical detection of single particles [8] and the second utilizes a liquid-core MMI waveguide which intersects two fluidic channels which was used to multiplex the detection of particles using velocity. Also, a distributed feedback on-chip dye laser is presented. Within this chapter, a discussion on laser induced fluorescence, multiplexing using MMI waveguides, hydrodynamic focusing and on-chip dye lasers is presented.

2.2.1 Laser Induced Fluorescence

Fluorescence is a form of photoluminescence [84] that has become useful in the detection of biological materials. When a photon excites an electron from a ground state (S_o) to an excited vibration singlet state (S_1 with vibrational levels 0, 1, 2, 3…), it may relax to the lowest vibration state (S_1, 0) as seen in Fig. 2.12. A photon is emitted as the electron relaxes back to the ground state. Since there is a change in

energy levels between the absorbed and emitted photon, there is a (Stokes) shift in the excitation and emission wavelengths. The emitted photon will have lower energy (red shifted). The lifetime of the process is on the order of nanoseconds.

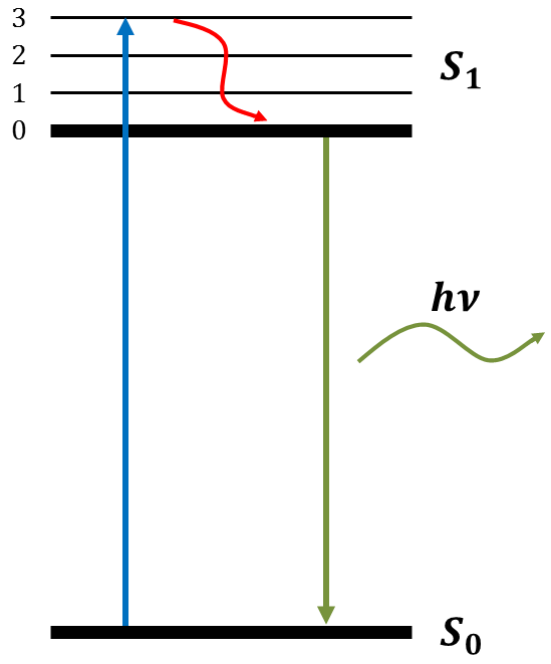

Fig. 2.12 Light is absorbed, moving electrons from the ground singlet state (S_0) to a vibrational excited singlet state ($S_1, 3$). Non-radiative decay moves the electron to the lowest vibrational excited singlet state ($S_1, 0$) and a photon is emitted (with energy, $h\nu$) at lower energy back to the ground state.

Molecules exist which fluoresce at many different wavelengths. These molecules are readily available commercially as dyes which can be used to stain fluorescently label particles (e.g. polystyrene beads, single viruses). These particles can then be detected by illuminating them with laser light and collecting their emitted wavelength. Due to the Stokes shift in absorbed and emitted wavelengths, the excitation light can be filtered. By selectively staining samples with different color

dyes, the presence of different species can be detected by monitoring their emission wavelengths. Commonly used dye molecules include cyanine, rhodamine, coumarin and xanthene. Table 2.1 summarizes some commonly used commercially available dyes in our lab with their excitation and emission wavelengths. Note that these dye absorption and emission bands can be relatively large (tens of nanometers) and the listed excitation and emission wavelengths are peak values.

Dye name	Excitation wavelength (nm)	Emission wavelength (nm)
Alexa Fluor 488	496	519
Cy3	554	568
Cy5	649	666
DyLight 550	562	576
DyLight 800	777	794

Table. 2.1 Several common fluorescent dye molecules used in the Applied Optics Group with their peak excitation and emission wavelengths.

2.2.2 Multi-mode Interference Waveguides

Consider the dielectric slab waveguide seen in Fig. 2.13 (a) with a core index of refraction larger than the cladding index of refraction ($n_1 > n_2$). Each mode which propagates within the waveguide will have a unique transverse (k_v) and parallel (β_v) wave vector component depending on the angle of propagation within the waveguide (where $k = 2\pi n_1/\lambda$). The number of modes (m) which may propagate within the waveguide can be expressed as [85]:

$$m \leq \frac{2V - \varphi}{\pi} \quad (2.34)$$

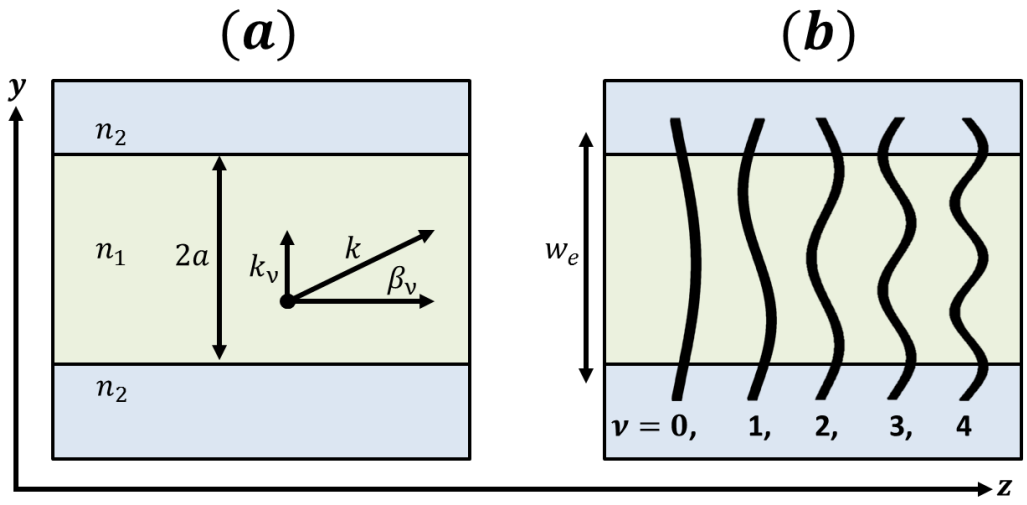

Fig. 2.13 (a) A symmetric slab waveguide with $n_1 > n_2$ with width of the core layer equal to $2a$. The propagating wavevector, $\vec{k}$ has transverse components $\overrightarrow{k_\nu}$ which lies along the y-direction with parallel components $\overrightarrow{\beta_\nu}$ in the z-direction where $\nu = 0, 1, 2, 3, \ldots$ for the multiple sustained modes (the number of which will propagate being determined by equation (2.34)). (b) Visualization of the propagation of multiple modes (ν) with effective width w_e.

Where φ is the phase shift acquired at the boundary of n_1 and n_2, which in the case of total internal reflection (TIR) cannot be larger than π. V is the so called "V-number" and is given by:

$$V = \left(\frac{2\pi a}{\lambda}\right)\sqrt{{n_1}^2 - {n_2}^2} \quad (2.35)$$

Now consider the structure shown in Fig. 2.10 (b) in which the slab waveguide is depicted which supports multiple modes ($\nu = 0, 1, 2, 3, 4$). The effective width (w_e) of the propagating modes is determined by the waveguide width (w) along

with the penetration depth of the modes and is approximated to be the same for each ν^{th} mode by [86]:

$$w_e \approx w + \left(\frac{\lambda}{\pi\sqrt{{n_1}^2 - {n_2}^2}}\right)\left(\frac{n_2}{n_1}\right)^{2\sigma} \quad (2.36)$$

Where $\sigma = 0, 1$ for TE, TM polarization respectively. The mode dependent propagation constants are given by (consider the geometry in Fig. 2.10 (a)):

$$\beta_\nu = \sqrt{k^2 - {k_\nu}^2} = k\sqrt{1 - \left({k_\nu}/{k}\right)^2} \approx k - \frac{{k_\nu}^2}{2k} \quad (2.37)$$

Where the first order bionomial expansion is used in the final step. Considering the total phase shift acquired for the ν^{th} mode within the effective width:

$$k_\nu = \frac{(\nu + 1)\pi}{w_e} \quad (2.38)$$

Which can be used to express the propagation constant as a function of the effective width:

$$\beta_\nu \approx k - \frac{(\nu + 1)^2\pi\lambda}{4n_1{w_e}^2} \quad (2.39)$$

Using equation (2.39), the beat length can be defined ($\equiv L_\pi$) between the two lowest order modes:

$$L_\pi = \frac{\pi}{\beta_0 - \beta_1} \approx \frac{4n_1{w_e}^2}{3\lambda} \quad (2.40)$$

An input optical field profile ($\Psi(y, 0)$) can be expressed as a summation of guided modes (assuming that it does not excite unguided modes):

$$\Psi(y, 0) = \sum_{\nu=0}^{m-1} c_\nu \psi_\nu(y) \quad (2.41)$$

Where c_ν are the orthogonal field excitation coefficients. The field profile at a distance z along the multi-mode waveguide can be written:

$$\Psi(y,z) = \sum_{\nu=0}^{m-1} c_\nu \psi_\nu(y)\, e^{i(\omega t - \beta_\nu z)} \quad (2.42)$$

This expression (equation (2.42)) can be re-written by assuming the fundamental mode phase is a common factor in the sum. If it is then dropped along with the implicit time dependence:

$$\Psi(y,z) = \sum_{\nu=0}^{m-1} c_\nu \psi_\nu(y)\, e^{[i(\beta_0 - \beta_\nu)z]} = \sum_{\nu=0}^{m-1} c_\nu \psi_\nu(y)\, e^{[i\frac{\nu(\nu+2)\pi}{3L_\pi}z]} \quad (2.43)$$

Where in the last step, we used the equation (2.40) for the beat length. The resulting field profile along z then depends on the mode phase factor:

$$e^{[i\frac{\nu(\nu+2)\pi}{3L_\pi}z]} \quad (2.44)$$

If equation (2.44) is equal to 1 then all the modes along z differ by integer multiples of 2π and therefore the input field profile is replicated. If instead equation (2.44) is equal to $(-1)^\nu$ then even (odd) modes will be in (out) of phase resulting in a mirrored image of the input field profile. To satisfy these conditions:

$$z = p(3L_\pi) \quad \text{where } p = 0, 1, 2 \ldots \quad (2.45)$$

So a single image (direct/mirrored if $p =$ even/odd) will be produced if equation (2.45) is satisfied. The pattern then is repeated along the length of the multi-mode interference (MMI) waveguide.

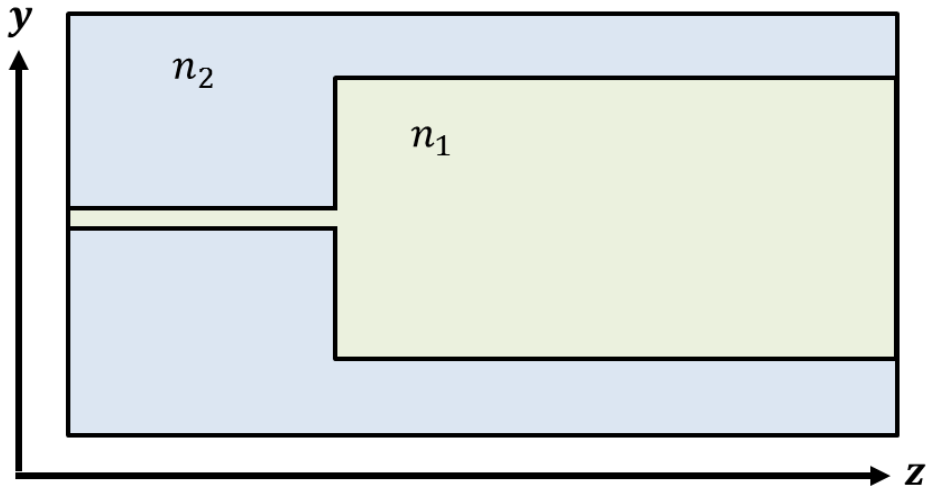

Fig. 2.14 Cartoon of a symmetric single input MMI waveguide structure. $n_1 > n_2$ and light propagates along the +z-direction. It's assumed that a single mode propagates in the narrow portion of the structure at lower values of z. The waveguide widens to support multiple modes further along the +z-direction. This structure behaves as described in equation (2.47).

The above discussion assumes arbitrary input position. However, the devices considered within this thesis are symmetric input MMI waveguides like the structure found in Fig. 2.14. The input field profile is determined by a symmetric input narrow waveguide (assumed to guide only the fundamental mode). In this case, it is found that N number of self-images will be found across w_e when:

$$z = L = \frac{3pL_\pi}{4N} = p\frac{{n_1}{w_e}^2}{N\lambda} \quad (2.46)$$

When designing such a waveguide, the shortest length device is often desirable and therefore the structure will be designed for $p = 0$. Therefore:

$$NL = \frac{{n_1}{w_e}^2}{\lambda} \quad (2.47)$$

Notice that according to equation (2.47), one may be able to design such a structure in which two separate wavelengths (λ) may result in two different integer values of N. Alternatively, for a single wavelength laser, different integer values of N spot patterns are created along the waveguide at different values of L. These properties of MMI waveguides have enabled up to six-fold multiplexing of fluorescently labelled viruses on an oxide-based optofluidic chip [74], [75]. In Chapter 5, a device is presented which uses a liquid-core MMI waveguide for two-fold multiplexing at a single wavelength using a stacked-channel design for velocity discrimination of particles.

2.2.3 Microfluidic Flow Dynamics

Microfluidics is a field in which fluids (vapors, liquids, plasmas) are confined in a small volume (less than a microliter). The confinement of fluids to small volumes allows for smaller sample consumption and a smaller overall device footprint. These aspects make microfluidics appealing for lab-on-chip technologies. Understanding fluid flow in such small geometries is crucial for developing useful on-chip devices. The devices discussed within this dissertation are comprised of small rectangular channels which are filled with vapors or liquids. The behavior of fluids in such channels differs from macroscale fluid dynamics. Often low Reynolds numbers are present which results in laminar flow of fluids [87]. The result of low Reynolds number flow (laminar) is that co-propagating fluids will not mix. By controlling the

flow dynamics in microfluidic channel arrays, sample handling can be precisely controlled on-chip.

The Reynolds number (Re) is important in fluid dynamics and describes the type of flow which is present in a fluidic channel. It is quantified by [87]:

$$Re = \frac{\rho v D}{\mu} \quad (2.48)$$

Where ρ, v, D and μ are the fluid density, mean speed, hydraulic diameter and dynamic viscosity, respectively. ρ and μ are fluid dependent and v and D depend on the device design and experimental parameters. For example, D depends on the channel geometry. For a circular channel, D is merely the diameter of the channel, but for a rectangular channel $D = \frac{2wh}{w+h}$ where w and h are the channel width and height respectively. Often in microfluidics, the flow speed (v) is controlled via positive pressure from a syringe pump which allows for programmable volumetric flow rates. Alternatively, negative pressure can be applied at an outlet thereby pulling the fluid through the channel. The devices presented later in the dissertation will use this negative pressure approach.

For a given pressure differential across a rectangular microfluidic channel, the average flow rate (Q) can be approximated. A circuit analogue model can be utilized to find the average flow rate by relating it to the pressure difference across the channel (ΔP) and a hydrodynamic resistance term, R:

$$Q = \frac{\Delta P}{R} \quad (2.49)$$

The hydrodynamic resistance term (R) for a rectangular channel can be found by:

$$R = \frac{12\mu L}{wh^3}\left\{1 - \frac{h}{w}\left[\frac{192}{\pi^5}\sum_{n=1,3,5\ldots}^{\infty}\frac{1}{n^5}\tanh\left(\frac{n\pi w}{2h}\right)\right]\right\}^{-1} \quad (2.50)$$

Where μ is the fluid viscosity, w, h, L are the channel width, height and length respectively. This equation assumes that the channel has a low aspect ratio meaning that $w \approx h$. The term in brackets is a geometric form factor specific to a low aspect ratio rectangular channel [88], [89]:

$$F = 1 - \frac{h}{w}\left[\frac{192}{\pi^5}\sum_{n=1,3,5\ldots}^{\infty}\frac{1}{n^5}\tanh\left(\frac{n\pi w}{2h}\right)\right] \quad (2.51)$$

To find this term for a given channel design, convergence is tested over the summation of equation (2.51). Notice that F is dependent only on the channel's cross-sectional dimensions (w and h). The length of the channel is considered when calculating the hydrodynamic resistance, R. For example, consider a rectangular channel with width and height, w and $h = 12\ \mu m\ x\ 6\ \mu m$ with channel length, $L = 1.7\ mm$. F is plotted for these dimensions across the sum of equation (2.51) as seen in Fig 2.15.

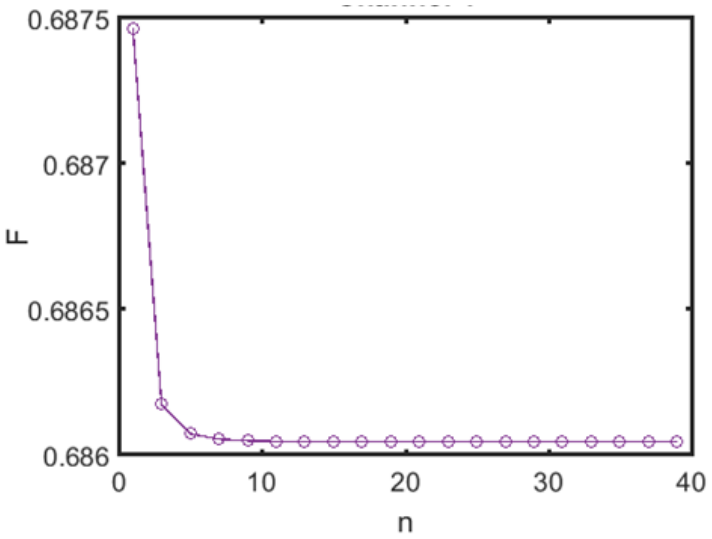

Fig. 2.15 The geometric form factor from equation (2.51) over the summation for a rectangular microfluidic structure with cross-sectional dimensions of $x\ h = 12\ \mu m\ x\ 6\ \mu m$.

From Fig 2.15, the geometric form factor is found for the example rectangular microfluidic channel to be $F(n = 39) = 0.6860$. Knowing F for the channel, the hydrodynamic resistance can be determined form the channel dimensions using equation (2.50): $R = \frac{12\eta L}{Fwh^3} = 1.147\ x\ 10^{16}\ \frac{Pa \cdot s}{m^3}$. The volumetric flow speed (Q) can be determined using equation (2.49) for a given pressure differential. As mentioned above, the devices of interest here use a negative pressure to induce flow in the channels. Experimentally, maximum negative pressures of -35 inHg are measured, resulting in a pressure differential (in Pascals) = $\Delta P = |-118523.6\ Pa - 101325\ Pa| = 219848.6\ Pa$. Therefore, using equation (2.49), $Q = 1.917\ x10^{-11}\ m^3/s$.

Lastly, the mean speed of the fluid traveling through the channel can be found by: $|v| = Q/A$ where $A = w \cdot h$. For our example device, $|v| = 26.62\ cm/s$. Calculating the Reynolds number using this speed (recall equation 2.48) in a water filled channel $\left(\rho = 1000\ {}^{kg}/_{m^3},\ \mu = 1\ x\ 10^{-3}\ {}^{kg}/_{m \cdot s}\right)$:

$$Re = 2.13$$

The transition from laminar to turbulent flow typically occurs around $Re = 2300$ [87], therefore for the channels considered within this dissertation, laminar flow is most definitely present. Laminar flow results in a parabolic velocity profile within the microfluidic channel where the flow speeds at the sidewalls are zero due to the no-slip condition. Speeds are at their maximum in the center of the channel and liquids co-propagating do not mix. Two streams of fluid introduced together into a single channel will not mix and at their boundary will introduce a shear force dependent on the relative flow speeds (and viscosities). This shear force has been usefully exploited to focus a single fluid within a single channel by pushing it toward the center using other flow streams to apply a shear force onto the fluid [90], [91], [56], [92]. This method is called hydrodynamic focusing (HDF) and has been used in many microfluidic applications including flow cytometry [93].

Focusing a fluid into a smaller cross section within the parabolic velocity profile present with laminar flow allows a smaller velocity distribution to exist for the focused fluid. Flow cytometry uses laser induced fluorescence to detect particles as they flow through the excitation beam. The resulting histogram of signal peak heights will have a normal distribution with finite width. The width of the normal distribution

will determine how precisely different particle species can be differentiated. By minimizing the speed distribution, the collected fluorescent signal heights will be more uniform and therefore particle discrimination will be more accurate. Both one- and two-dimensional HDF have been introduced on-chip to decrease the particle signal height histograms [91], [92], [90]. Chapter 5 presents a PDMS optofluidic device which uses one-dimensional HDF to enhance the detection of single viruses on-chip [8].

2.2.4 On-chip Dye Lasers

Dye lasers use fluorescent dye molecules to act as a gain medium. Due to the wide range of emission wavelengths available, a single pump laser can be used to create a host of tunable output wavelengths [94], [95]. The dye is typically dissolved in a solvent and the dye solution is flowed through the optical pump (typically a pulsed 532 nm laser. Continuous wave dye lasers are difficult to realize due to the evolution of common dyes into dark states [76]). As mentioned above, different types of cavities have been utilized to provide feedback including Fabry-Perot cavities [96], whispering gallery mode resonators (e.g. dye doped resonators [83], dye solution droplets [82], evanescent interaction in capillaries [78]) or Bragg gratings [97]. Both bulk and microfluidic approaches have been used to demonstrate lasing.

Waveguide based Bragg gratings have been used both in fiber and ridge waveguides to create wavelength specific reflectors as well as to provide feedback to create a laser cavity. These reflections are provided by a periodic variation in

refractive index as seen in Fig. 2.16 (a). The Fresnel coefficient can be calculated for each pass through one cycle in the period (length Λ), determining the amount of light reflected at that boundary. The more cycles of periodic refractive index that exist, the more reflections will occur over the length of the grating. Such periodic media can be used to create optical reflectors [98], tunable dispersion [99], [100], and lasers [101].

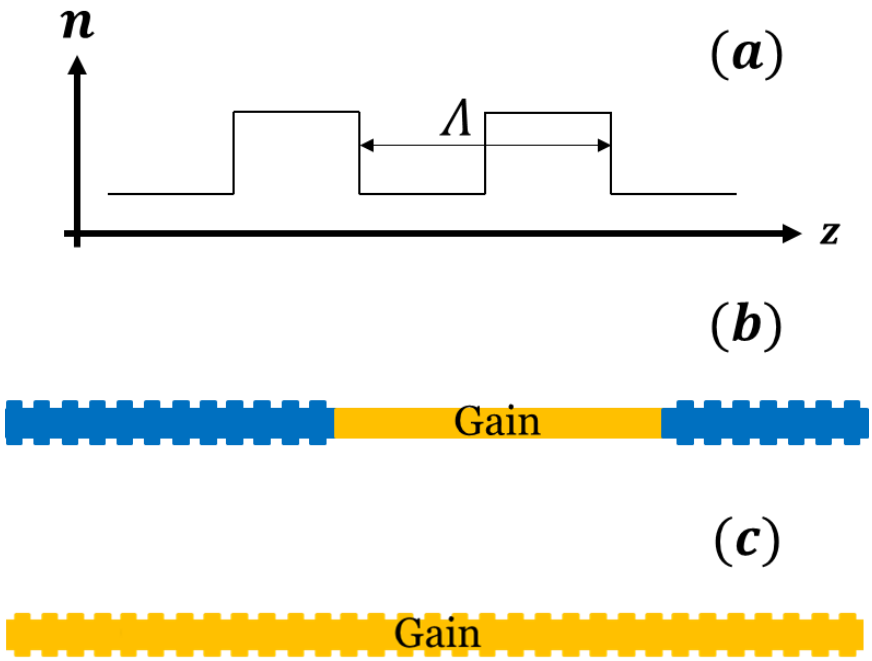

Fig. 2.16 (a) A variation in a structure's refractive index (n) along a spatial direction (z-direction) with characteristic Bragg spacing Λ. Due to the change in refractive index, light propagating along the z-direction will have some chance of reflection within each period Λ determined by the Fresnel equations. These reflections occur at specific wavelengths as described in equation (2.52). Such Bragg gratings can be used to create laser cavities. Distributed Bragg reflector lasers (DFB) (b) sandwich a gain medium (pictured in orange) between two structures with periodic index (e.g. a modulation in a waveguide width resulting in a variation in effective index of refraction) which act as wavelength specific mirrors. By tuning a single reflection within the gain emission profile, single mode lasing is possible. A variation in refractive index can also be introduced into the gain medium itself which provides reflections all along the length of the gain medium to induce lasing. Such a laser is called a distributed feedback laser (DFB) as pictured in (c).

The Bragg condition mathematically states that the total round-trip phase acquired over one period of the structure adds up in phase:

$$2n_{eff}\Lambda = m\lambda_m \quad (2.52)$$

Where n_{eff} is the effective index of the guided mode, Λ is the length of the periodic structure, m is an integer and λ_m are the m^{th} order resonant wavelengths. So, for a given period (Λ), there can be several resonant wavelengths for the structure with a spacing between subsequent resonant wavelengths (λ_m) called the free spectral range (FSR) which is given by:

$$FSR = 2n_{eff}\Lambda\left(\frac{1}{m-1} - \frac{1}{m}\right) \quad (2.53)$$

Larger periodicity in the variation in refractive index will result in larger m^{th} order for a fixed wavelength and a smaller *FSR* (more frequent resonances) which may or may not be desirable depending on the application. Consider attempting to create a first order structure ($m = 1$) resonant for a particular wavelength in the visible spectrum (say, 600 nm). Oxides are commonly employed in the fabrication of Bragg reflectors and have an index of refraction $n_{eff} \approx 1.5$. Therefore, a $\Lambda = 300$ nm structure would need to be fabricated to satisfy the Bragg condition. For standard UV photolithography, such resolution is not practical. Therefore, a patterning technique with higher resolution is required in order to fabricate a working device (e.g. electron beam lithography).

As mentioned above, such Bragg reflectors can be used to create lasers. There are two approaches towards integrating Bragg structures into a laser cavity.

Distributed Bragg reflector lasers (DBR) use a modulated index of refraction surrounding a gain medium in order to provide narrow wavelength resonances as seen in the cartoon in Fig. 2.16 (b). These resonances define the laser cavity operating modes and since the reflections are very narrow, these structures result in very controllable narrow wavelength output modes. Additionally, modulation of the structure (e.g. change in index of refraction via injection current) can result in high precision tunability. Second, distributed feedback lasers (DFB) use a modulation in the index of refraction *within* the gain medium (see Fig. 2.16 (c)) as opposed to sandwiching the gain medium between two Bragg mirrors. In this way, emission from the gain medium results in reflections all along the length of the periodic structure. Several examples of on-chip DFB dye lasers have been demonstrated in PDMS [77], [79]. In Chapter 5, we will discuss a novel DFB structure for on-chip dye lasers using PDMS.

Chapter 3

Leaky Optical Waveguides

This chapter presents a discussion on the theoretical optical losses in low index fluid filled leaky optical waveguides. Loss mechanisms in both capillaries and anti-resonant reflecting optical waveguides (ARROW) are discussed through sections 3.1 and 3.2, respectively. Section 3.3 presents a discussion on the fabrication of oxide- and PDMS-based optofluidic devices which utilize leaky optical waveguides.

Most often, waveguides make use of total internal reflection (TIR) to guide light. To use TIR, however, one needs a higher index of refraction in the core of the waveguide compared with the surrounding cladding layer [85]. This does not lend well to the applications previously described where one is interested in guiding light in a fluid. For alkali vapors, the index of refraction is around $n \approx 1$ and for liquids like water, the index of refraction is a bit higher, $n \approx 1.33$. This thesis focuses on devices which are formed of oxides ($n \approx 1.46$ or higher) or of a viscoelastic polymer, polydimethylsiloxane (PDMS) ($n \approx 1.42$). Thus, to guide light within the fluids of interest, TIR cannot be used. The losses associated with these structures are of great importance to creating a functional device with reasonable sensitivities.

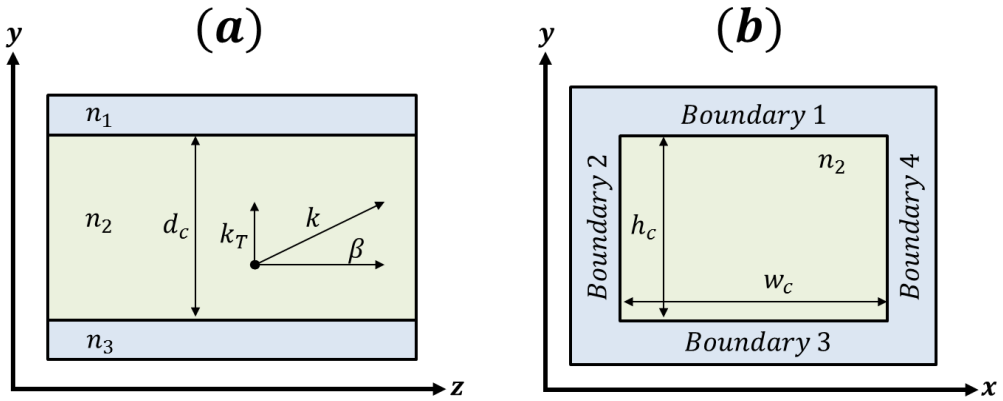

Fig. 3.1 (a) Three layer dielectric stack in which light is guided in the middle layer (index of refraction n_2) of thickness d_c. The surrounding layers have index of refraction n_1 and n_3. The propagating wavevector, k, have transverse and parallel components k_T and β, respectively. (b) 2D structure with core index of n_2 and cross-sectional dimensions $w_c \; x \; h_c$. The core is bounded on four sides (boundaries 1 – 4). To find the loss of the rectangular leaky optical waveguide, the reflectance at each of the four boundaries must be computed.

Consider a stack of three dielectrics as shown in Fig. 3.1 (a) in which light is guided within the middle layer. The propagating mode wavevector, k is comprised of a transverse component (k_T) and a parallel component along z (β). This layer has a low refractive index n_2 and the cladding layers above and below it have refractive index n_1 and n_3 ($n_2 < n_1, n_3$). The fundamental mode angle of incidence (θ_1) at the core-cladding boundary is computed by equation (3.1):

$$\theta_1 = cos^{-1}\left(\frac{\lambda}{2 \cdot d_c \cdot n_2}\right) \quad (3.1)$$

Where λ is the wavelength of the propagating light and d_c is the core thickness. This function is found by noting that $cos\theta_1 = \frac{k_T}{k}$ (see Fig. 3.1 (a)) where $k = \frac{2\pi n_2}{\lambda}$ is the wavenumber of the propagating light and the transverse part of the wavenumber must

satisfy the following equation for constructive interference (guiding): $2k_T = \frac{2\pi}{d_c}$. Using Snell's law, the refracted angle in the cladding layer is given by $\theta_2 = sin^{-1}\left(\frac{n_1 sin\theta_1}{n_2}\right)$. As stated above, our interest is in the case where $n_2 < n_1, n_3$. Thus, TIR is not achievable and there will be loss at each boundary between the dielectric materials. The loss in this structure is determined by the absorption coefficient [102]:

$$\alpha = \frac{(1 - R_1 R_3)}{2d_c \tan(\theta_1)\sqrt{R_1 R_3}} \quad (3.2)$$

Where R_1 and R_3 is the reflectance at the top ($n_2 : n_1$) and bottom ($n_2 : n_3$) boundary, respectively. The expressions for reflectance at each boundary are determined by the polarization of the incident light and the relevant refractive indices. The Beer-Lambert law states that the output power (P_{out}) traveling through the core material is given by:

$$P_{out} = P_{in} \cdot e^{-\alpha L} \quad (3.3)$$

Where the input optical power is P_{in} and L is the length over which the light propagates through the core medium.

However, the leaky optical waveguides of interest in this dissertation have rectangular cross sections as depicted in Fig. 3.1 (b). Losses may occur at each of the four boundaries of the low index core (n_2). The losses for a particular polarization will be the sum of both transverse electric (TE) and transverse magnetic (TM) components. For x(y)-polarized light, the TE mode lies in the y(x)-direction and the TM mode in the x(y)-direction. Explicitly, the total losses for x- (α_{x-pol}) and y-

polarized (α_{y-pol}) light in the rectangular structure found in Fig. 3.1. (b) are given by:

$$\alpha_{x-pol} = \frac{\left(1 - R_{TE,1}R_{TE,3}\right)}{2h_c\tan(\theta_y)\sqrt{R_{TE,1}R_{TE,3}}} + \frac{\left(1 - R_{TM,2}R_{TM,4}\right)}{2w_c\tan(\theta_x)\sqrt{R_{TM,2}R_{TM,4}}} \quad (3.4)$$

$$\alpha_{y-pol} = \frac{\left(1 - R_{TE,2}R_{TE,4}\right)}{2w_c\tan(\theta_x)\sqrt{R_{TE,2}R_{TE,4}}} + \frac{\left(1 - R_{TM,1}R_{TM,3}\right)}{2h_c\tan(\theta_y)\sqrt{R_{TM,1}R_{TM,3}}} \quad (3.5)$$

Where $\theta_{x,y}$ is the incident angle in the x- or y-dimension determined by inputting $d_c = w_c, h_c$ into equation (3.1) where w_c and h_c are the low index rectangular core's cross-sectional width and height (see Fig. 3.1 (b)). Reflectance at each of the four boundaries is labelled as TE or TM with a numeric subscript denoting the relevant boundary as labelled in Fig. 3.1 (b). In the following two sections, the reflectance equations will be presented for both capillaries and ARROWs.

3.1 Capillaries

A simple capillary is a structure in which a low index core is surrounded by a higher index of refraction medium (e.g. the structure in Fig. 3.1 (b) in which the entire cladding has index of refraction $n_1 < n_2$). The losses can be calculated using the Fresnel equations which describe both the reflected and transmitted light at a material interface. The reflectance for the TE and TM modes at a given boundary are computed by equations (3.6) [103]:

$$R_{TE} = |r_{TE}|^2 = \left|\frac{n_2 cos\theta_2 - n_1 cos\theta_1}{n_2 cos\theta_2 + n_1 cos\theta_1}\right|^2$$

$$R_{TM} = |r_{TM}|^2 = \left|\frac{n_1 cos\theta_2 - n_2 cos\theta_1}{n_2 cos\theta_1 + n_1 cos\theta_2}\right|^2 \qquad (3.6)$$

For a typical PDMS optofluidic device, the fluidic channel has a cladding layer with $n_1 \approx 1.42$. For a water filled structure (n_2 = 1.33) with $w_c = 12\,\mu m$ and $h_c = 6\,\mu m$, the loss as a function of wavelength (400 to 800 nm) can be found by using equations (3.4), (3.5) and (3.6). The x-polarized and y-polarized losses for the example structure are plotted in Fig. 3.2.

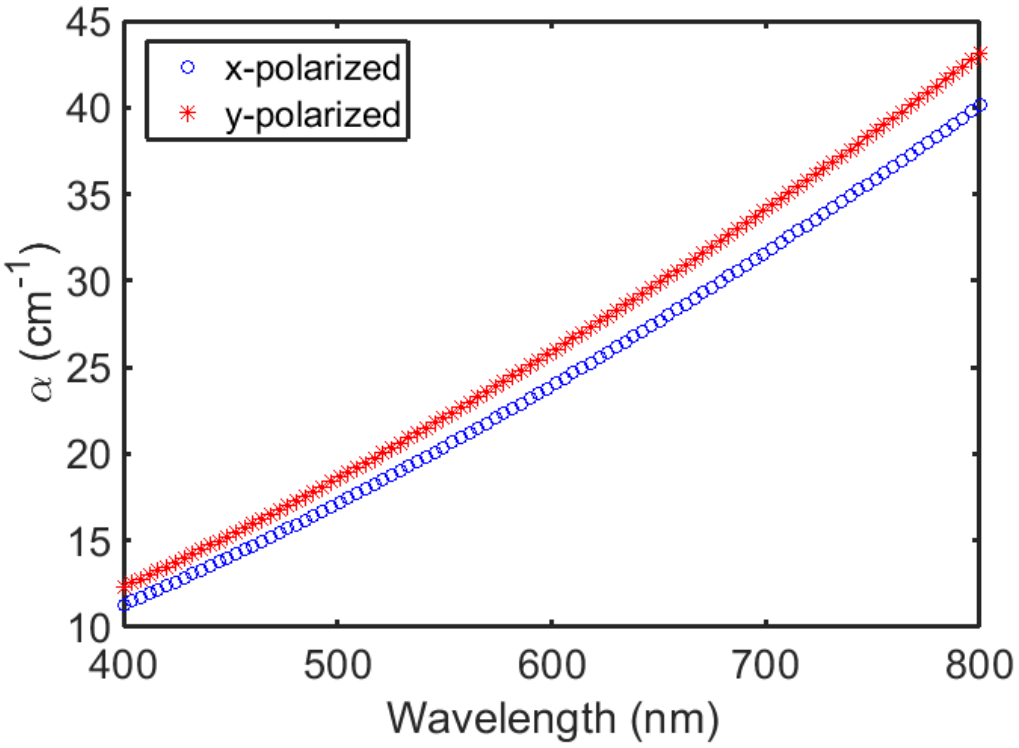

Fig. 3.2 x- and y-polarized loss calculated for a 6 μm x 12 μm water filled capillary (surrounding index of PDMS $n_1 = 1.42$). The wavelength dependent values are calculated as outlined in the text using equations (3.1), (3.4), (3.5) and (3.6). The loss increases with wavelength and the y-polarized loss is larger than the x-polarized light.

A common application for water filled optofluidic chip-scale leaky waveguides is to detect fluorescent particles. Therefore, visible to near-infrared light is commonly used for such applications. Fig. 3.2 shows that common losses in such a water filled waveguide are on the order of tens per centimeter. If the fluidic waveguide is short, then the device may have sufficient sensitivity for the application (as will be demonstrated in Chapter 5). However, vapor filled leaky waveguides are desirable to detect absorption spectra which have refractive index $n \approx 1$. For such applications, long interaction lengths are necessary for low temperature vapors. This means that the light must be guided over a long length of vapor and therefore experiences high loss even without absorption from the vapor (see equation (3.3)). Therefore, vapor-based applications often require lower loss structures than the capillaries presented above in order to see measurable transmission away from the vapor's resonance (path length, L, for such applications must be at least on the order of millimeters for reasonable temperatures). The next section discusses an approach to decrease loss in oxide-based optofluidic platforms utilizing periodic structures.

3.2 Anti-Resonant Reflecting Optical Waveguide

As discussed above, capillary loss increases with wavelength and shrinks with increasing waveguide dimension. Luckily, low index guiding is achievable with interferometric confinement by structuring the high cladding index. Examples include Bragg fibers [104], photonic bandgap fibers [105] and photonic crystal slab waveguides [106]. Anti-resonant reflecting optical waveguides (ARROWs) were first

proposed by Duguay [107] and use an anti-resonance condition in order to guide leaky modes since these structures result in radiation losses as the mode propagates (finite reflectivity at each boundary). The following distinction will be made between the two types of ARROWs as follows: hollow core (HC-ARROW) and solid core (SC-ARROW). However, the anti-resonant condition is central to both.

Consider the HC-ARROW structure found in Fig. 3.3. A low index core (n_c) with thickness d_c is surrounded by two layers of dielectric with indices n_i and thicknesses d_i where i indicates the i^{th} layer from the core outward. As above, the mode wavevector, k is comprised of a transverse component (k_T) and a parallel component along z (β). The ARROW layers surrounding the core are each designed to act as mirrors for the wavelength of interest.

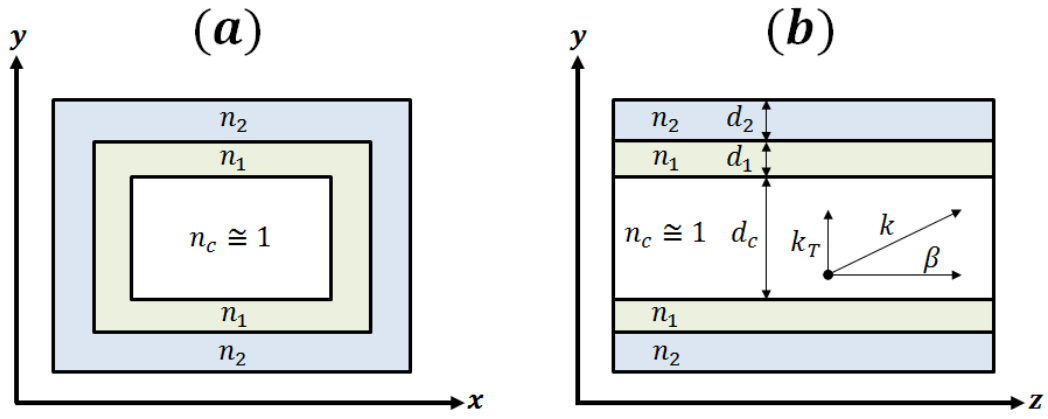

Fig. 3.3 HC-ARROW cross sections (a) in the y-x plane and (b) in the y-z plane.

As with capillaries, the transmitted modes have both TE and TM modes for x- and y-polarization. Therefore, equation (3.4) and (3.5) must be used to determine the structure's loss. However, the simple Fresnel equations are not enough to compute the

reflectance at the four boundaries surrounding the low index core as more than one dielectric layer exists. The anti-resonant condition that must be satisfied to reflect light from the i^{th} layer states that the entire transverse round trip phase shift is equal to an odd integer multiple of π. Explicitly, the condition in the i^{th} layer is the following:

$$(2n-1)\pi = 2d_i k_T + \varphi_i \qquad (3.7)$$

Where $n = 1, 2, 3$ ... and φ_i is the total phase shift picked up at the layer boundaries. The total phase shift (φ_i) must be carefully considered for varied index sequences and polarizations.

For example, consider light propagating in a material with index n_i which is incident on the boundary of a material with index of refraction equal to n_t. TM light that is reflected will acquire a π (0) phase shift if the incident angle is less (greater) than the Brewster angle:

$$\theta_B = \text{atan}\left(\frac{n_t}{n_i}\right) \qquad (3.8)$$

However, reflected TE light will acquire a π phase shift only if $n_t > n_i$ and a 0 phase shift if $n_t < n_i$. The total phase shift, φ_i in the i^{th} layer is then the sum of the phase shifts at each of the boundaries. For HC-ARROWs the total phase shift in the core is always $\varphi_i = 2\pi$ as the core is a lower index material that the first cladding layer. For $n_{i+1} > n_i > n_{i-1}$ the total TE phase shift is $\varphi_i = \pi$ and for $n_i > n_{i-1}, n_{i+1}$ $\varphi_i = 0$. Therefore, we use the latter index sequence for the first ARROW layer (from the core outward) in order to keep the same TE anti-resonance condition for all layers

as $\varphi_i = 0$ or $\varphi_i = 2\pi$ results in the condition that $2d_i k_T$ is equal to an odd integer multiple of π.

As mentioned above, an analysis of the incident angle and index series must be considered to determine the total phase shift acquired for TM light. For example, consider $780\,nm$ wavelength light guiding in a $6\,\mu m$ tall HC-ARROW that is incident on a Si_3N_4 layer ($n_1 = 2.1$). The resulting incident angle computed using equation (3.1) in the core is found to be $\theta_c = 86.27°, 87.20°$ if the core is filled with air or water, respectively ($n_c = 1.00, 1.33$). Light refracted into this Si_3N_4 layer will have a refracted angle of $\theta_1 = 28.37°, 39.24°$ if the core is filled with air ($n_c = 1$), water ($n_c = 1.33$). Now consider a second ARROW layer fabricated with SiO_2 ($n_2 = 1.46$). The Brewster angle is calculated to be $\theta_{B,SiO_2} = 34.81°$. Therefore, a TM mode will acquire a π phase shift for the air filled core and a 0 phase shift for the water filled core. Any light reflected from this boundary will then be incident upon the core layer again which has $\theta_{B,core} = 25.46, 32.35°$ for air, water. At this boundary, neither TM mode will acquire a phase shift and the resulting total phase for the air (water) filled core is $\varphi_{i=1} = \pi$ ($\varphi_{i=1} = 0$). Therefore, the anti-resonance condition is different for the same ARROW structure depending on the core material. The thickness of the i^{th} ARROW layer can be determined by considering these phase shifts [107]:

$$t_i = \frac{N\lambda}{4\sqrt{1 - \left(\frac{n_c}{n_i}\right)^2 + \left(\frac{\lambda}{2t_c n_i}\right)^2}}; N = \begin{cases} 1, 3, 5;\ \varphi_i = 2\pi, 0 \\ 2, 4, 6;\ \varphi_i = \pi \end{cases} \qquad (3.9)$$

SC-ARROWs also use the anti-resonant condition but only on the bottom side of the waveguide (the facet facing silicon) as seen in Fig. 3.4. The core is typically fabricated with SiO_2 ($n_c \approx 1.46$) and thereby guides via TIR on the sides in which it is exposed to air. The resulting reflectance on boundaries 1, 2 and 4 (see. Fig. 3.1 (b)) will be ideally be equal to 1 (100% reflectance). This allows a system of solid and hollow planar waveguides to be fabricated together on a wafer as described in section 3.3.

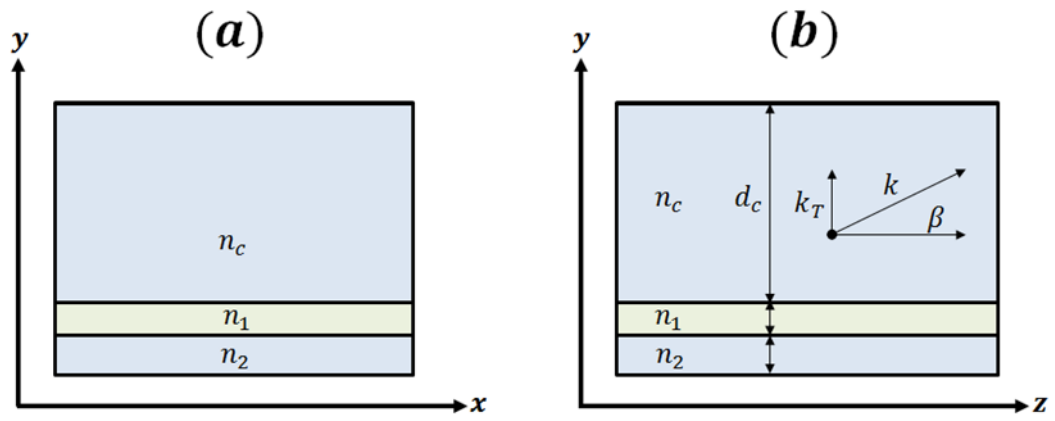

Fig. 3.4 SC-ARROW cross sections (a) in the y-x plane and (b) in the y-z plane. Light is guided in the core via the anti-resonance condition in the –y direction and via total internal reflection otherwise.

The theoretical losses for an ARROW can be calculated using the transfer matrix formalism [108]. Consider the structure in Fig. 3.5 in which light propagates along in the x-direction. The light passes through a sequence of dielectric materials, n_1, n_2 and n_3. The propagating electric field can be written as

$$E(x) = Re^{-ikx} + Le^{+ikx} \equiv A(x) + B(x) \quad (3.10)$$

Where k is the wave vector in the x-direction, Re^{-ikx} is the wave traveling in the right direction (+x-direction) and Le^{+ikx} travels towards the left (-x-direction). The right and left traveling coefficients in Fig. 3.5 are defined as:

$$\begin{aligned} A_1 &= A(0^-) \\ B_1 &= B(0^-) \\ A'_2 &= A(0^+) \\ B'_2 &= B(0^+) \\ A_2 &= A({x_1}^-) \\ B_2 &= B({x_1}^-) \\ A'_3 &= A({x_1}^+) \\ B'_3 &= B({x_1}^+) \end{aligned} \tag{3.11}$$

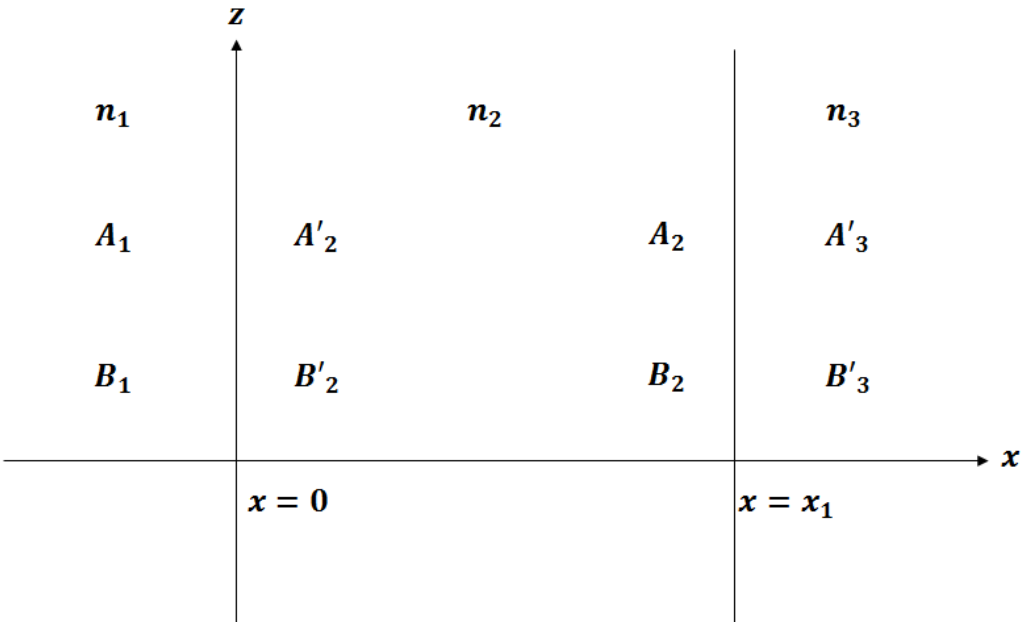

Fig. 3.5 Schematic of a thin dielectric medium in which light propagates.

The field amplitude vectors propagating in the x-direction can be expressed:

$$\begin{pmatrix} A_1 \\ B_1 \end{pmatrix} = D_1^{-1} D_2 \begin{pmatrix} A'_2 \\ B'_2 \end{pmatrix} \equiv D_{12} \begin{pmatrix} A'_2 \\ B'_2 \end{pmatrix}$$

$$\begin{pmatrix} A'_2 \\ B'_2 \end{pmatrix} = P_2 \begin{pmatrix} A_2 \\ B_2 \end{pmatrix} = \begin{pmatrix} e^{ik_2 x_1} & 0 \\ 0 & e^{-ik_2 x_1} \end{pmatrix} \begin{pmatrix} A'_2 \\ B'_2 \end{pmatrix} \quad (3.12)$$

$$\begin{pmatrix} A_2 \\ B_2 \end{pmatrix} = D_2^{-1} D_3 \begin{pmatrix} A'_3 \\ B'_3 \end{pmatrix} \equiv D_{23} \begin{pmatrix} A'_3 \\ B'_3 \end{pmatrix}$$

Where D_i is called a dynamical matrix and is found by considering the continuity of the electric and magnetic fields at each boundary [108]:

$$D_i = \begin{cases} \begin{pmatrix} 1 & 1 \\ n_i cos\theta_i & -n_i cos\theta_i \end{pmatrix}; TE \\ \begin{pmatrix} cos\theta_i & cos\theta_i \\ n_i & -n_i \end{pmatrix}; TM \end{cases} \quad (3.13)$$

Where P_2 considers the appropriate phase shift ($\varphi = k_2 x_1$) picked up in medium 2 where $k_i = \frac{n_i \omega cos\theta_i}{c}$. Using the above dynamical matrices, the transmission matrices, D_{ij} can be defined:

$$D_{ij} = \begin{cases} \frac{1}{2}\begin{pmatrix} 1+\frac{k_2}{k_1} & 1-\frac{k_2}{k_1} \\ 1-\frac{k_2}{k_1} & 1+\frac{k_2}{k_1} \end{pmatrix}; TE \\ \frac{1}{2}\begin{pmatrix} 1+\frac{n_2^2 k_1}{n_1^2 k_2} & 1-\frac{n_2^2 k_1}{n_1^2 k_2} \\ 1-\frac{n_2^2 k_1}{n_1^2 k_2} & 1+\frac{n_2^2 k_1}{n_1^2 k_2} \end{pmatrix}; TM \end{cases} \quad (3.14)$$

The input and output field amplitudes can be related by:

$$\begin{pmatrix} A_1 \\ B_1 \end{pmatrix} = D_1^{-1} D_2 P_2 D_2^{-1} D_3 \begin{pmatrix} A'_3 \\ B'_3 \end{pmatrix} \quad (3.15)$$

This transfer matrix formalism can be applied to a stack of N dielectric layers as seen in Fig. 3.6:

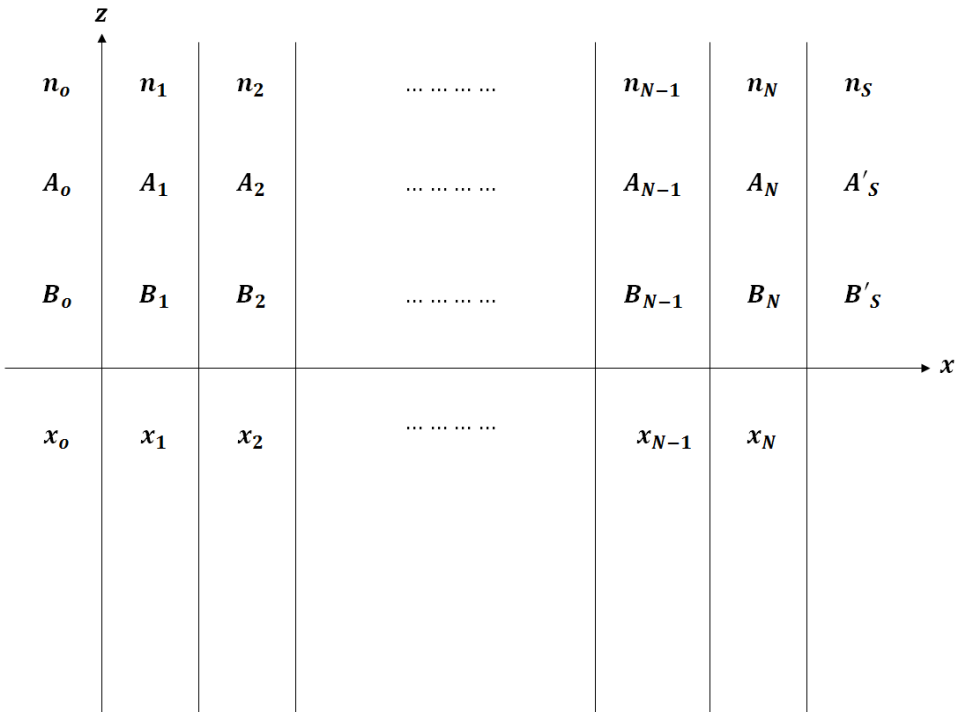

Fig. 3.6 A stack of $\boldsymbol{N}$ dielectric layers.

For the multilayer dielectric system in Fig. 3.6, the relationship between the input and output field amplitudes is given by:

$$\begin{pmatrix} A_o \\ B_o \end{pmatrix} = \begin{pmatrix} M_{11} & M_{12} \\ M_{21} & M_{22} \end{pmatrix} \begin{pmatrix} A'_S \\ B'_S \end{pmatrix} \quad (3.16)$$

Where $$\begin{pmatrix} M_{11} & M_{12} \\ M_{21} & M_{22} \end{pmatrix} = D_o^{-1} \left(\prod_{i=1}^{N} D_i P_i D_i^{-1}\right) D_S \quad (3.17)$$

Therefore, the dynamical matrices must be calculated for each medium and from these values, the reflectance can be determined by:

$$R = \left|\frac{M_{21}}{M_{11}}\right|^2 \quad (3.18)$$

Finally, this expression for reflectance can be used with equations (3.2), (3.4) and (3.5) to determine the loss in ARROW structures. A minimum loss value has been derived for both TE and TM modes if $n_c < n_2 < n_1$:

$$\alpha_{Min\_TE} = \left(\frac{{n_2}^2 - {n_c}^2}{{n_1}^2 - {n_c}^2}\right)^{N/2} \alpha_o \quad (3.19)$$

$$\alpha_{Min\_TM} = \left(\frac{{n_1}^{N+1}}{n_2 {n_c}^N}\right)^2 \alpha_{Min_{TE}} \quad (3.20)$$

$$\alpha_o = \frac{\lambda^2 m^2}{n_c {d_c}^3 \sqrt{{n_1}^2 - {n_c}^2}} \quad (3.21)$$

Where N is the number of anti-resonant layers and $m = 1,2,3$ ... is the mode order. Though these are minimum loss values, several important characteristics can be determined. First note that minimal TM loss is greater than TE loss by a factor $\left(\frac{{n_1}^{N+1}}{n_2 {n_c}^N}\right)^2$. Also, loss is decreased with the addition of ARROW layers and loss is inversely proportional to the core index and has a ${d_c}^{-3}$ dependence. Note that in reality there are of course fabrication imperfections (e.g. surface roughness which leads to scatter).

For our typically fabricated HC-ARROW structures [109], $N = 6$ and $\lambda = 794.98\ nm$ (corresponding to the D_1 hyperfine transitions in Rb). For the rubidium filled HC-ARROW structures discussed in chapter 4, the layers are engineered to have the x- and y-polarized loss profiles near their D2 and D1 hyperfine transitions (780.24 nm and 794.98 nm, respectively) as seen in Fig. 3.7 (see appendix B for a discussion on the designed ARROW layers). The x-polarized losses are smaller than

those found in the case of capillaries (see Fig. 3.2, $\alpha \approx 40\ cm^{-1}$) and the HC-ARROW y-polarized losses are much larger than the x-polarized losses. This conclusion is consistent with equations (3.4), (3.5) and (3.21).

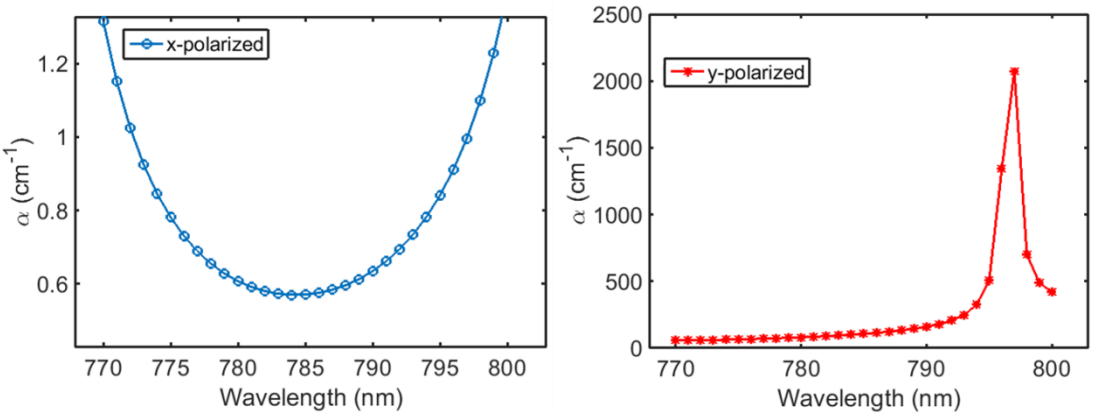

Fig. 3.7 x- (left) and y-polarized (right) for a 6 $\mu m\ x\ 12\ \mu m$ cross-sectional dimension HC-ARROW structure designed for guiding light through rubidium vapor (see appendix B for more on the layer designs). The y-polarized losses are much larger than the x-polarized losses as expected.

3.3 Fabrication of Optofluidic Devices

The leaky optical waveguides described above are used in the devices presented within this text to facilitate light-matter interactions with fluids (vapors and liquids). Two platforms will be discussed: oxide- and polydimethylsiloxane (PDMS). These two platforms are similar in that they both combine a system of hollow rectangular channels (which double as leaky optical waveguides as described above) with solid-core rectangular optical waveguides. This system of waveguides comprises the "chip."

For vapor experiments, the devices are fabricated from a system of oxides which produce ARROWs presented above. Also discussed within this thesis is an all-polymer analogue of the oxide-based system which is fabricated using PDMS (which uses capillary leaky optical waveguides). Sections 3.3.1 and 3.3.2 describe the fabrication procedures for the creation of the oxide- and PDMS-based optofluidic devices, respectively.

3.3.1 Oxide-based Devices

The fabrication of oxide-based optofluidic devices allows the integration of vapors on-chip. PDMS devices are permeable to vapors and thereby are not an ideal candidate for such applications. Though growing oxides on silicon is a more challenging procedure than creating PDMS structures, the benefit is that the optical losses within the fluidic channel can be decreased using anti-resonant reflecting optical waveguides (ARROW) [107]. The fabrication of the devices described here was carried out by our collaborators at Brigham Young University in the lab of Dr. Aaron Hawkins.

The flowchart in Fig. 3.7 describes the fabrication of the oxide-based devices. Both solid and hollow- waveguides are fabricated in tandem on a single silicon wafer, resulting in a fully integrated device for enabling light-matter interactions with fluids (note that others also have used these devices for the detection of particles suspended within liquids [110], [111], [112]). The process begins with a silicon wafer in which ARROW layers are deposited (via plasma enhanced chemical vapor deposition

(PECVD) – note that such wafers can also be commercially purchased with pre-grown layers). The next step involves spinning on an SU-8 photoresist and UV-patterning a sacrificial core for the hollow-core ARROW. After patterning the sacrificial SU-8, a protective nickel (Ni) layer is deposited near the areas in which the solid- and hollow- core waveguides will be defined. Next, a reactive ion etch (RIE) removes some of the ARROW layers and etches into the silicon where the waveguides will not be patterned. The Ni is then removed and the top layers can be deposited via PECVD. Fig 3.8 shows the deposition of only a thick top silicon dioxide layer; however top ARROW layers may also be deposited before the thick top oxide if lower loss is desired. Following the top layer deposition, the solid-core ridge waveguide is defined. To do so, a thick SU-8 layer is patterned where the structure is to be undisturbed. Then RIE is used to etch into the top oxide some distance to create a ridge in the top layer for solid-core waveguide definition. Lastly, all SU-8 is removed (including the sacrificial core) and the device can be filled with fluid. The design for a typical alkali-filled oxide-based device has a footprint small enough that ~ 32 chips are fabricated on a single 6 inch diameter silicon wafer. The individual devices can then be cleaved using a diamond scribe.

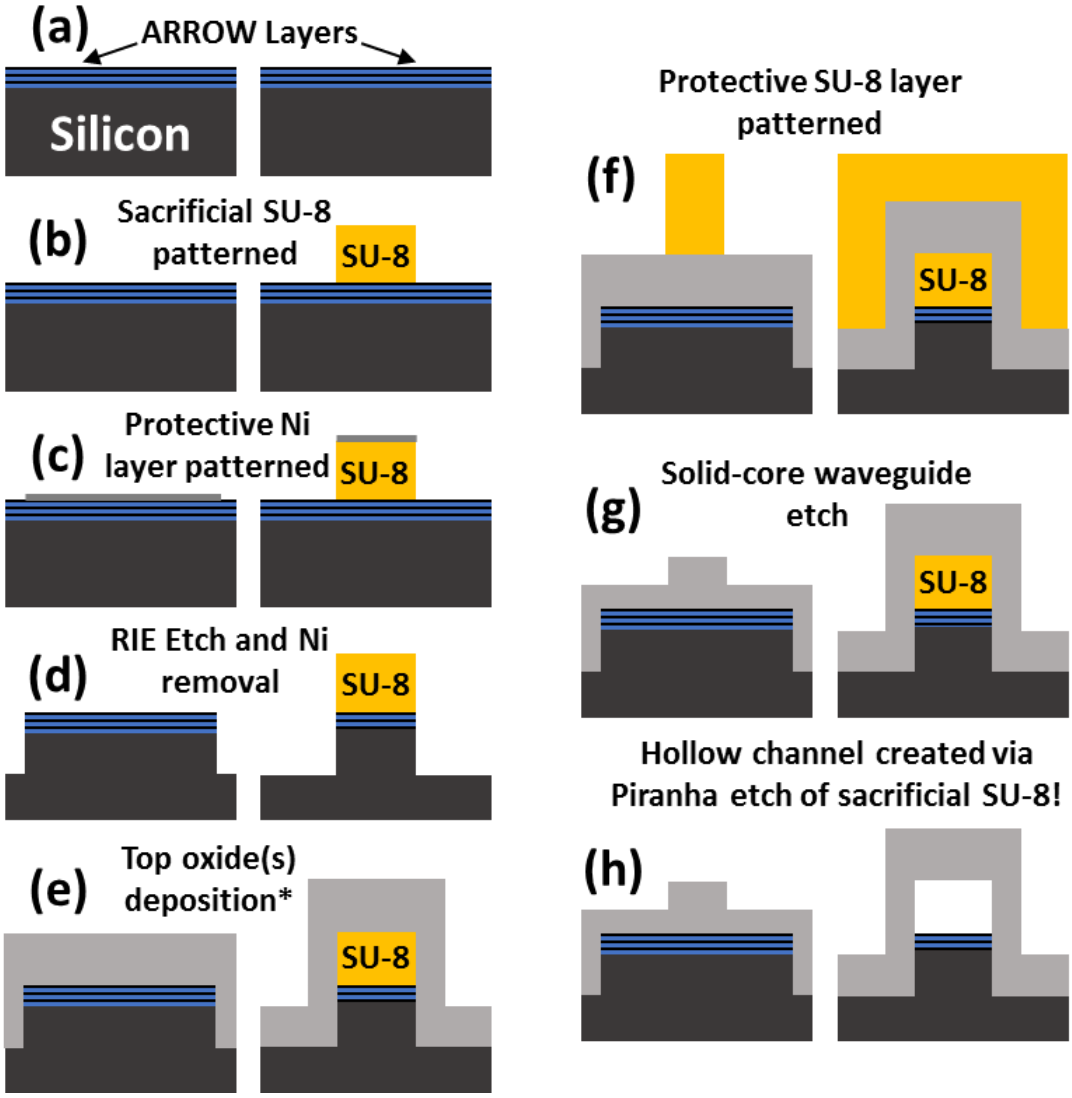

Fig. 3.8 Oxide-based ARROW chip fabrication flowchart. (a) Bottom ARROW layers are grown (PECVD) onto a silicon wafer. (b) A sacrificial SU-8 core is patterned for the creation of the hollow-core. (c) A protective Ni layer is deposited to protect the waveguide areas from (d) an RIE etch. The Ni is removed and (e) the top layers (ARROW and/or top silicon dioxide) are deposited via PECVD. (f) A thick protective SU-8 is patterned to protect the layers from the (g) solid-core waveguide RIE. (h) All SU-8 is removed and the devices are ready for cleaving and filling.

3.3.2 Polydimethylsiloxane Devices

A relatively less expensive and faster fabrication method uses soft photolithography. The elastomer PDMS has been used rampantly within microfluidics [113] and its viscoelasticity makes it ideal for the integration of pneumatic chambers and valves [114] into such microfluidic devices. Recently, waveguides were also integrated into pneumatic valves on an optofluidic chip ("lightvalve") [115]. Chapter 5 will describe three optofluidic devices fabricated with PDMS as described here.

The PDMS device fabrication flowchart is found in Fig. 3.9. As with the oxide-based devices, the fabrication of PDMS devices starts with a silicon wafer. A layer of SU-8 is spun directly onto the silicon and is patterned with UV light. This SU-8 "master" will act as a mold for a given PDMS structure and can be used multiple times as a cast for a given design. After the SU-8 master is fabricated, it and a blank silicon wafer are silanized to lay down an atomically thin layer to prevent adhesion of the cured PDMS to the master. This will allow for the easy removal of the cured PDMS from the master and prevent damage to either. PDMS (Sylgard 184) is received as two bottles, a base and curing agent. Typically, the base to curing agent ratio is mixed as 10 to 1 by weight ("10:1") in a cup, stirred vigorously and then allowed to degas (as bubbles form within the mixture during mixing) in a desiccator for ~ 1 hour or until all bubbles are evacuated from the viscous mixture. However, the index of refraction can be altered by changing this base to curing agent ratio [116]. A 5:1 ratio results in a higher index of refraction and is used to fabricate the core for on-

chip solid-core waveguides (note that for the PDMS structure, the solid-core waveguides work using TIR) as well as fluidic sidewalls. After silanization, 5:1 PDMS is spun onto the patterned master for 30 minutes at 6000 RPM. This layer is then allowed to cure for two hours in an oven at 60℃. After curing, 10:1 PDMS is poured directly on top of the cured 5:1 layer. Concurrently, 10:1 is poured onto the blank silanzied silicon wafer. These layers are cured overnight in the same 60℃ oven. After all the PDMS is cured, the layers are both peeled from their silicon wafers and holes are punched into the patterned wafer to provide fluidic access to the final device. The two layers are O_2 plasma bonded together to create the final wafer. Individual devices are cleaved using a razor blade.

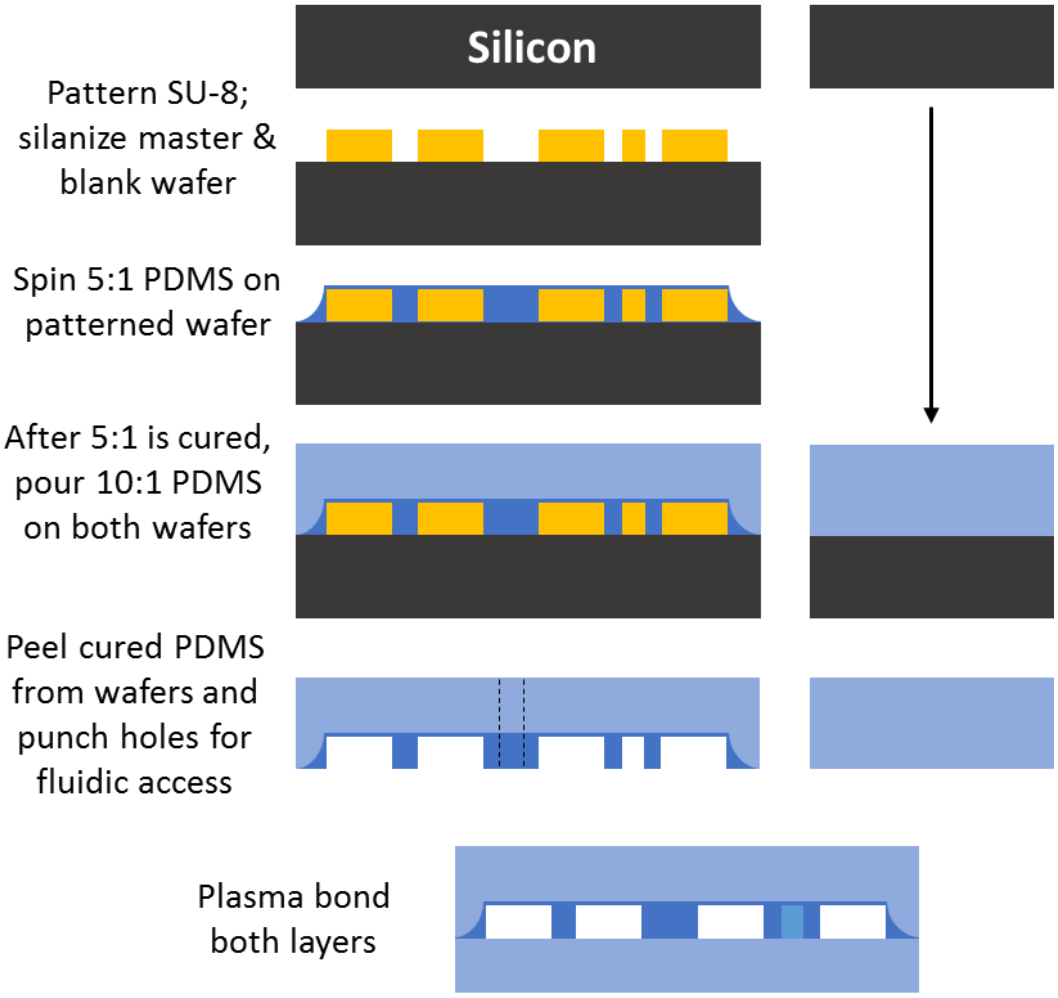

Fig. 3.9 PDMS-based optofluidic device fabrication flowchart. A silicon wafer is patterned with SU-8 to act as a mold for the 5:1 PDMS layer. Both the SU-8 master and a blank silicon wafer are silanized. 5:1 to PDMS is spun at 6000 RPM for 30 minutes onto the silanized patterned master to create the solid-core optical waveguides and the fluidic sidewalls. The 5:1 is cured for 2 hours at 60℃ and then 10:1 is poured directly on top of the 5:1. Additionally, 10:1 is poured onto the silanzized blank silicon wafer. All PDMS is cured overnight at 60℃. Fluidic access holes are punched into the patterned PDMS wafer and the two layers are bonded via O_2 plasma.

Chapter 4

On-Chip Atom Optics

Ol'Shanii et al. [117] and Renn et al. were the first to optically guide Rb atoms through hollow-core fiber [118] and demonstrate that the gradient force produced in the waveguide was sufficient for transverse confinement of the atoms, producing a potential well of 71mK depth in different size (inner diameter (ID) 40 and 10 μm) fibers (where the potential well depth energy, ΔE, is related to temperature, T, by the Boltzmann constant, k_B: $\Delta E = T \cdot k_B$). Since then, several examples of optical guiding and trapping in hollow-core photonic crystal fiber (HC-PCF) have been demonstrated [119], [120], [121], [122], [11]. Linear and nonlinear spectroscopy as well as electromagnetically induced transparency (EIT) has also been demonstrated in HC-PCF with Rb [31], [123], [124] and acetylene [32], [125]. More recently, chip-based approaches to waveguide-based atomic spectroscopy have emerged including self-contained silicon chips based on anti-resonant reflecting optical waveguides which demonstrated atomic spectroscopy, EIT, and slow light in Rb-filled waveguides [109][29]. More recently, Stern et al. introduced a chip platform based on evanescent fields from solid-core waveguides interacting with near-surface atoms [28]. These so called atomic cladding waveguides have been used to demonstrate non-linear effects [126] and all-optical switching [127]. More recently,

on-chip absorption spectroscopy has also been demonstrated with slot waveguides [128].

Here, alkali filled ARROW devices are discussed. This chapter summarizes an all-optical approach to cooling atomic vapor using a spatially varied AC Stark shift. Two ARROW-based chip-scale designs are presented which could be used to cool Na atoms to final speeds comparable to Zeeman slowers. Slowing is built into the devices themselves and requires no additional external control (e.g. frequency chirping or magnetic fields). Additionally, a device layout is presented which incorporates multiple Rb cells which can be used to demonstrate photonic devices using EIT based slow and stored light. Lastly, a discussion on experimental difficulties is presented in loading such devices with atomic vapors.

4.1 All-Optical Cooling

Chapter 2 presented a discussion on the relationship between an atom's speed and its temperature. Through conservation of momentum over many scattering cycles, atoms can be slowed (cooled). To continually absorb photons as the atom cools, the cooling laser must always appear on resonance. Chapter 2 also presented some common cooling methods including Zeeman cooling and chirped cooling which can result in final speeds on the order of tens of meters per second. Chapter 3 presented oxide-based ARROWs which allow light to guide in low index medium (e.g. alkali vapors). The amount of loss in the waveguide structure is heavily dependent on the waveguide parameters (e.g. width, ARROW layers, etc). The loss will determine the

optical power (equation (2.28)) along the direction of light propagation and the size of the hollow core area will determine the mode area. Here, a novel all-optical analogue to Zeeman cooling is presented. This approach uses two lasers as seen in Fig. 4.1 (a): one counter-propagating Doppler cooling beam and another co-propagating laser which provides an appropriate AC Stark light shift which is proportional to the intensity of the optical field which takes the role of the magnetic field in the Zeeman slower. As an example, two ARROW structures are presented which provide an intensity profile which is appropriately tailored to cool Na atoms to final speeds of 40 m/s with two fixed frequency input laser beams.

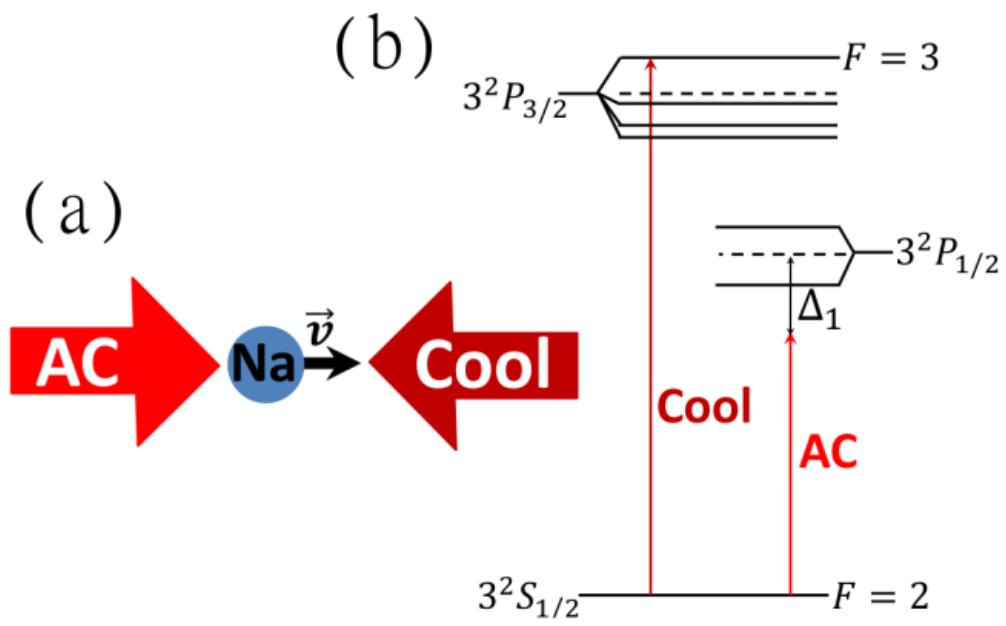

Fig. 4.1 (a) Example beam geometry. Doppler "cool" beam counter-propagates while an "AC" Stark beam co-propagates with the atom. (b) The relevant hyperfine transitions for Na cooling.

An expression for the AC Stark light shift can be found using second-order perturbation theory. Consider a two-level atom with a ground state, $|g>$ and an excited state, $|e>$. In the Dipole approximation, the interaction Hamiltonian is given by $H = -\hat{\mu} \cdot \vec{E}$ where $\vec{E}$ is the electric field vector and the Dipole moment is $\hat{\mu} = e\vec{r}$ where e is the electron charge. The resulting energy shift is given by:

$$\Delta E = \mp \frac{|< e|\mu|g >|^2}{\Delta} \left|\vec{E}\right|^2 \equiv \mp \frac{{\mu_{eg}}^2}{\Delta} \left|\vec{E}\right|^2 \quad (4.1)$$

Where $\Delta = \delta_L - \vec{k} \cdot \vec{v}$ and $\delta_L = \omega - \omega_o$ is the detuning of the laser in the lab frame with $\hbar\omega_o = E_i$ and ω being the angular frequency of the incoming laser. For near resonant beams, the $\mp$ signs correspond to the excited (-) and ground state (+) shifts respectively. Thus, if the light is red shifted ($\Delta < 0$) then the excited and ground states get pushed further apart as seen in Fig. 4.2 (a). A blue shifted laser ($\Delta > 0$) in the lab frame results in the opposite effect as seen in Fig. 4.2 (b). The optical intensity (I) is related to the electric field by: $I = 2\varepsilon_o c\left|\vec{E}\right|^2$. Using this relationship, equation (4.1) can be re-written in terms of intensity:

$$\Delta E = \mp \frac{{\mu_{eg}}^2 I}{2\varepsilon_o c \Delta} \quad (4.2)$$

Therefore, the AC Stark light shift is directly proportional to the field intensity, I and inversely proportional to the detuning from resonance, Δ.

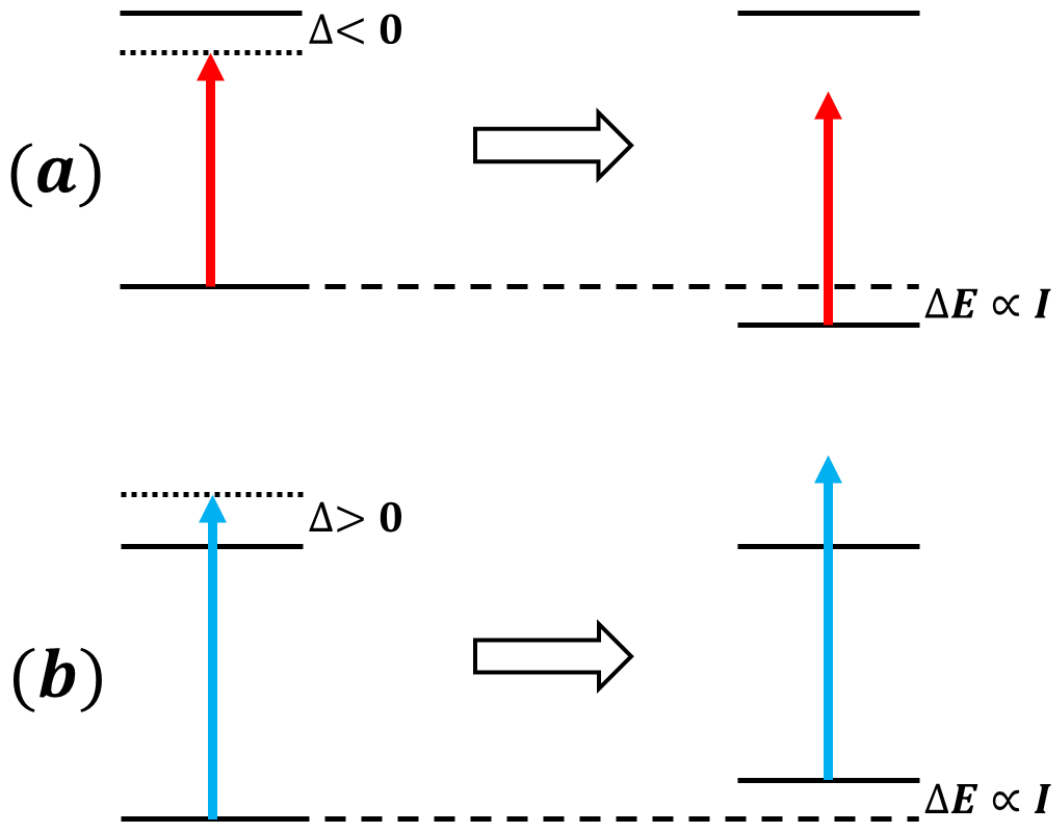

Fig. 4.2 (a) A red shifted beam ($\Delta < 0$) in the lab frame results in an AC Stark shift (ΔE) which pushes the energy levels away from one another and is proportional to the laser's intensity. (b) A blue shifted laser ($\Delta > 0$) in the lab frame results in an AC Stark shift (ΔE) which pushes the energy levels toward one another and is proportional to the laser's intensity.

Equation (4.2) assumes there are only two energy levels present ($|g>$ and $|e>$). However, atomic energy systems are realistically more complicated than this simple two level model. In the ARROW examples presented below, the hyperfine energy levels of ^{23}Na are used to cool the atoms. Recalling Fig. 2.1, there are clearly more than two energy levels present that are closely spaced and therefore must be considered. Therefore, equation (4.2) is not adequate to describe cooling of a realistic

system. Instead, the light shifts over the different unperturbed energy level must be summed up for each transition:

$$\Delta E = \mp \frac{I}{2\varepsilon_o c} \sum_j \frac{{\mu_{ij}}^2}{\Delta_{ij}} \quad (4.3)$$

To simplify the summation, the transition strength coefficients for the different energy levels (c_{ij}) can be used. The square of these values denotes the line strengths of each transition and are published. Using these strength transitions, the dipole moment can be re-written as $\mu_{ij} = c_{ij}\mu_i$ (via the Wigner-Eckart Theorem [129]) where μ_i is determined by the excited hyperfine transitions ($i = 1,2$ corresponding to $D_{1,2}$). If the detuning of the transition is greater than the hyperfine splittings then the ground state energy shift can be approximated by:

$$\Delta E = \frac{I{\mu_i}^2}{2\varepsilon_o c \Delta_{F,i}} \sum {c_{ij}}^2 \quad (4.4)$$

Where the subscript F designates the ground state, $i = 1,2$ again designates the excited state hyperfine level corresponding to the D_i transition and $\Delta_{F,i}$ is the detuning from the center of the hyperfine transition to the F^{th} ground state. Therefore, the summation need only be performed over the transition strengths for a particular excited state. When the detuning of a linearly polarized (π-polarized) laser is largely detuned ($\Delta_{F,i} \gg \Gamma_i$) then $\sum {c_{ij}}^2 \rightarrow \frac{1}{3}$. Thus, the light shift for π-polarized far detuned light can be written as:

$$\Delta E = \frac{I{\mu_i}^2}{6\varepsilon_o c \Delta_{F,i}} \quad (4.5)$$

Using the relationship between dipole moment and the decay rate:

$$\Gamma_i = \frac{{\omega_o}^3}{3\pi\hbar\varepsilon_o c^3}\,{\mu_i}^2 \quad (4.6)$$

Where ω_o is the angular frequency for the transition, the light shift can be re-written as:

$$\Delta E = \frac{\pi\hbar c^2 \Gamma_i I}{2{\omega_o}^3 \Delta_{F,i}} \quad (4.7)$$

This expression for the AC Stark shift can be used analogously to the Zeeman shift presented in Chapter 2 (equation (2.8)). Using equation (4.7) as the AC Stark shift as a function of light propagation along the z-direction ($\Delta E_{\mathrm{AC}}(z)$) and the Doppler light shift from equation (2.5), the following condition must be met (compare with equation (2.6)) to allow for sustained cooling of the atoms along the z-direction:

$$\Delta E_{\mathrm{AC}}(z) + \Delta E_{\mathrm{D}}(z) = 0 \quad (4.8)$$

To do so, two beams are used (see Fig. 4.1): a counter-propagating, on resonance fixed frequency Doppler cooling beam and a co-propagating AC Stark beam to dynamically move the ground state and allow for continual cooling. The relevant hyperfine transitions for ^{23}Na are shown in Fig. 4.1 (b) and the detuning of the AC Stark beam from the center of the D_1 hyperfine transitions is denoted as Δ_1. Note that in practice, the use of a re-pump beam would be necessary to prevent population depletion for the ground state via optical pumping [42] (see appendix C for more on optical pumping).

The AC Stark cooling beam is detuned by Δ_1 from the D_1 hyperfine transition and the cooling beam is locked to resonance between the $3^2S_{1/2}, F = 2 \rightarrow$

$3^2P_{3/2}, F' = 3$ D_2 hyperfine transitions. The waveguide must therefore guide light at both D_1 and D_2 wavelengths (589.19 and 589.76 nm). The ARROW layers were designed using two oxides: SiO_2 which has a refractive index of 1.46 and Ta_2O_5 with a refractive index of 2.107. The proposed waveguide consists of twelve ARROW layers as seen in Fig. 4.3 and whose thicknesses were determined from the anti-resonance condition as described in section 3.2 (equation (3.6)). The hollow core is 10 μm tall (y-direction) and has a variable width (w). From the core outward, the ARROW layers consist of alternating Ta_2O_5 (thickness 79nm) and SiO_2 (thickness 138nm) dielectrics with the exception of the final top oxide whose thickness varies in the designs below.

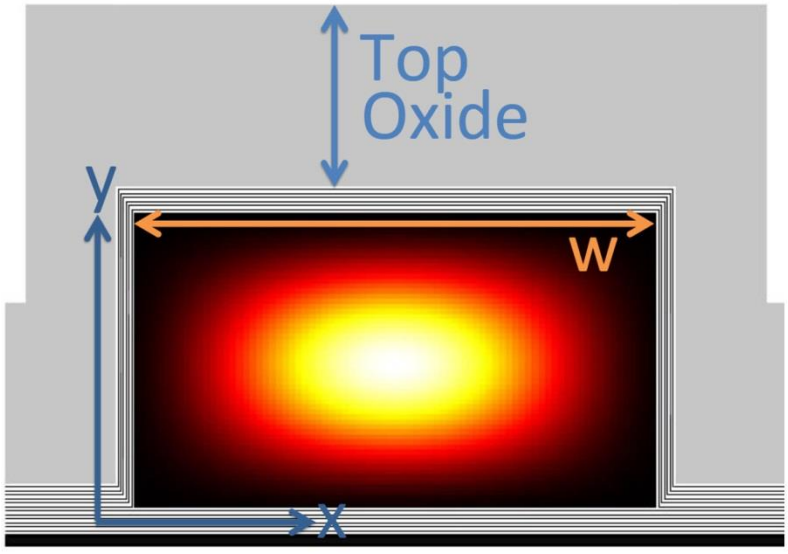

Fig. 4.3 Cross section of twelve layer HC-ARROW design. The top oxide thickness and the hollow core width, w, are the parameters to be varied in the following waveguide designs.

For continual cooling, equation (4.8) must be satisfied along the z-direction where $\Delta E_{AC}(z)$ is given by equation (4.7). Expressing power in a lossy waveguide

along the z-direction via the Beer-Lambert law (equation (2.28)), the intensity along z can be written:

$$\mathrm{I}(z) = \frac{\mathrm{P_{in}} e^{-\alpha(\mathrm{z})\mathrm{z}}}{\mathrm{A(z)}} \quad (4.9)$$

Thus, the intensity can be varied by altering the loss, $\alpha(\mathrm{z})$, or the fundamental mode area, $\mathrm{A(z)}$, along the z-direction. Combining equation (4.9) and equation (4.7), an expression for the AC Stark shift as a function of waveguide loss and mode area can be determined:

$$\Delta E_{AC}(z) = \frac{\pi c^2 \Gamma}{2\omega_o^3}\left(\frac{1}{\Delta_{1,\mathrm{F}}}\right)\frac{\mathrm{P_{in}} e^{-\alpha(\mathrm{z})\mathrm{z}}}{\mathrm{A(z)}} \quad (4.10)$$

Below, two waveguide designs are presented which use equation (4.10) and (4.8) to provide cooling of ^{23}Na atoms to final speeds of 40 m/s. In current chip designs [109],[29], atoms are introduced into the waveguides by heating metal reservoirs of ~ 2 mm ID. The waveguide itself with its ~12 μm x 5 μm cross section acts as the aperture producing a directed beam of ~3mrad divergence, comparable to or better than previously reported examples [39], [40]. By integrating the Maxwell thermal velocity distribution for an initial temperature of 130℃ up to the transverse capture velocity for these waveguides, guided atom fluxes are found to be on the order of ~ 10^4 Hz [118]. Note that the following examples use ^{23}Na and ARROW based optical waveguides for cooling, but in principle, this all-optical cooling approach is amendable to other atomic species and methods for intensity tuning.

The first example waveguide is designed by changing the width of the waveguide along the direction of deceleration, z. Changing the width (w) will affect

both the waveguide loss and the fundamental mode area. Therefore, for each step along the z-direction, both $\alpha(w)$ and $A(w)$ must be determined. In order to extract these parameters, a waveguide with a 10 μm core height and varying width (between 3 and 60 μm) was simulated. The loss for each width was determined via Matlab script which uses the previously described transfer matrix formalism (see section 2.2) and the fundamental mode area was determined using FIMMWAVE software by Photon Design. Fig. 4.4 plots the mode loss and area as a function of increasing waveguide width. Fitting these results, analytic expressions for the loss coefficient and mode area are determined:

$$\alpha(w) = 0.074798 + 188.7e^{-0.68094w} \quad (4.11)$$

$$A(w) = 1.2504 + 4.383w \quad (4.12)$$

Where $\alpha(w)$ is in units of cm^{-1} and $A(w)$ is in μm^2. The fits are found to be good with $R > 0.998$ for both.

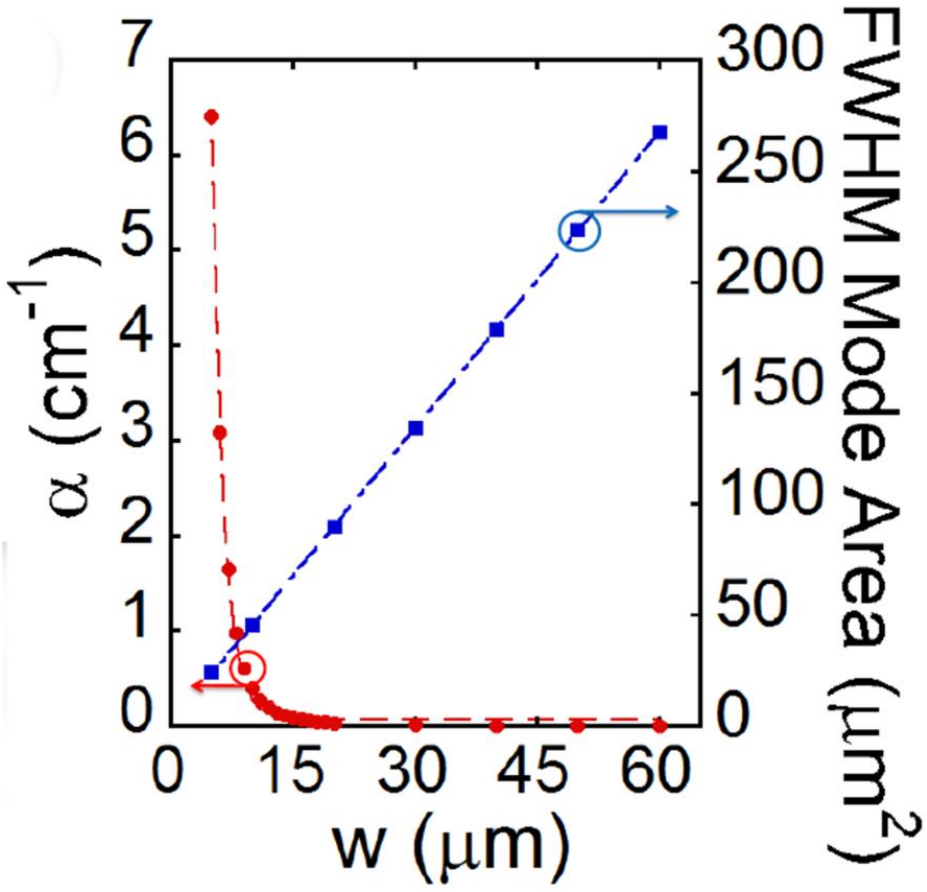

Fig. 4.4 Calculated loss and fundamental mode areas as a function of waveguide width, $\boldsymbol{w}$. These results were fit and used for the simulations discussed in the text.

Using equations (4.11) and (4.12), equation (4.10) can be expressed as a function of z and w:

$$\Delta E_{AC}(w,z) = \frac{\pi c^2 \Gamma}{2\omega_o^3}\left(\frac{1}{\Delta_{1,F}}\right)\frac{P_{in}e^{-\alpha(w,z)z}}{A(w,z)} \qquad (4.13)$$

Equation (4.13) is then used with the Doppler energy shift to satisfy equation (4.8). To do so, an initial waveguide width and input power, P_{in}, is determined and then the waveguide width is solved for at small steps along z. With appropriate initial parameters, the intensity along z can be sustained with varying width such that

equation (4.8) is satisfied along the entire waveguide length to achieve a final speed of 40 m/s. Varying initial temperatures, T_o, were considered. The waveguide designs (w vs. z) for T_o= 30, 50, 70, 90, 110 and 130 ℃ are plotted in Fig. 4.5 (blue, green, red, light blue, purple and gold respectively). A top down view of the waveguide can be seen in the inset of Fig. 4.5 for T_o= 50 ℃.

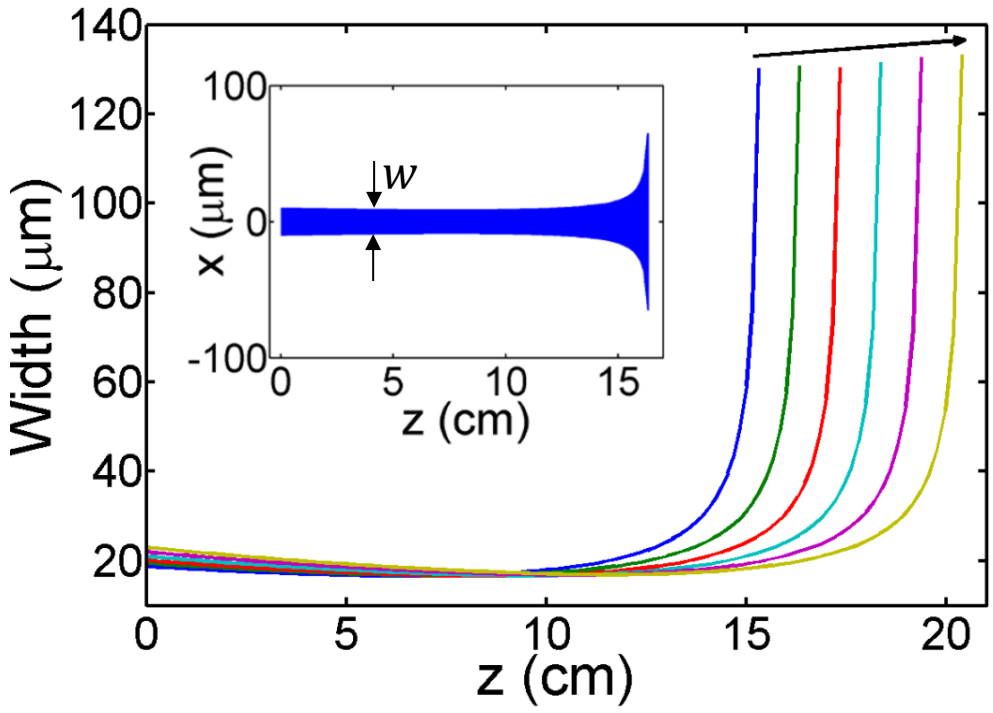

Fig. 4.5 w(z) for T_o= 30, 50, 70, 90, 110 and 130℃ (blue, green, red, light blue, purple and gold respectively). Arrow indicates increasing T_o and the inset shows a top down view of the spatially varying hollow core width for $\boldsymbol{T_o} = 50$℃.

For $\delta_L = -8$ GHz (recall: $\Delta_{1,F} = \delta_L - \vec{k} \cdot \vec{v}$), P_{in} was 2.59, 2.81, 3.02, 3.29, 3.58 and 3.88 mW for $T_o = 30$, 50, 70, 90, 110 and 130 ℃, respectively. Designing the chips to achieve a final mean speed of $v_f = 40.0\, m/s$ corresponds to a final

temperature of 1.47 K which is comparable to results demonstrated with Zeeman slowers. Higher initial temperatures of course result in higher v_o thereby requiring a longer waveguide length in order to cool to the same final speed. The large taper near the end of the waveguide is a result in the necessity to rapidly decrease the optical intensity $I(z) \propto \frac{1}{A(w)}$. Lateral confinement is provided by the gradient force from the AC Stark beam. This prevents transverse heating and results in calculated potential well depths on the order of 50 mK corresponding to maximum transverse captures speeds of ~ 6 m/s for the designed AC Stark laser beam. This provides sufficient lateral confinement along the waveguide [44].

The second design for cooling involves keeping a constant waveguide width (and thus a constant mode area size) and changing only the top ARROW layers. The simplest approach is to vary only the thick top oxide with thickness (d_{TO}). Using equation (4.8) and (4.13) with a constant $\mathrm{A(w,z)} \equiv A_o$ an analytic expression for the required loss along z ($\alpha(z)$) can be derived:

$$\alpha(z) = \left(\frac{1}{z}\right) ln\left(\frac{-\pi c^2 \Gamma \lambda P_{in}}{2\Delta_{1,F}\omega_o^3 A_o h\sqrt{v_o{}^2 - 2az}}\right) \quad (4.14)$$

Using the same initial temperatures as above (T_o = 30, 50, 70, 90, 110 and 130 ℃) in an HC-ARROW with width, $w = 25\mu m$, height, $h = 10\mu m$ and $\delta_L = -8$ GHz, $\alpha(z)$ can be solved for in order to cool ^{23}Na atoms to $v_f = 40.0\ m/s$. Using the transfer matrix formalism (see section 3.2), the appropriate top oxide thickness can be determined along the z-direction $d_{TO}(z)$ to achieve the desired losses.

The necessary loss coefficients were found accessible within a narrow range of d_{TO} (between 5.98 and 6.05 μm). P_{in} was found to be 3.43, 3.59, 3.75, 3.90, 4.06 and 4.21mW for $T_o = 30$, 50, 70, 90, 110 and 130℃ respectively with $\delta_L = -8$ GHz. Fig. 4.6 (a) shows the necessary loss coefficients for varying input temperatures. Fig. 4.6 (b) shows the resulting waveguide design (d_{TO} vs. z) found via the transfer matrix formalism. Fig. 4.6 (c) plots the mean speed along z for the same initial temperatures to $v_f = 40.0 m/s$. Though this approach would result in a difficult fabrication challenge, the simulations suggest that the atoms could be cooled below 40 m/s down to their Doppler temperature, $T_D = \frac{\hbar\Gamma}{2k_B}$ = 235 μK ($v_f = 0.5 m/s$) [36]. Cooling below this temperature is not suitable for HC-ARROWs as they preferentially guide linear polarizations over substantial lengths. This differs from free space experiments where polarization dependent sub-Doppler cooling techniques could be used to reach lower temperatures [10].

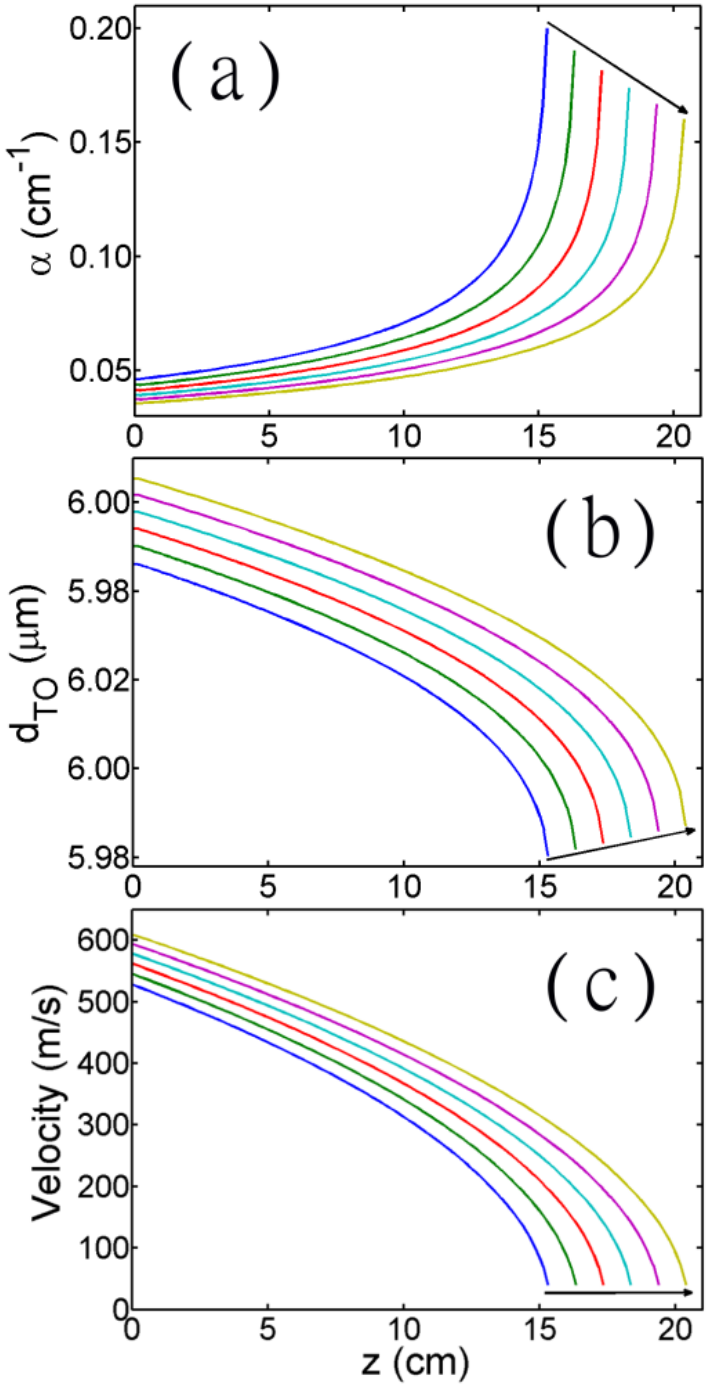

Fig. 4.6 (a) $\alpha(z)$ for T_o= 30, 50, 70, 90, 110 and 130℃ (colors and arrow same as in Fig. 4.4). (b) d_{TO}(z) for varying T_o. (c) $v(z)$ for varying T_o.

4.2 Towards Integrated On-Chip Alkali Waveguides

Using the ARROW platform, both Rb hyperfine spectroscopy [109] and EIT based slow light [29] have been demonstrated. Using these light-matter interactions on-chip with two integrated Rb filled HC-ARROWs could allow for the creation of some photonic devices including Mach-Zehnder interferometers, optical buffers and pulse sequence generators [7]. A cartoon of the proposed device is found in Fig. 4.7 where two hollow-core ARROWs (HC-ARROW, grey) are integrated with a system of solid-core ARROWs (SC-ARROW, green).

To couple the two on-chip Rb cells, SC-ARROW y-junctions are used. The performance of these structures was investigated experimentally and theoretically. Experimentally, many SC-ARROW y-junctions were fabricated with varying half angle, θ (see Fig. 4.8 (a)). The waveguide cross-sectional dimensions were ~ 5 μm x 5 μm and their throughputs were measured at wavelength, $\lambda = 532\ nm$. A sample mode image at the end of a fabricated SC-ARROW y-junction is found in Fig. 4.8 (b). The total transmission through the splitter is given by ${P_{out}}/{P_{in}} = \kappa_c \kappa_B e^{-\alpha L}$ where κ_c is the coupling loss, κ_B is the loss at the y-junction, α is the scattering loss in the waveguide and L is the total length of the waveguide. On the same wafer, straight SC-ARROWs were fabricated, and cutback measurements were performed in order to extract a loss coefficient for the devices, α. Using this value with the experimentally measured chip lengths, the length dependent loss can be extracted

from the y-junction cutback measurements leaving information about the scattering loss at the y-junction, κ_B . The normalized experimental results are found in Fig. 4.8 (c).

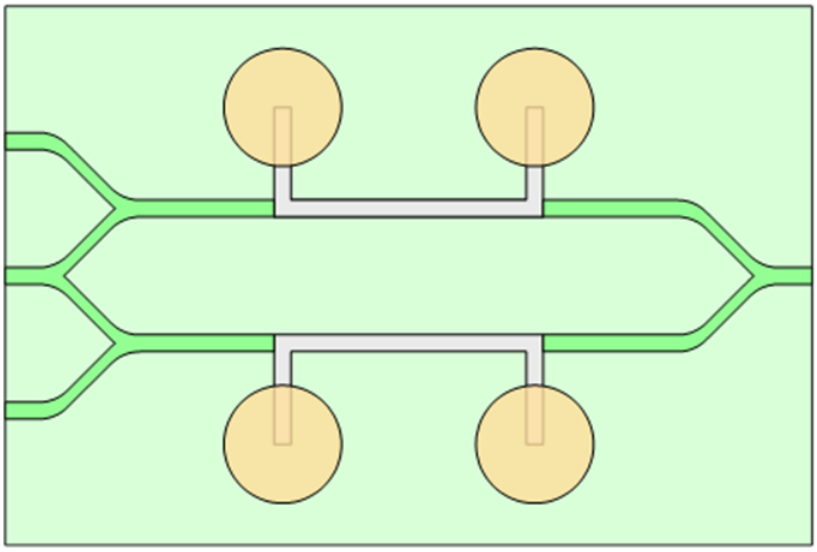

Fig. 4.7 Two HC-ARROWs (grey) are integrated with a system of y-junction SC-ARROWs (dark green). Using this system, light can be launched onto the chip such that it only guides to the upper or lower Rb-filled waveguide or so that it is split and sent equally to the upper and lower Rb-filled waveguide.

The y-junctions were simulated using FIMMWAVE by Photon Design. Fig. 4.8 (a) shows a sample simulated structure and the results for varying θ (red) are plotted along with the experimental results in Fig. 4.8 (c) (blue). Good agreement is found as a function of θ. Therefore, a small half angle is desired in order to keep losses to a minimum. Based on these SC-ARROW y-junction simulations and experiments, the integrated HC-ARROW structures (Fig. 4.7) were fabricated and demonstrated optical guiding as anticipated.

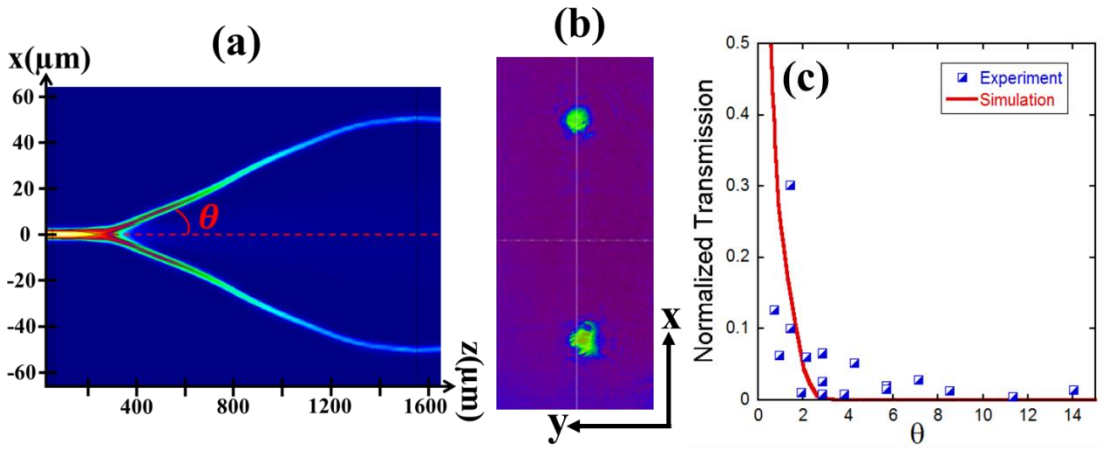

Fig. 4.8 (a) Y-junction simulated in FIMMWAVE with half angle θ. (b) A sample output mode image taken at the edge facet of the waveguide from a fabricated y-junction ($\lambda = 532nm$). (c) Normalized transmission for both the simulated (red) and fabricated structures (blue) as a function θ.

Experimental slow and stored light was achieved in a bulk cell using two narrow linewidth diode lasers (Vescent Photonics, DBR and CECL). Three of the D_1 hyperfine energy levels are used in ^{87}Rb to create large dispersion based on electromagnetically induced transparency (EIT – see section 2.1.4). Storage of light is demonstrated using the lambda energy scheme (see Fig. 2.6) in which the probe (coupling) laser's ground state is the ^{87}Rb $5S_{1/2}$ F = 1 (F = 2) level and the probe and coupling beam share a common excited state, $5P_{1/2}$ (D1) F' = 2. The two lasers are frequency and phase locked together using an offset phase lock servo (Vescent Photonics D2-135 with fast photodetector, D2-160). The master laser was side-locked to the relevant hyperfine energy level using a saturated absorption spectroscopy module (Vescent Photonics, D2-210) and the slave laser was driven to the appropriate frequency spacing (6.8347 GHz) via the offset phase lock servo. Both lasers pass

through a separate acousto-optic modulator (AOM – Brimrose) for beam shaping which is controlled via a function generator (Agilent Technologies 33522A-400) which communicates to a computer for timing of the relative modulations. A description of the experimental setup can be found in Appendix D. The two lasers are orthogonally linearly polarized and combined at a polarizing beam splitter before passing through an ^{87}Rb filled bulk cell. The cell is contained in a heater and is shielded from stray magnetic fields using μ–metal. The beams are separated after the ^{87}Rb cell using another polarizing beam splitter and are detected via a photodetector and oscilloscope.

Experimental slow light is demonstrated in Fig. 4.9 (a) for varying cell temperature. Notice that higher temperatures equate to larger delays but lead to smaller peak amplitudes (more absorption) and larger dispersion (the pulses are more spread out due to a narrowing in the EIT window). The slow light experiment is performed by modulating the probe beam AOM to create a pulse shape (in Fig. 4.9 (a), the pulse full-width half-max is 250 ns and shape is a truncated Gaussian [130]). The storage of light is demonstrated by modulating the coupling beam. To do so, the beam is turned off (at the truncated edge of the probe beam) and is then turned back on at some storage time (τ) later. Fig. 4.9 (b) plots some stored light data for an ^{87}Rb cell heated to 73℃. Pulses are retrieved with decreasing efficiency for longer τ. The efficiency of retrieval is defined by the pulse intensity profiles before and after storage [51]:

$$\eta = \frac{\int_{T}^{+\infty} |\varepsilon_{out}(t)|^2 dt}{\int_{-\infty}^{T} |\varepsilon_{in}(t)|^2 dt} \quad (4.15)$$

Where $\varepsilon_{out}(t)(\varepsilon_{in}(t))$ is the temporal electric field profile for the output (input) pulse. The efficiencies fall off with an exponential decay as a function of τ as seen in Fig. 4.9 (c), where the spin-wave decoherence rate (τ_s) is the fitted decay rate. For the data in Fig. 4.9 (b), the decoherence rate is found to be 1.15 μs. Additionally, the output pulse width is dictated by the retrieved coupling beam intensity. By retrieving pulses with varied optical powers (intensities, since the beam width is not changing), different output pulse widths can be achieved as demonstrated in Fig. 4.9 (d).

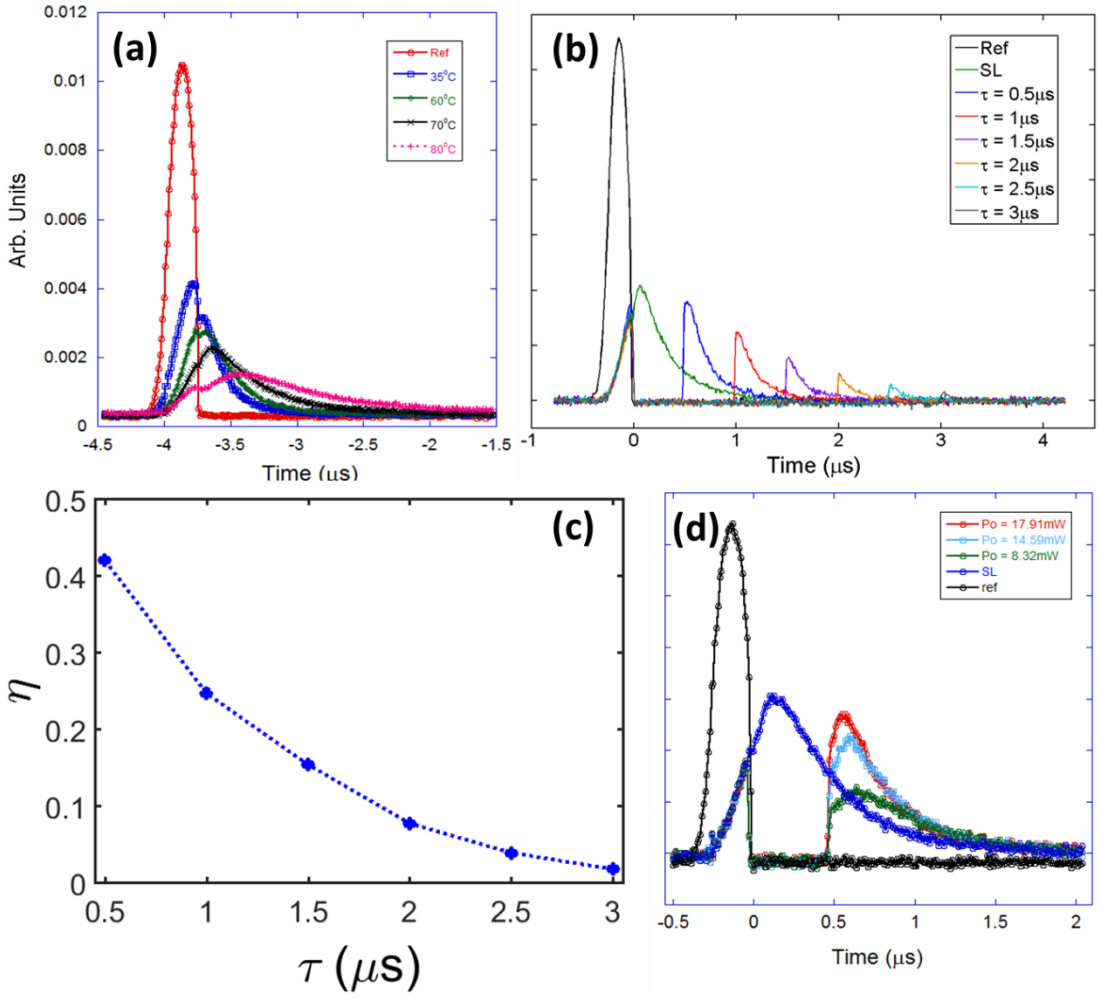

Fig. 4.9 (a) Experimental slow light in bulk ^{87}Rb cell as a function of cell temperature. (b) Stored light results from the same bulk cell heated to 73℃ for various storage times. (c) The efficiencies (η) of the stored light data as a function of storage time (τ) from (b). (d) Demonstration of output pulse width modulation by varying the output power of the retrieval coupling beam. All input pulse widths have a full-width half-max of 250 ns.

Despite optical guiding in chips with the design presented in Fig. 4.7 and the experimental realization of slow and stored light in bulk cell, the photonic devices have yet to be demonstrated experimentally. Loading the fabricated devices with Rb vapor has proven challenging. No vapor was detected on any devices over the course

of these experiments. Therefore, capillary tests monitoring the transport of Rb vapor through high aspect ratio glass channels were performed at Brigham Young University [131], [132]. The results suggest a geometry dependence proportional to L/d^2 where L and d are the length and diameter of the glass capillary as seen in Fig. 4.10 (b). The studies utilized two glass cells separated by a capillary (see. Fig. 4.10 (a)). One cell was loaded with solid Rb and the entire device was vacuumed to pressures below 1 mTorr. The cells were epoxied to copper stubs which were crimped closed after vacuuming down. The devices were heated continually, and an absorption spectrum was taken on the loaded and unloaded sides daily as seen in Fig. 4.10 (a). The time for transport to the unloaded side was defined as the time in which greater than 2% maximum absorption in the D_2 hyperfine spectrum was detected. Studies monitoring varied temperatures and wall coatings were subsequently performed [131]. These results led to the fabrication of novel perforated HC-ARROW devices (see Fig. 4.10 (c)) which did demonstrate absorption spectra with low optical depths [133]. Another study has suggested that incorporation of inert gas (Helium performing the best) assists in transport of Rb through high aspect ratio glass capillaries [34].

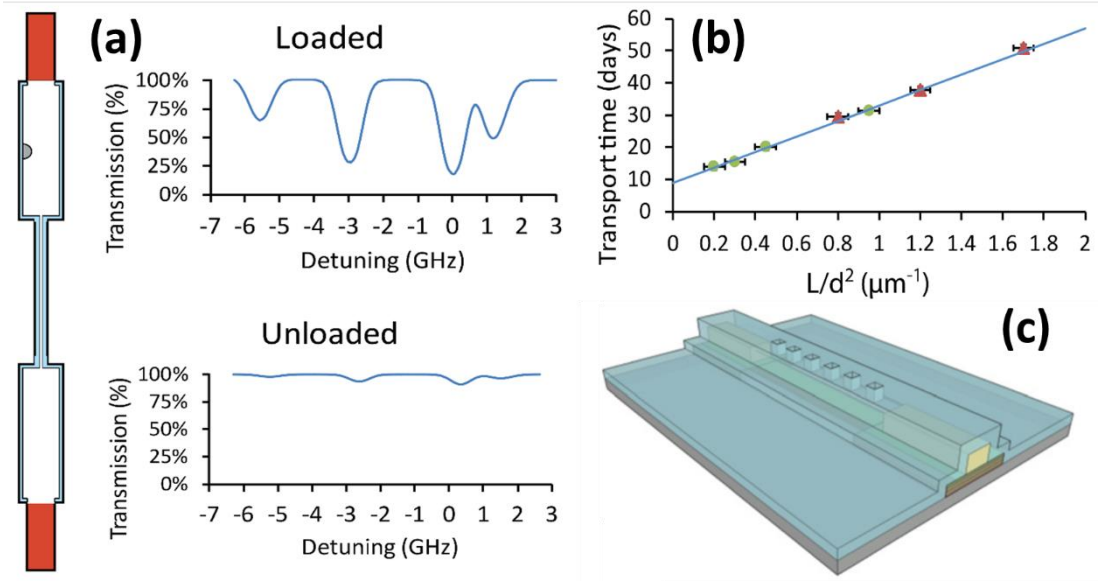

Fig. 4.10 (a) D2 Rb hyperfine absorption spectra in loaded and unloaded sides of capillary device. A cartoon the device is shown left of the absorption plots. The absorption plots were collected daily and transport time is defined as the day where the unloaded absorption spectrum demonstrates more than 2% absorption (max). (b) The transport time is plotted for multiple cells (each data point denotes a separate device; green circles, red triangles denote cell 200 μm and 100 μm diameter capillaries) as a function of L/d^2. From [132]. (c) Cartoon of the perforated ARROW device from [133]. Buried channel solid core optical waveguides are fabricated in-line with a hollow-core ARROW with perforated top oxide. A reservoir is glued on top of the perforated channel and loaded with solid Rb. The device is heated and Rb vapor fills the channel.

Chapter 5

On-Chip Biosensing

This chapter presents two all-polymer optofluidic devices with applications in on-chip biosensing. These devices build upon previous work which demonstrated single particle sensitivities on an oxide-based chip [74]. Inspired by demonstrations of PDMS-based optofluidic functionality [115], the devices presented here are PDMS analogues with chip-scale single particle sensitivity. Further, these devices incorporate engineered fluidic manipulation to both enhance and multiplex the detection of single fluorescent particles on-chip. PDMS allows for rapid prototyping of optofluidic devices and the designs presented here could be implemented on other platforms including oxides. Section 5.1 describes a device which utilizes hydrodynamic focusing to increase the optical collection efficiency off-chip [8]. The collected mean signal amplitudes of single H1N1 viruses were enhanced by ~ 60% with the addition of hydrodynamic focusing. In Section 5.2, a stacked channel design is presented which incorporates an on-chip liquid core multimode interference waveguide for spectral and velocity-based multiplexing of fluorescent particles [9]. Six-fold multiplexing of fluorescent polystyrene beads is demonstrated using three wavelengths. Two-fold multiplexing of single viruses is demonstrated with a single laser.

5.1 Hydrodynamic Focusing for Enhanced Optical Detection

Fluorescence detection on-chip has demonstrated sensitivities high enough to detect single bioparticles such as nucleic acids and single viruses [71], [112]. The optofluidic devices presented in this chapter utilize laser induced fluorescence (see chapter 2) to detect fluorescently labelled single viruses. The most basic PDMS-based optofluidic chip layout for fluorescence detection is found in Fig. 5.1. The chip is comprised of a TIR-based solid- and leaky H_2O filled optical waveguides. The solid-core waveguides utilize TIR for guiding in a rectangular 5:1 structure (see section 3.3). The 5:1 is cladded from the top and bottom by 10:1 PDMS and by air on either side. The H_2O filled leaky waveguides (see section 3.1) allow fluid flow and the capillary sidewalls are fabricated from 5:1 PDMS and are cladded on top and bottom by 10:1 PDMS. Fluorescent particles are pulled through the microfluidic channel via negative pressure (denoted -P in Fig. 5.1). A cartoon of the solid- and hollow-waveguide cross-sections are found on the left of Fig. 5.1. Excitation laser light (denoted by a blue arrow in Fig. 5.1) is launched into a narrow single mode-matched solid-core optical waveguide which guides light to the microfluidic channel and as the fluorescent particles pass through the excitation laser, they fluoresce. The fluorescence is collected perpendicular to the direction of excitation by a wide (~ 15 μm width) multi-mode solid-core optical waveguide (fluorescence denoted by greenarrow in Fig. 5.1). The emission light is collected with a microscope objective and excitation scatter is filtered off-chip before the collected light is launched into a

multi-mode optical fiber and detected on an avalanche photodetector (Excelitas; SPCM-AQR-14-FC). The signals are time-correlated using a Picoquant Time Harp 200, PRT 400 router in time-tagged time-resolved collection mode. The data is processed in Matlab. The resulting signal is a series of peaks in time as seen on the right in Fig. 5.1 (Intensity, I, versus time, t).

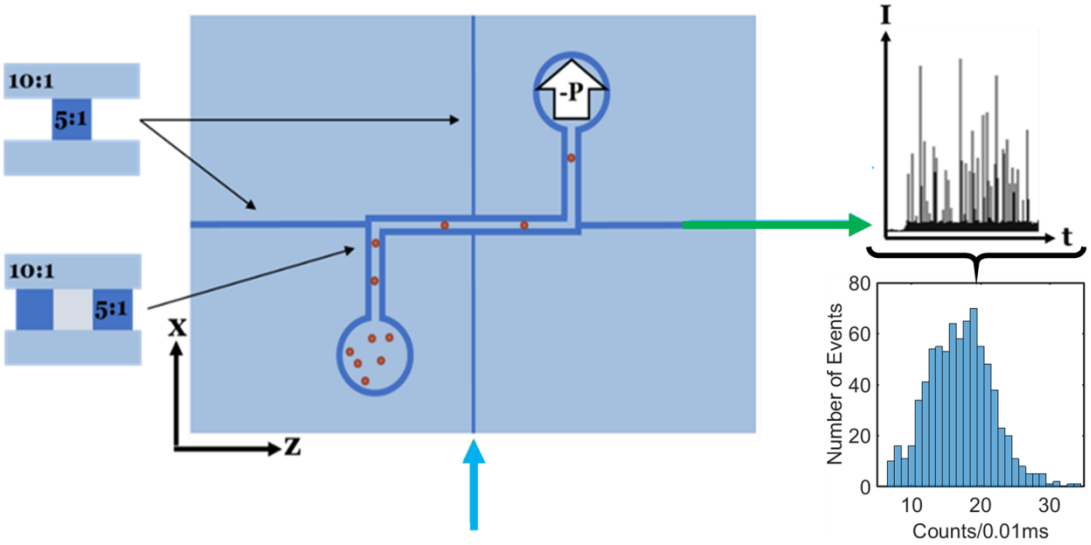

Fig. 5.1 Cartoon of the most basic fluorescence detection PDMS chip. Far left shows cross-sections of the solid (top) and hollow (bottom) waveguides. Fluorescent particles suspended in liquid are pulled through the microfluidic channel via negative pressure (-P at the outlet reservoir). Excitation laser light (blue arrow) in launched into a solid-core waveguide which guides light to the microfluidic channel. As the fluorescent particles pass through the laser light, they fluoresce, and their emission is collected perpendicular to the excitation waveguide (green arrow). The output is filtered and intensity (I) vs. time (t) is detected on an APD. The APD peak signal heights (in units of counts per bin time) result in a peak height histogram with finite standard deviation due to the variation in collection efficiency within the channel.

The collected signal heights are found to be highly dependent on the particle position within the microfluidic channel/leaky optical waveguide [134]. The channel has higher fluorescence collection efficiency if the particles reside closer to the center

of the channel due to the overlap integral of their emission and the guided leaky mode within the waveguide. Therefore, higher collection efficiency can be achieved if the particles flow through the center of the microfluidic channel as they pass through the excitation laser. Collected signal height histograms result in a normal distribution with a finite standard deviation which depends on the varied positions of the particles within the channel as seen in Fig. 5.1. As discussed in Chapter 2, the device in Fig. 5.1 will produce a parabolic distribution of particle speeds across the entire cross-section of the microfluidic channel which do not mix within the channel (laminar flow). Hydrodynamic focusing (HDF) of the particles can be utilized to tailor the particles' position within the microfluidic channel and shrink the velocity distribution [56], [93], [91]. The quality of the detected signals is quantified by the coefficient of variation (CV) [93]. The CV is calculated by dividing the standard deviation of the signal height distribution by the mean. The lower the CV, the more discernible different particle species will be.

To incorporate HDF into a similar device as the one in Fig. 5.1, a system of three input channels was fabricated to provide focusing of fluorescent particles within the main microfluidic channel. This system of channels was designed in-plane with a system of solid-core optical waveguides as in Fig. 5.1. A cartoon of the HDF optofluidic device is found in Fig. 5.2 (a) where the solid-core waveguides are shown in black and the microfluidic channels are shown in blue. Three input reservoirs are denoted (1, 2 and 3) which combine after a distance and run to a single outlet which is driven by negative pressure (experimentally measured at an in-line gauge, -35 inHg).

Fluid from reservoirs 1 and 2 intersect before a ninety degree bend which is designed to provide out of plane (y-direction) focusing of the particles due to the creation of a Dean vortex [135]. In-plane HDF is provided by a channel offset and a sheath flow from fluid flowing from reservoir 3. For the experimentally available negative pressures and the microfluidic cross-sectional areas and lengths, the flow speeds are not high enough to provide a Dean vortex. However, in-plane focusing is experimentally achievable as seen in Fig. 5.2 (b) where a microscope image was taken at the microfluidic intersection (see the dashed box in Fig. 5.2 (a)) when reservoir 2 is filled with food dye and reservoirs 1 and 3 are filled with deionized (DI) water (acting as the buffer).

Fluorescence is induced using an Argon Ion laser (488 nm) which is first coupled to single mode fiber (Newport, FS-V) and then launched onto the chip via the single mode-matched excitation solid-core waveguide (SC_1, cross-sectional dimensions ~ 6 μm x 5.5 μm). SC_1 guides light to the microfluidic channel where particles pass through the excitation laser and their fluorescence ($\lambda_{emision}$) is collected by a multi-mode solid-core waveguide (SC_2, cross-sectional dimensions ~ 6 μm x 12 μm) perpendicular to the direction of excitation. A picture of the experimental setup is found in Fig. 5.2 (c). The chip is mounted on the chip mount and an LED is used to align the collection objective. The LED light is guided to the collection objective via a removable 50/50 beam splitter ("BS"). A flip mirror is then used to image the chip facet on a CCD camera. This alignment ensures that the collected light is coupled into a multi-mode optical fiber ("MMF") after the collected

light is passed through an optical filter ("Filter") when the BS and flip mirror are moved from the collection path. The MMF guides the filtered, collected light from the chip to an avalanche photodetector ("APD") for detection. Once the chip is aligned, the excitation laser light is launched onto the chip using a single mode optical fiber ("Input Fiber"). A vacuum line running to the building's wall vacuum (and controlled with an in-line valve) is attached to the chip prior to initial alignment. A mode image collected from SC1 after it has passed through the HDF chip is found in Fig. 5.2 (d). The device with vacuum line attached is found in Fig. 5.2 (e) with the device sitting next to a dime for scale. The device's footprint is less than 8 mm x 8 mm and three droplets of water can be seen atop of reservoir's 1, 2 and 3. The device is filled via negative pressure at a single output provided by the vacuum line. A close-up image of the device after alignment in the experimental setup is found in Fig. 5.2 (f). The input optical fiber and collection objective are aligned, and the vacuum line is attached. A scale bar is included for scale. The HDF devices were used to detect fluorescence from both commercially available fluorescent polystyrene beads (FluoSpheres, 500 nm diameter, yellow-green) and single H1N1 viruses tagged with AlexaFluor 488.

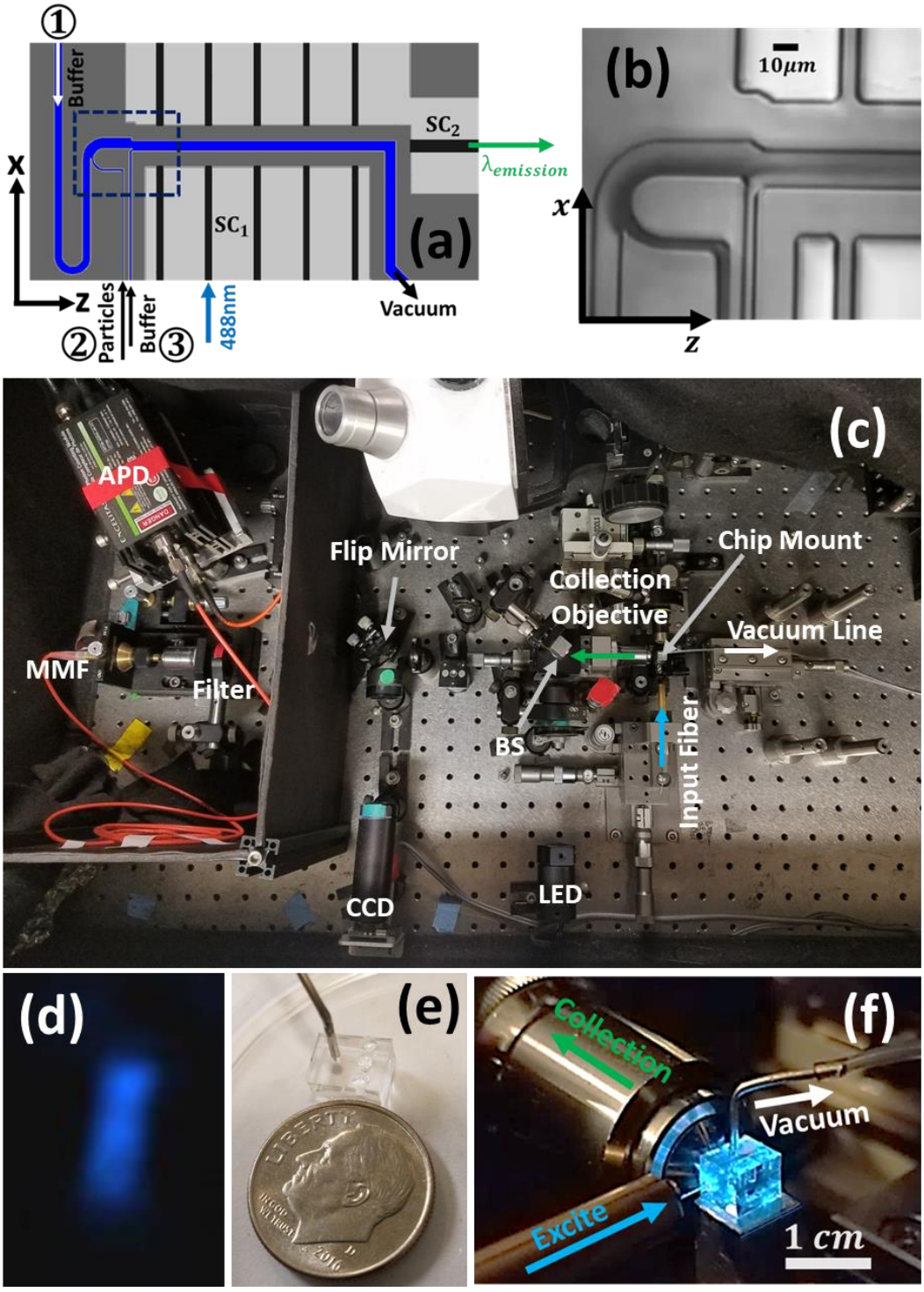

Fig. 5.2 (a) Schematic of the HDF optofluidic device. Microfluidic channels (solid-core waveguides) are shown in blue (black). Three input reservoirs: 1, 2 and 3 are

connected via a system of microfluidic channels and fluid flow is provided by a single outlet driven by negative pressure (vacuum). For focusing, reservoirs 1 and 3 are filled with a buffer and reservoir 2 is filled with a particle solution. Excitation laser light (488 nm) is guided to the microfluidic channel via solid-core 1 (SC_1) and fluorescent emission ($\lambda_{emission}$) is collected off-chip by the orthogonal solid-core 2 (SC_2). (b) A microscope image of a device (region denoted by the dashed box in (a)) demonstrating lateral focusing. Reservoir 2 is filled with food dye and reservoirs 1 and 3 are filled with deionized water. (c) The experimental setup. The chip is aligned to a collection objective and the excitation source (Argon Ion laser coupled into single mode optical fiber) is aligned to the device. Negative pressure is provided by a flexible line which runs to wall vacuum. An LED is used to backlight the chip facet. The collection objective is aligned with the backlight and a CCD camera. The collected light is filtered and then coupled into a multi-mode optical fiber which guides the light to an APD. (d) A mode image taken of the excitation light guided through SC_1 on the optofluidic device. (e) An image of the chip after filling. Reservoirs 1, 2 and 3 are seen with droplets of liquid which have been through the device via the outlet (vacuum line provides negative pressure). The device is smaller than 8 mm x 8 mm (dime for scale). (f) An image of the PDMS device with scale bar. The input laser, collection objective and vacuum line are aligned.

Enhanced detection with HDF was quantified using polystyrene beads. Fluorescent signals were collected in the chip-plane as described above and for the bead experiments, a top-down video was also collected at the excitation region. The avalanche photodetector (APD) traces were used to monitor the collected signal height statistics and to determine CV with and without focusing. The top-down videos allowed for x-z plane particle tracking. A still image from both a control and experiment video (without and with HDF) is found in Fig. 5.3. Images of the excitation region with the lights on are found on the left. Stills from the relevant videos are shown on the right. For the control, two beads are clearly seen near the top and bottom of the channel. In the experiment video, a single bead is found nearer to the center of the channel. These videos are analyzed to create particle position

histograms for the control and experiment (see Fig. 5.6; the Matalb script for the video analysis can be found in Appendix E).

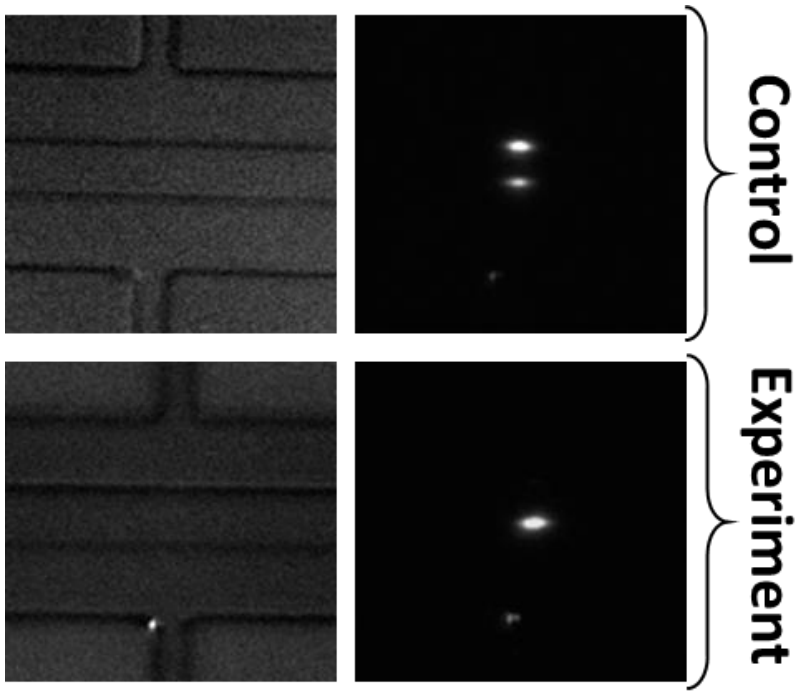

Fig. 5.3 Still images from the collected videos for the control and experiment (without and with HDF). A reference image of the excitation region with the lights on is shown on the left. A single still for the runs are shown on the right. For the control, two particles are seen in a single still image. These particles reside near the top and bottom of the channel (no focusing). For the experiment, a single particle is found nearer to the center of the microfluidic channel when focusing is present.

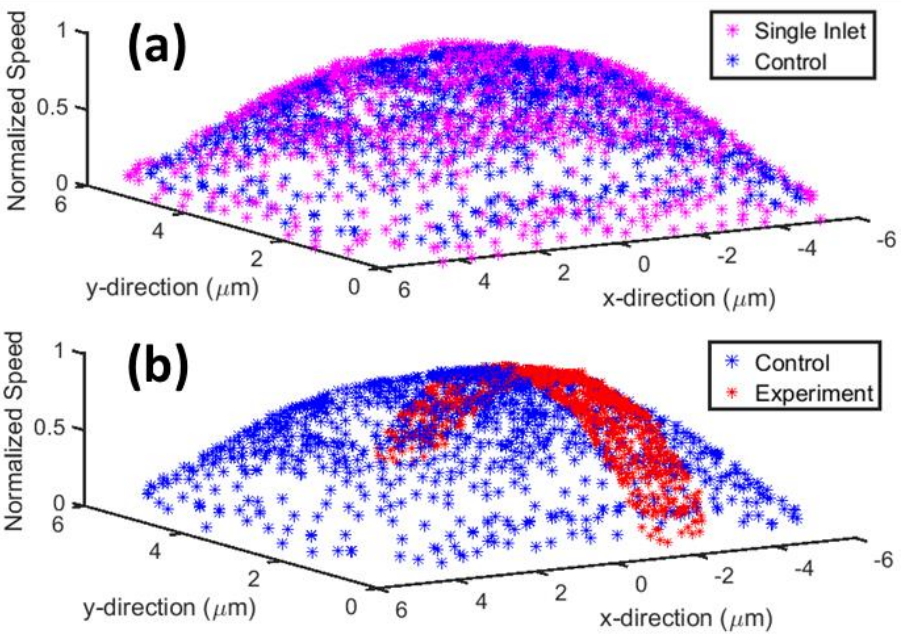

Fig. 5.4 (a) COMSOL particle simulations for a single and triple inlet device. The normalized output speed profiles are the same for both, justifying the control experiment used for the HDF experiment in which bead solution is pulled through all three input reservoirs. Within the main microfluidic channel, the speed profile is the same as a single inlet device would produce. (b) The same control data is plotted with a simulated HDF experiment in which particle solution is only input into reservoir 2 and reservoirs 1 and 3 contain a buffer. The results from (b) comprise the histogram data presented below (Fig. 5.5 (d)).

As a control experiment, a bead solution was pulled through the device from all three input reservoirs (all bead concentrations were 3 x 10^7 beads/mL). If a single inlet were present (as in Fig. 5.1), then a parabolic velocity profile would exist throughout the microfluidic channel. In the HDF structure, the same parabolic velocity profile will exist in the final microfluidic channel (after the three inputs are combined). The purpose of the three inlets is to selectively insert particles to a smaller cross section of the final microfluidic velocity profile. This is true for experiments in which laminar flow is present. Fig. 5.4 shows results for a series of simulations

performed in COMSOL. The normalized speed profiles were collected at the end of a single inlet device (Fig. 5.1) and a triple inlet device (Fig. 5.2). Since the full channel lengths would take an unreasonable amount of time to run, smaller channel lengths were simulated with realistic input speeds. Fig. 5.4 (a) shows the normalized speed results for both the single inlet and triple inlet cases in which bead solution is introduced into all inlets, justifying the choice of the control experiment. Fig. 5.4 (b) shows the same control data found in (a) along with a simulation of the HDF experiment in which beads are only inserted into reservoir 2 and buffer is input to reservoirs 1 and 3. The particles clearly reside in a smaller portion of the velocity profile and are focused near the center of the channel. The offset from the center is due to an inadequate sheath flow from reservoir 3 and could be ameliorated with a higher flow speed. As demonstrated below, these results match well with the experimental results.

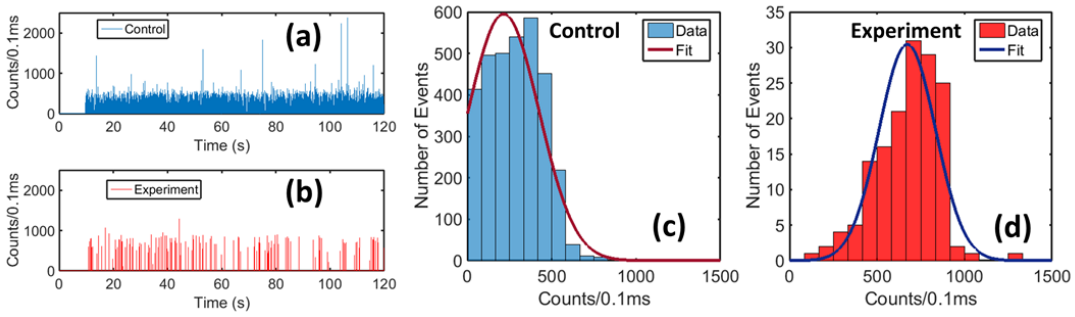

Fig. 5.5 (a) Raw control and (b) experiment (without and with HDF) APD traces collected when exciting 500 nm diameter fluorescent polystyrene beads. The resulting signal height histograms for the (c) control and (d) experiment are plotted with normal distribution fits. The fitted parameters result in CV of 0.98 and 0.24 for the control and experiment demonstrating enhanced detection with the addition of HDF.

The resulting fluorescent polystyrene bead control (bead solution in all three inlet reservoirs) and experiment (with HDF, bead solution only input to reservoir 2) APD traces are found in Fig. 5.5 (a) and (b), respectively. Of interest are the statistics of the detected signals for the control and experiment. Therefore, the APD signal heights are plotted as peak height histograms as seen in Fig. 5.5 (c) and (d). These histograms were fitted with a normal distribution and the fitted mean and standard deviations were used to determine the resulting CVs. The fitted mean and standard deviations for the experimental data were found to be 673.0 and 161.7 counts per 0.1 ms bin time. For the control, the fitted mean and standard deviations were found to be 214.4 and 210.6 counts per 0.1 ms bin time. The resulting CVs are 0.98 and 0.24 for the control and experiment respectively. With the addition of HDF, an improvement in CV is found to be a factor of 4.1 and the fitted mean is increased by a factor of 3.1, demonstrating significant enhancement of optical detection on-chip with HDF.

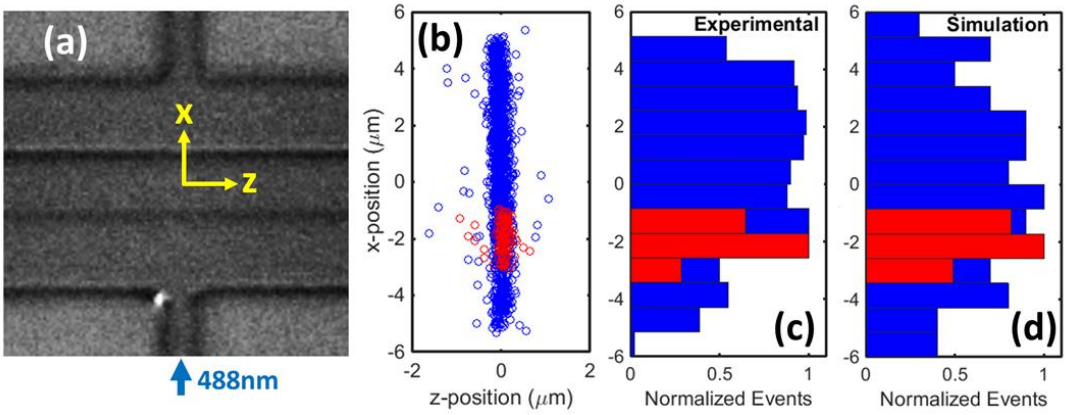

Fig. 5.6 (a) Microscope image of the excitation region with relevant axes (x-z plane). Excitation laser light (488 nm) is guided along the +x-direction and the fluorescent particles travel in the +z-direction. Videos are recorded at the excitation region while the raw APD traces for the control and experiment (see Fig. 5.3 and 5.5) were

collected. The videos were analyzed in Matlab (script found in Appendix E) and the particle positions upon fluorescing is plotted in (b) for the control (blue) and experiment (red). The particles are more focused in the x-plane with the addition of focusing as expected. (c) Shows the resulting x-position histograms from the data in (b) for the control (blue) and experiment (red). Simulated x-position histograms (d) are created from COMSOL simulations (see Fig. 5.4 (b)) and match well with the experimental results from (c).

While the APD traces of Fig. 5.5 (a) and (b) were being collected, a top-down video at the excitation volume was collected simultaneously. The videos were analyzed in Matlab to track the particle positions in the x-z plane for the control and experiment (script in Appendix E). Fig. 5.6 (a) shows a still image of the excitation region where the videos were recorded. The excitation laser was coupled into SC1 and the light was guided in the +x-direction. The beads are pulled through the device along the +z-direction. The videos can be found in the supplemental material in reference [8]. The control (blue) and experiment (red) particle positions as they pass through the excitation laser are plotted in Fig. 5.6 (b). Both control and experiment particle positions are found to reside in a small z-distribution due to the finite width of the excitation laser's mode, demonstrating effective optical guiding in the excitation waveguide. For the control (blue), the particles are found across the entire channel width as expected, whereas in the experiment (with HDF), particles are focused to a small x-distribution just off-center. These results are plotted as experimental data x-position histograms in Fig. 5.5 (c). The COMSOL simulated particle positions (see Fig. 5.4) are plotted as an x-position histogram in Fig. 5.6 (d) and the resulting simulations match the experimental results well.

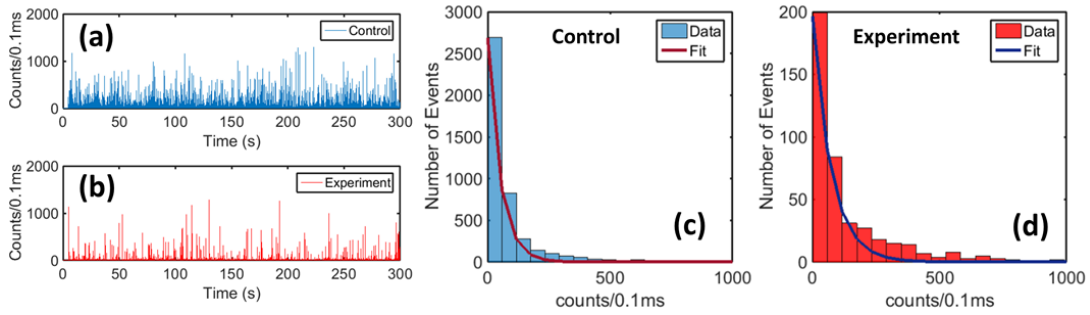

Fig. 5.7 (a) Control and (b) experiment APD traces for fluorescently labelled H1N1 viruses. The signal peak height histograms for the (c) control and (d) experiment are plotted with exponential decay fits. The mean signal height for the control and experiment are 94.8 and 155.9 counts per 0.1 ms, demonstrating an enhanced signal height detection of a factor 1.64.

The above experiments validate the hypothesis that HDF enhances the detection of laser induced fluorescence signals on-chip. Of greater practical interest is the detection of nanoscale biomolecules. To that end, single H1N1 viruses were non-specifically tagged with Alexa Fluor 488 dye and the analogous optical experiments were performed. Explicitly, a control was performed by pulling virus solution through the device from all three input reservoirs and the HDF experiment was performed by pulling virus solution from reservoir 2 and buffer (nuclease-free water) was pulled from reservoirs 1 and 3. The collected APD traces for the control and experiment are found in Fig. 5.7 (a) and (b), respectively. The resulting signal height histograms are found in Fig. 5.7 (c) and (d). Notice that a full normal distribution is not visible which is due to the smaller number of fluorophores per virus than in the case of the polystyrene beads. Therefore, only the tail end of the distribution is detected. The histograms are fit with an exponential decay with fitted decay rates of 0.020 and 0.014 in units of 0.1 ms bin time per counts for the control and experiment. Since a

standard deviation cannot be fit, the CV for both traces cannot be determined. However, the mean signal heights were found to be 94.8 and 155.9 counts per 0.1 ms for the control and experiment. Thus, an enhanced mean signal height of a factor 1.64 is demonstrated with the addition of HDF to the optofluidic device.

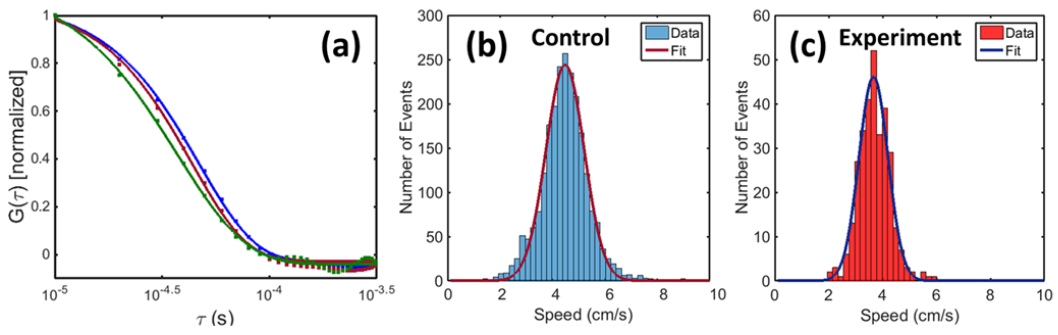

Fig. 5.8 (a) Three sample normalized autocorrelation traces (symbols) with fits (lines) from the control APD trace (Fig. 5.6 (a)). Speed histograms with normal fits for the (b) control and (c) experiment signal heights. The fitted mean and standard deviation are 4.5 and 0.73 cm/s for the control and 3.7 and 0.54 cm/s for the experiment. This demonstrates a narrower velocity distribution on-chip with the addition of HDF.

Lastly, though the full normal distribution of the signal heights cannot be detected, the velocity distributions were found using fluorescence correlation spectroscopy (FCS). This is done by comparing the time scales of autocorrelations of fluorescent signals to the time it takes for a particle to pass through an excitation volume. To do so, a model which incorporates the excitation beam profile in our devices is utilized [111]. For each peak in the APD traces (Fig. 5.7 (a) and (b)), an FCS autocorrelation trace, $G(\tau)$, was fit to extract the virus's speed [136], [110], [111]. Fig. 5.8 (a) shows three sample normalized autocorrelation traces with fits from within the control data. The resulting speed histograms with normal fits for the

control and experiment are found in Fig. 5.8 (b) and (c). The fitted mean speeds were found to be 4.8 and 3.7 cm/s for the control and experiment, respectively. The slower mean is anticipated as the focused particles are flowing off-center in the microfluidic channel and thereby don't flow with the maximum speed (center of the parabolic speed distribution, see Fig. 5.4). The standard deviations are 0.73 and 0.54 cm/s for the control and experiment which demonstrates a shrinking of the velocity distribution in the case of HDF as anticipated.

Therefore, HDF is found to increase the optical collection efficiency of fluorescence signals from an optofluidic device. Additionally, these devices were found to have sufficient sensitivity to detection single fluorescently labelled viruses (a first for this type of device). The enhancement was evident for lateral, off-center focusing. Better focusing (in the x- and y-dimensions) would result in decreased velocity distributions and better optical collection efficiency. Though here the device is implemented using PDMS, the design could be fabricated using silicon or other materials.

5.2 Stacked Channel Devices for Spectral and Velocity Multiplexing

As demonstrated in the above section, PDMS optofluidic devices can be used to detect fluorescently labelled single viruses. The ability to multiplex the detection of single viruses is appealing for clinical applications. Spectral multiplexed detection of single viruses has been demonstrated on an oxide-based optofluidic device using

ARROWs [74]. Spectral multiplexing is achieved by using a multi-mode interference (MMI) waveguide as the excitation source as opposed to a single input waveguide as was used in the HDF device presented in section 5.1. The on-chip MMI waveguide can be designed to produce different *N* integer number of spots at the analyte channel for different excitation wavelengths (see chapter 2, equation (2.47)). Intersecting the MMI waveguide with two analyte channels along different lengths, *L*, can produce two different *N* integer spot patterns for a single laser. Using this approach, spatial multiplexing of fluorescent particles is possible. Combining spectral and spatial MMI waveguide based approaches, six-fold multiplexing of single viruses has been demonstrated on an oxide-based ARROW device [75].

In this section, a PDMS optofluidic device is presented which utilizes a liquid-core MMI waveguide and a stacked analyte channel design to provide spectral and velocity multiplexing of single viruses or higher throughput for the same sample. A single MMI spot pattern intersects two separate microfluidic channels across which the same spot pattern is preserved. By applying different negative pressures to the two channel's outlets, fluorescent particles can flow through the channel with different mean speeds. By analyzing the APD traces, the particle velocities can be determined and thereby their channel of origin can be discerned. Alternatively, this device can be used to increase the throughput of the optofluidic device by flowing particles through the stacked channels at the same speed.

The liquid-core MMI waveguide was designed to produce *N* number of spots at a fixed length, *L* [for width, w, L(w = 50, 75 and 100 μm) = 825, 1,860 and 3,290

μm, respectively] for three different wavelengths, λ: N = 9, 8, 7 spots for λ = 488, 556 and 633 nm respectively. The devices were designed to be filled with ethylene glycol ($n \approx 1.43$) and therefore guide via total internal reflection. The MMI waveguides were simulated using FIMMWAVE software by Photon Design and include the wavelength dependent index of refraction for both ethylene glycol [137] as well as both 10:1 and 5:1 PDMS [116]. The lengths over which the desired spot patterns are preserved ($\equiv \Delta L_N$) was modelled with varying parameters in FIMMWAVE. Three MMI waveguide widths were modelled = 50, 75 and 100 μm at the three design wavelengths of 488, 556 and 633 nm (N = 9, 8, 7). A sample top-down image of the modelled intensity profile is found in Fig. 5.9 (a). The intensity profiles of each structure were exported into Matlab and the number of spots along the direction of propagation (z-direction) were found using a peak finding algorithm (findpeaks.m with 'MinPeakHeight' set to 0.35 of the normalized profile). A 3D intensity profile imported into Matlab is found in Fig. 5.9 (b) (as in (a), a 50 μm wide MMI waveguide modelled at 633 nm). The results showed the anticipated number of spots near the length predicted from equation (2.47). The length along the z-direction in which the designed N number of spots was preserved was defined as ΔL_N as seen in Fig. 5.9 (a). As predicted by equation (2.47), a wider MMI waveguide requires a longer length (L – see Fig. 5.9 (c)) and thus a larger chip footprint. However, wider (and longer) MMI waveguides result in larger ΔL_N (see Fig. 5.9 (d)). This would allow for a larger number of analyte channels to pass through the excitation pattern and allow for increased multiplexing capabilities. Though the devices were simulated at room

temperature, it is found that the length required to keep a set spot number (N = 8 at 556 nm) when considering ethylene glycol's thermal expansion coefficient and temperature dependent index of refraction varies less than ΔL_N (for a 50 μm wide MMI waveguide, the required length varies 15.8 μm < 70 μm) for a temperature range in which water is liquid (0 ℃ to 100 ℃).

Experimentally, it was found that MMI waveguides of width 100 μm or larger would collapse slightly under vacuum and therefore their spot patterns were distorted. The input field profile size determines the lower limit of the MMI waveguide width. For example, our input solid-core waveguide (which delivers light on-chip to the liquid core MMI waveguide) is mode-matched to Newport FS-V fiber (which we use to couple all input light into the device) and has a width of 5.5 μm which guides a mode with $1/e^2$ width of ~ 4.9 μm. Thus, if one wants to resolve N number of spots, a waveguide width must measure at least ~ N*4.9 μm. The devices presented here have maximum N = 9 and therefore, 50 μm width MMI waveguides are on the lower limit of resolvable patterns. Therefore, the experiments below utilized both 50 μm and 75 μm wide MMI waveguides.

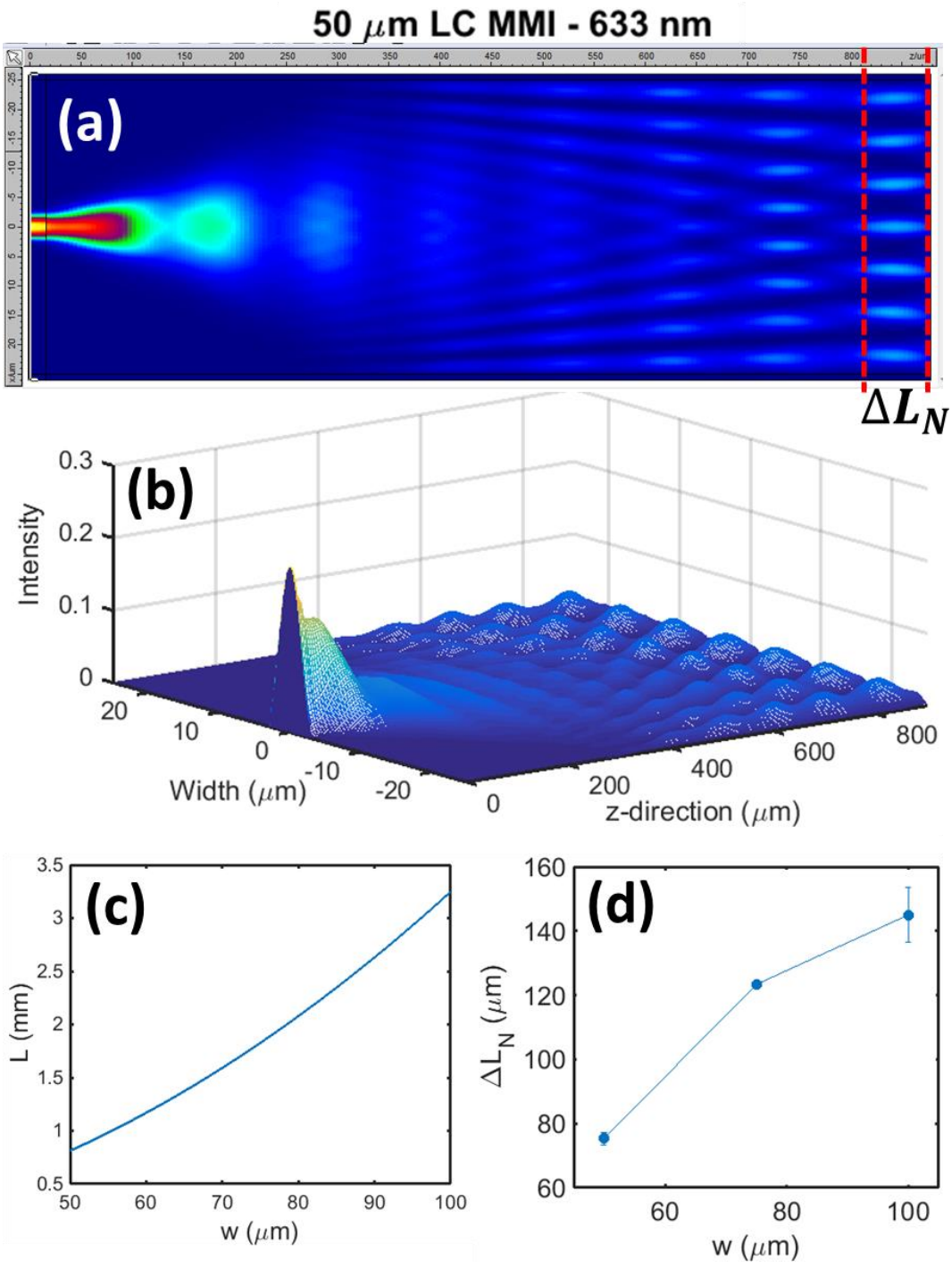

Fig. 5.9 (a) A sample top-down intensity profile from FIMMWAVE for a 50 μm wide liquid core MMI waveguide with input solid-core waveguide modelled at 633 nm. (b) The full 3D profile is imported to Matlab for analysis of the desired spot number

length, ΔL_N. To keep a set number of spots for a given waveguide, the length (L) must change as a function of width (w) as dictated in equation (2.47). This relationship is plotted in (c) and demonstrates that wider width waveguides will need to have a longer length in order to preserve N spots at a given wavelength. (d) ΔL_N as a function of w found from simulating three MMI waveguide widths in FIMMWAVE. The data are averages from the three design wavelengths (488, 556 and 633 nm).

A cartoon of the full device can be found in Fig. 5.10 (a) where the MMI liquid-core MMI waveguide is seen to perpendicularly intersect two fluidic channels 1 and 2 (Ch_1 and Ch_2). All three microfluidic channels (the MMI waveguide, Ch_1 and Ch_2) have separate inlets and outlets. By applying varied negative pressures to the outlets of Ch_1 and Ch_2, the mean velocities of the particles can be controlled. Solid-core waveguides are denoted in black and guide input laser light (λ_{in}) to be guided to the liquid-core MMI waveguide. A multi-mode solid core waveguide (with 35 μm which tapers to the edge of the chip) intersects both Ch_1 and Ch_2 and is used to collect emitted fluorescence (λ_{emit}). Both the solid-core waveguides (black in Fig. 5.10 (a)) and 5:1 microfluidic channel sidewalls (grey in 5.10 (a)) are fabricated with 5:1 PDMS. An image of an actual unfilled device is found in Fig. 5.10 (c) which has a 50 μm wide MMI waveguide.

Fig. 5.10 (b) shows the to-scale simulated spot pattern for $\lambda_{in} = 633\ nm$ (N = 7) in the region denoted by a dashed box in Fig. 5.10 (a). This simulation included not only the liquid-core MMI waveguide, but also the crossing channels Ch_1 and Ch_2. The N = 7 spot pattern is maintained across both Ch_1 and Ch_2. To quantify the experimental spot patterns across Ch_1 and Ch_2, an aqueous quantum dot solution

(dissolved in water, band gap at 665 nm) was pulled through Ch_1 and Ch_2. Fig. 5.10 (d), (e) and (f) show the resulting spot patterns for the three design wavelengths, 488, 556 and 633 nm respectively. The resulting spot patterns produce the expected number of spots (*N*) and the results from 5.10 (f) match the theoretical patterns (Fig. 5.10 (b)) well. Therefore, the device works optically as designed, preserving the intended spot pattern across both Ch_1 and Ch_2.

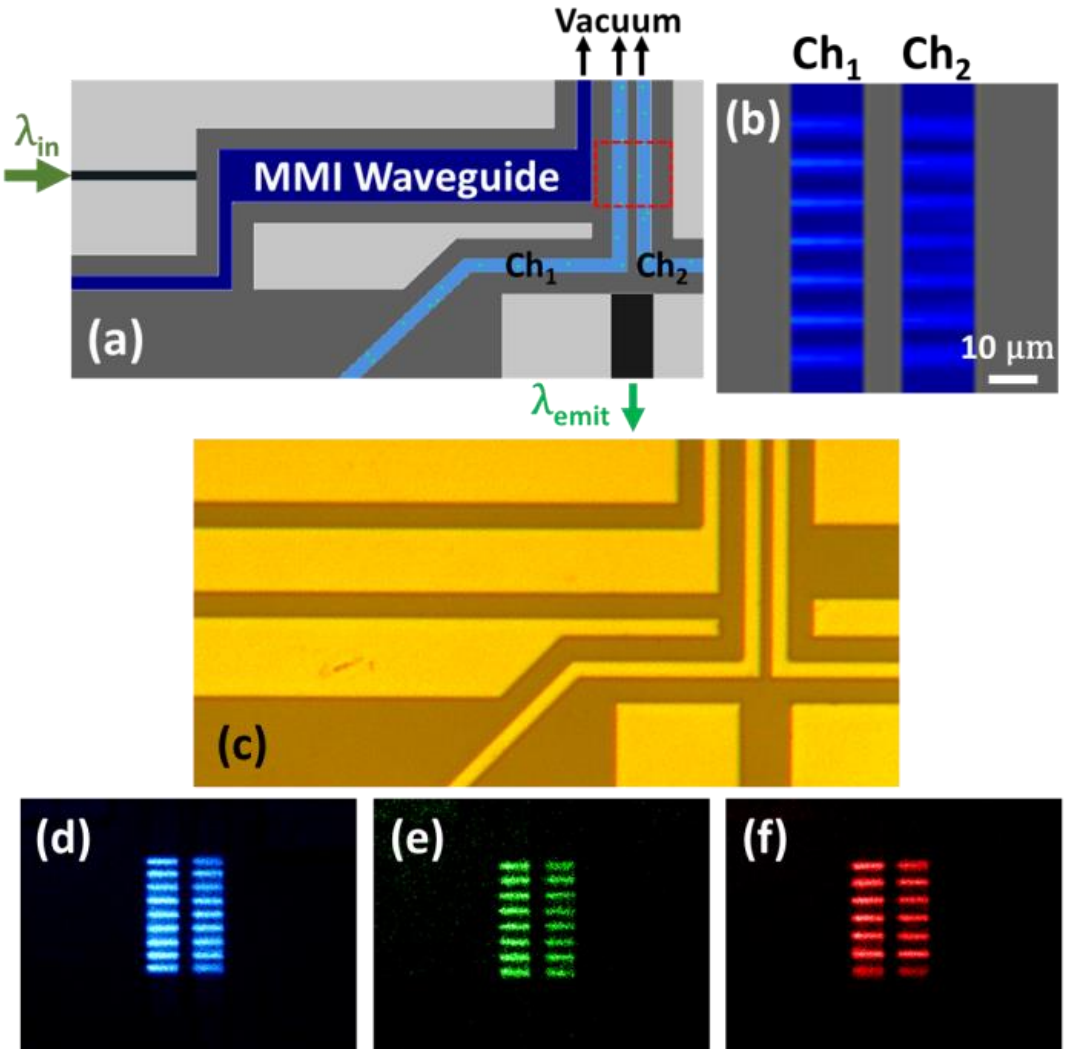

Fig. 5.10 (a) Schematic of the stacked channel PDMS optofluidic device. A liquid-core MMI waveguide is used to induce N = 9, 8 or 7 spots at two particle channels (Ch_1 and Ch_2) for λ_{in} = 488, 556 or 633 nm, respectively. Solid-core optical waveguides are shown in black and are used to guide light to the MMI waveguide and to collect fluorescence emission (λ_{emit}) from the chip. (b) Simulated MMI waveguide spot patterns at Ch_1 and Ch_2 for λ_{in} = 633 nm (N = 7) drawn to scale. The region on the full device is denoted by a red dashed box in (a). An optical microscope image of an unfilled 50 μm wide liquid core MMI waveguide device is shown in (c). Experimental spot patterns are collected by filling Ch_1 and Ch_2 with quantum dots (emission at 665 nm) and collecting their emission from top-down with a microscope when λ_{in} = (d) 488, (e) 556 and (f) 633 nm. The experimental spot patterns show the anticipated number of spots. The theoretical spot pattern (b) matches the experimental pattern (f) well for λ_{in} = 633 nm.

To test the full devices, a mixture of 1 μm diameter fluorescent polystyrene beads (FluoSpheres yellow-green 505/515, orange 540/560 and crimson 625/645) with concentration ~ 10^6 mL^{-1} was used to monitor the fluorescence at the three design wavelengths. MMI waveguide spot pattern fidelity and enhanced throughput were tested by collecting bead APD traces in which a single channel and both channels Ch_1 and Ch_2 were filled with bead solution. These data were collected for single wavelength excitation while both Ch_1 and Ch_2 were being driven by the same negative pressure (-35 inHg). The results are summarized in Fig. 5.10 for λ_{in} = 488, 556 and 633 nm in rows 1, 2 and 3, respectively. The first column shows the data in which only Ch_1 is filled with bead solution (Ch_2 is filled with deionized water); column two shows the data where both Ch_1 and Ch_2 were filled with bead solution and were pulled through their channels at -35 inHg; column three shows a sample MMI waveguide spot pattern from the APD trace with nice profiles demonstrating the anticipated N number of spots for each wavelength. The number of particles found in

the 488, 556 and 633 nm traces for single/double channel detection were 300/755, 183/392 and 193/289 demonstrating a factor of 2.5, 2.1 and 1.5 more particles detected over a ~ 30 second data trace while running bead solution through both analyte channels. Thus, the device demonstrates nice MMI waveguide pattern s in the collected APD traces (Fig. 5.11, column 3) and ~ 2x throughput is demonstrated when pulling a bead solution through both channels.

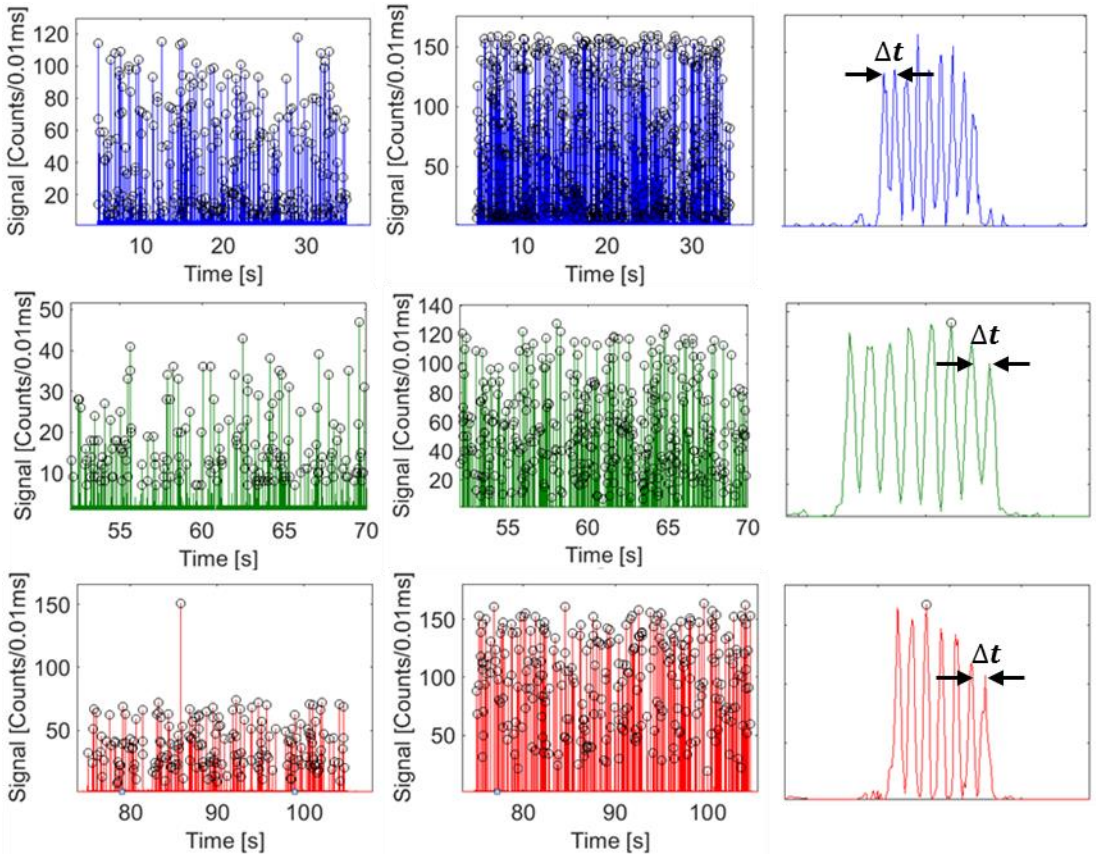

Fig. 5.11 Demonstration of enhanced throughput using the stacked channel design. Rows 1, 2 and 3 correspond to the single excitation wavelength used: 488 nm, 556 nm and 633 nm, respectively. Column 1 is data taken when only Ch1 is filled with bead solution and Ch2 is filled with deionized water. Column 2 is data collected when both Ch1 and Ch2 are filled with bead solution. Double the detected beads are anticipated. The number of detected beads is enhanced by a factor of 2.5, 2.1 and 1.5 for 488 nm, 556 nm and 633 nm respectively. Column 3 shows a zoomed in sample

of the signal for the corresponding wavelength (by row) demonstrating nice pattern fidelity and the anticipated N number of spots. The difference in time between the N peaks is denoted as Δt and can be used to determine particle speeds.

As discussed in Chapter 2, the particles flowing through a rectangular microfluidic channel with speeds provided by the negative pressures available to us experimentally will result in a distribution of particle positions and speeds within the channel cross-section. The flow is laminar (no mixing) and the velocity profile of the fluid flow is parabolic. Therefore, there exists a velocity distribution of particles travelling in a channel driven by negative pressure. To quantify these speed histograms, a series of APD traces were collected for all three design wavelengths as a function of experimentally measured negative pressures (Ch_1 filled with bead solution and Ch_2 filled with deionized water). Speeds were determined by taking the time difference (Δt) between the MMI waveguide signal peaks (see column 3 in Fig. 5.11) and the spatial separation (Δz) of the excitation pattern peaks (e.g. the spacing between peaks as seen in Fig. 5.10 (d), (e) and (f)). The speed is then calculated by $|\boldsymbol{v}| = {\Delta x}/{\Delta t}$. The resulting histograms for the negative pressure series for all three wavelengths are found in Fig. 5.12. The speeds were determined for experimental negative pressures of -35 inHg, -20 inHg, -10 inHg and -5 inHg. The pressures were measured at an in-line gauge running between the chip and the vacuum pump. The histograms do overlap for some of the profiles. However, separation between these histograms is found for -35 inHg and -10 inHg (assuming no clogging takes place). By separating the speed histograms, Ch_1 and Ch_2 can be driven at varying pressures

and the particle's position can be determined by velocity (e.g. was the originating signal from Ch_1 or Ch_2?).

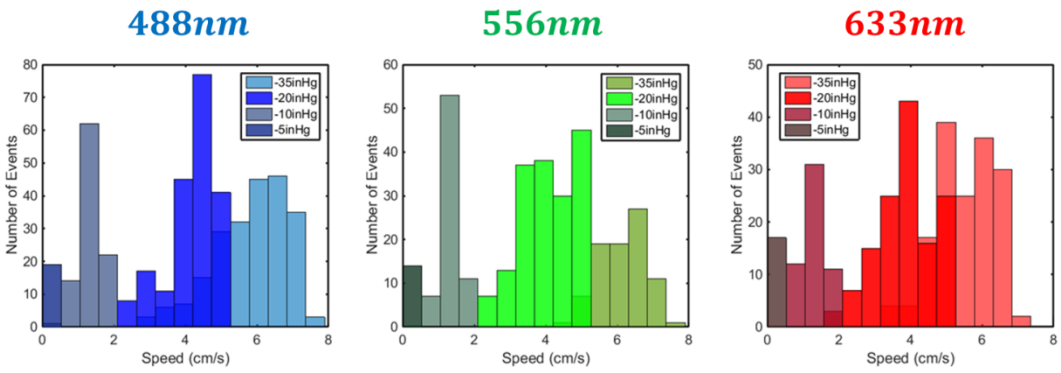

Fig. 5.12 Speed histograms for different single excitation wavelengths (488, 556 and 633 nm) for varying experimentally measured negative pressures. These experiments were performed when a single channel was filled with a fluorescent bead mixture.

To demonstrate velocity multiplexing, a series of APD traces were taken in which both Ch_1 or Ch_2 were filled with a fluorescent bead solution and were driven at -35 and -10 inHg, respectively. Single wavelength excitation traces were collected, and the speeds were determined as described above. Fig. 5.12 (a) shows a sample APD trace when 488 nm is used to excite a 50 μm wide MMI waveguide resulting in 9 spots. The time trace shows two sets of N = 9 spots traveling with notably different velocities. The resulting speed histograms are found in Fig. 5.13 (b) for the three excitation wavelengths. The histograms show a bimodal distribution with a separation between distributions at 3 cm/s (dashed line in Fig. 5.13 (b)). This threshold speed was chosen to distinguish the channel of origin for the fluorescence signals (Ch_2/Ch_1 if the particle speed is less/greater than 3 cm/s as denoted in the histograms).

Therefore, for a single excitation wavelength, two-fold multiplexing is possible based on velocity.

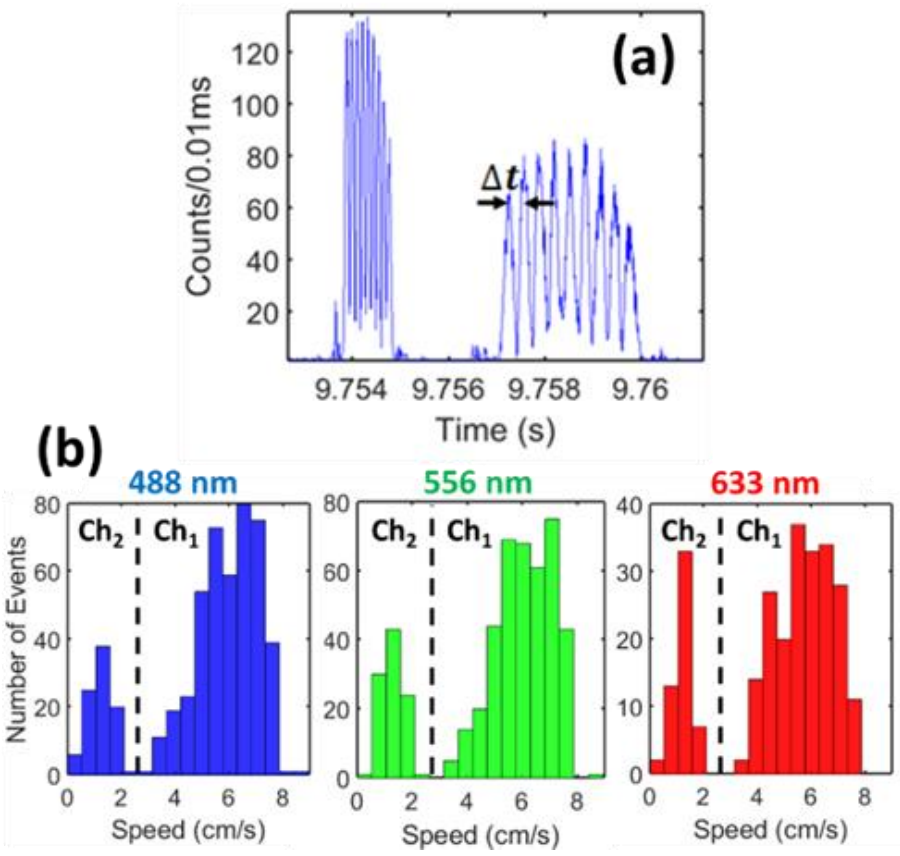

Fig. 5.13 (a) A sample of the APD trace collected with excitation wavelength of 488 nm from a 50 μm wide MMI waveguide device. Ch_1 and Ch_2 are driven at -35 and -10 inHg, respectively. Clearly, there are two sets of $N = 9$ spots with varied particle speed. From the single excitation wavelength APD traces, the color dependent speed histograms are compiled as seen in (b). There is a clear separation in the bimodal histogram at 3 cm/s (dashed line) which allow discrimination of the channel in which the particle was travelling upon excitation.

Six-fold multiplexing is demonstrated by launching all three excitation wavelengths into the device and running Ch_1 and Ch_2 at -35 and -10 inHg, respectively. The resulting APD trace is found in Fig. 5.14 (a) in which the particles

have been labelled by excitation wavelength color (488 nm = blue, 556 nm = green and 633 nm = red) and by speed ("Slow" or "Fast denoting speed less or greater than 3 cm/s). Above a noise threshold (found by running a control in which deionized water flows through both Ch_1 and Ch_2), particles are found. The color is assigned based on the number of peaks (N = 9, 8 or 7) found in each particle trace. Once N is determined, the anticipated spatial separation (Δz) can be determined and the speed is calculated. The speeds are then categorized as "Slow" or "Fast" based on each particle's speed in relation to the threshold (3 cm/s). The resulting speed histograms by excitation color are plotted in Fig. 5.14 (b). The results show good agreement with a similar bimodal trend for all three excitation wavelengths. Additionally, a comparable number of particles are found for each excitation color as anticipated. There is a total of 664 particles found in the ~ 30 second long APD trace. Over 95 % of the peaks are assigned with 34.3, 28.5 and 32.7 % of the particles identified as blue, green and red, respectively.

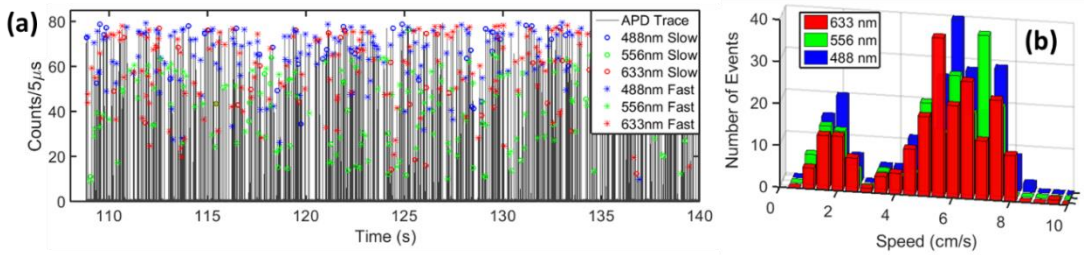

Fig. 5.14 (a) Six-fold multiplexing APD trace with labelled particles. Each peak is assigned a color (blue, green and red = 488, 556 and 633 nm excitation wavelength) and speed ("Fast" or "Slow" if greater or less than 3 cm/s). (b) The resulting speed histograms by excitation wavelength.

Lastly, two-fold multiplexing of single viruses is demonstrated using a single excitation wavelength (556 nm). H3N2 and H1N1 viruses are labelled with Cy3 fluorescent dye and pulled through a device with a 75 μm wide MMI waveguide. H3N2 (H1N1) solution is pulled through Ch_1 (Ch_2) at -35 (-20) inHg. A 10 minute long APD trace was collected and the resulting speed histogram is found in Fig. 5.15. The inset shows a portion of the raw APD trace in which two single H3N2 and H1N1 traces are shown with clearly different speeds. The bimodal distribution shows that the mean speeds in Ch_1 and Ch_2 were 7.43 cm/s and 1.33 cm/s, respectively. The histograms clearly show two separate distributions demonstrating effective velocity multiplexing. The concentrations of the virus solutions were approximated to be $9.09\ x\ 10^4\ mL^{-1}$ and $7.39\ x\ 10^5\ mL^{-1}$ for H3N2 and H1N1, respectively.

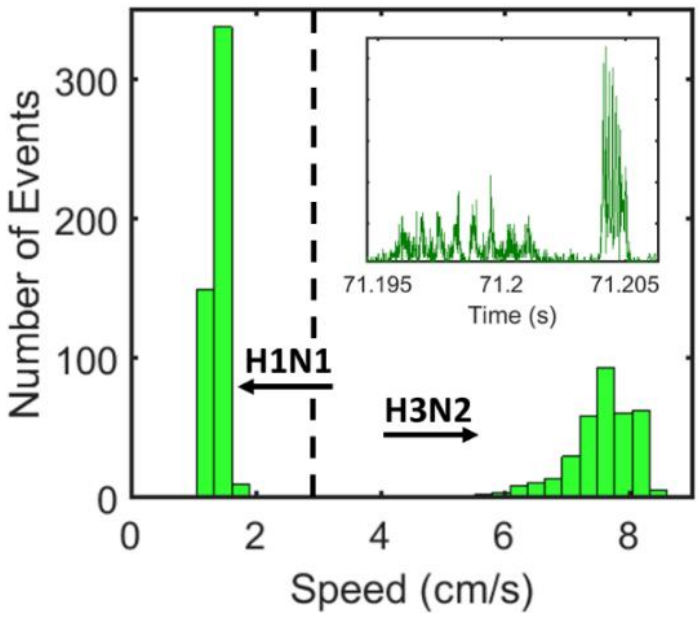

Fig. 5.15 Speed histograms for H3N2 and H1N1 virus driven at different negative pressures (speeds). Two clear subpopulations exist, demonstrating unambiguous

assignment of a particle to either Ch_1 or Ch_2. The inset shows a portion of the ten-minute-long APD trace in which a single H3N2 and H1N1 particle are clearly visible.

Thus, a new optofluidic approach to multiplexed detection was demonstrated using a liquid core MMI waveguide with a stacked channel design. Both velocity and spectral multiplexing allowed for six-fold multiplexing of fluorescent polystyrene beads. Additionally, the devices demonstrated single virus sensitivity. Two-fold multiplexing of single H3N2 and H1N1 single viruses was demonstrated using a single excitation wavelength. The device can alternatively be used to double the throughput of sample through such an optofluidic device. Here, the devices were fabricated using PDMS, but the design is amendable to other chip-scale platforms (e.g. other polymers or silicon). Certain device parameters could be changed in order to optimize the level of multiplexing possible. For example, narrower analyte channels could be used or a wider MMI waveguide could be used to increase the spot length as discussed above. Additionally, as seen in section 5.1, HDF could be implemented into the chip designs to decrease the velocity histogram widths and thereby increase the multiplexing capability.

In conclusion, this chapter has demonstrated that PDMS-based optofluidic devices are capable of detecting fluorescence signals with single bioparticle sensitivities. By incorporating hydrodynamic focusing into the standard laser induced fluorescence layout, particles can be forced to a region with higher optical collection efficiency. Thereby, enhanced optical detection was demonstrated in the case of both fluorescent polystyrene beads as well as with fluorescently labelled single viruses.

Additionally, a novel stacked channel design was incorporated with a liquid core MMI waveguide for simultaneous spatial and velocity-based multiplexing. Six-fold multiplexing of fluorescent polystyrene beads was demonstrated with three excitation wavelengths. Two-fold multiplexing of single H3N2 and H1N1 viruses was presented with a single excitation wavelength.

Chapter 6

Optofluidic Distributed Feedback Dye Laser

A critical component in the devices discussed within this dissertation is a coherent light source (laser). The lasers utilized for the previously mentioned results were all commercially purchased and were coupled to an optical fiber for launching light onto the chip-scale devices. The field of lab-on-chip seeks to create chip-scale devices which incorporate all necessary laboratory components. Therefore, it is desirable to create on-chip laser sources. There have been a host of approaches to creating on-chip dye lasers including the use of Fabry-Perot cavities on-chip [138], ring resonators [83], [139]–[141] and distributed feedback (DFB) structures [77], [79], [80], [97], [142]–[144]. The majority of these devices utilize Rhodamine 6G (R6G) dye for the gain medium as it can be dissolved in a number of solvents and has a high quantum yield [145].

The energy levels of an R6G dye molecule are depicted in Fig. 6.1 and lasing is achieved in a four-level system. As discussed in chapter 2, vibrational and rotational sublevels exist within a single singlet state. The dye molecules are excited from the ground singlet state $(S_0, 0)$ to an excited singlet state $(S_1, 3)$ via a pump laser. Non-radiative decay to an excited singlet state $(S_1, 2)$ occurs on the time scale of a

few picoseconds ("ps" in Fig. 6.1). From the relaxed excited state ($S_1, 2$), stimulated or spontaneous emission to a vibrational/rotational ground singlet state ($S_0, 1$) can occur. The spontaneous emission lifetime is ~ 5 ns. Finally, fast (a few picoseconds) non-radiative decay to the ground state ($S_0, 0$) occurs. In reality, however, intersystem crossing can occur to the triplet ground state, T_1 on the time scale of ~ 100 ns for R6G [76]. Evolution into the triplet state removes molecules from population inversion and also allows for absorption of emitted light into higher level triplet states. To prevent dye molecules from entering a triplet state, the dye solution is moved quickly through the excitation pump, triplet state quenchers may be added to the dye solution and pulsed pump sources are used (e.g. pulsed lasers with temporal width < 100 ns).

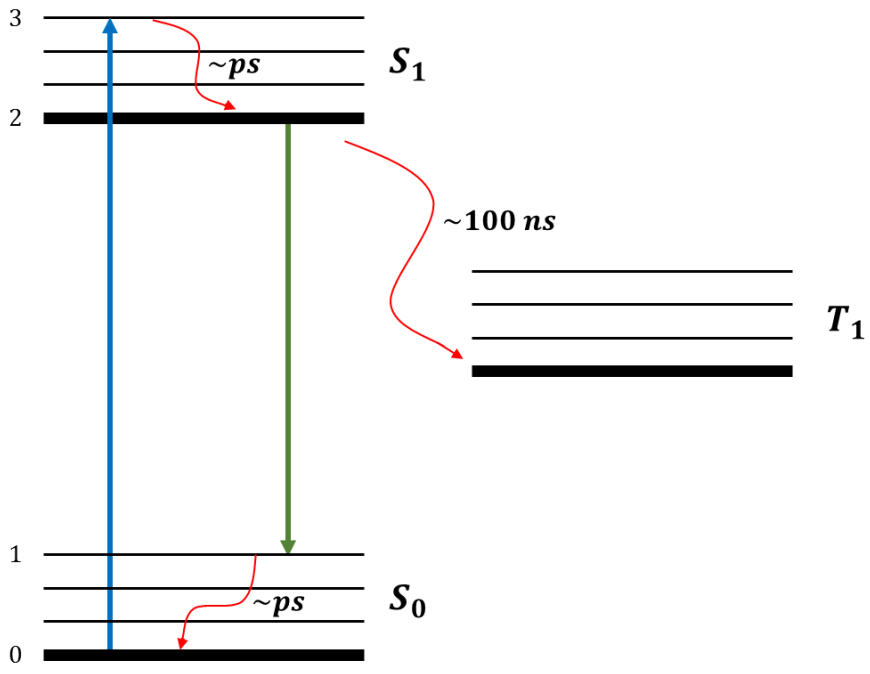

Fig. 6.1 Four-level energy system used to achieve lasing in a dye gain medium. The dye molecules are excited from the ground state $(S_0, 0)$ to a ro-vibrational excited state $(S_1, 3)$. Non-radiative decay takes place from $(S_1, 3)$ to $(S_1, 2)$. From $(S_1, 2)$, spontaneous or stimulated emission relaxes the molecule to $(S_0, 1)$. From $(S_0, 1)$, the molecule relaxes non-radiatively back to the ground state. Non-radiative decay occurs on the order of a few picoseconds. The spontaneous emission lifetime is 5 ns. Intersystem crossing may occur to an undesired triplet state, T on the order of 100 ns.

Here, a novel liquid core on-chip DFB dye laser is presented which utilizes a liquid R6G solution within a corrugated sidewall microfluidic structure. The DFB structure provides optical feedback by a periodic variation in the effective index of refraction provided by the corrugated sidewall. Such modulations in refractive index result in wavelength specific reflections which can be used to create the laser cavity. This chapter discusses the design methods for the devices and the demonstration of lasing in sections 6.1 and 6.2, respectively.

6.1 Design Methods

Equation (2.52) gives the Bragg condition ($2n_{eff}\Lambda = m\lambda_m$) required for reflections to occur in a periodic refractive index. Recall the variation in refractive index as seen in Fig. 2.13 (a). The index of refraction goes from a higher to lower value periodically with a periodicity of Λ along the z-direction. The m^{th} order resonances satisfying equation (2.52) specify the wavelengths which will be reflected in the structure and the spacing between subsequent m^{th} order resonances is called the free spectral range (*FSR*) and is given by equation (2.53) $\left(FSR = 2n_{eff}\Lambda\left(\frac{1}{m-1} -\right.\right.$

$\frac{1}{m}\right)\right)$. Fig. 6.2 shows the relationship between the m^{th} order resonances and *FSR* as a function of periodicity (Λ) for various wavelengths for light propagation in ethylene glycol ($n \approx 1.43$).

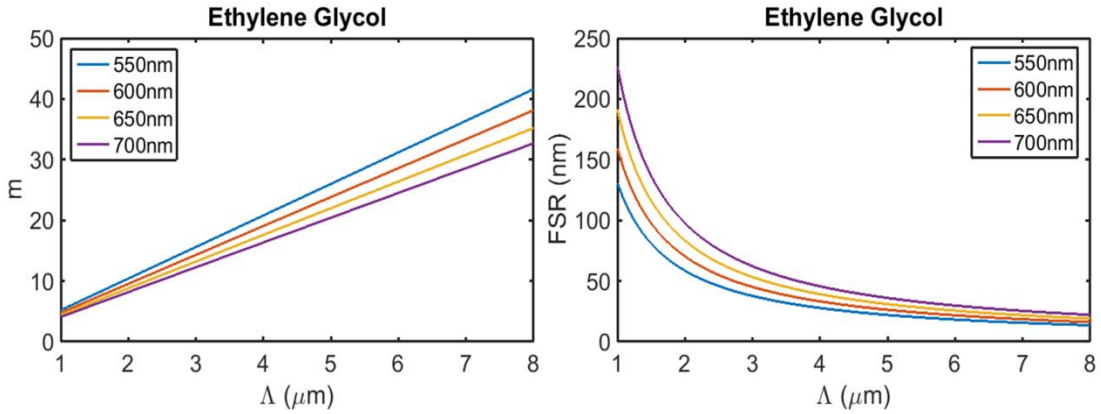

Fig. 6.2 m^{th} order resonances (left) and *FSR* as a function of characteristic Bragg spacing, Λ, for various wavelengths (blue, red, yellow and purple = 550, 600, 650 and 700 nm, respectively). *m* increases with Λ and *FSR* decreases with Λ.

A cartoon of the corrugated sidewall structure from top-down is found in Fig. 6.3 (a). The channels are to be filled with a high refractive index solution (here, ethylene glycol) in which a fluorescent dye is dissolved (R6G). The variation in the core width due to the corrugated sidewall profile results in a variation in the effective index of refraction (analogous to Fig. 2.13 (a)), thereby allowing for wavelength dependent Bragg resonances. If an m^{th} order reflection exists in the cavity at a wavelength commensurate with the dye's emission profile, it can provide feedback (reflections along the length of the channel) of the fluorescence such that lasing may be achieved. The R6G emission profile has a peak around 580 nm and spans ~ 50 nm

(e.g. see Fig. 6.8). Therefore, a cavity with a resonance near 580 nm and an *FSR* greater than 50 nm is desirable.

To model the device's transmission spectra, Rouard's method was employed [146], [147]. This method reduces the three dimensional microfluidic structure into a one-dimensional problem in which the transmission matrix formalism is used to calculate the reflectively provided by the periodic effective index (see section 3.2). The corrugated sidewall channel is comprised of two repeated structures, WG_1 and WG_2, as denoted in Fig. 6.3 (b). The cross-sections of these two structures are found in Fig. 6.3 (c). The corrugated sidewall results in a variation of the microfluidic channel's width which modulates between w_o to $w_o + 2d$ along the z-direction.

To use Rouard's method, first the effective indices of WG_1 and WG_2 must be determined. To do this, the structure is decomposed into three vertical slices comprised of three index layer segments – one with ethylene glycol (the liquid in which the R6G dye will be dissolved) surrounded by 10:1 PDMS, n'_{core}, and the other with 5:1 PDMS surrounded by 10:1 PDMS as the sidewalls are, $n'_{sidewall}$. Lastly, the structure's approximate effective index is determined using a three layer structure with n'_{core} surrounded by $n'_{sidewall}$ (see appendix F for more on the effective index method). A table of effective indices for WG_2 is found in Table 6.1 for varying grating depths, d and x-polarization. The unmodulated width, w_o, is 5.5 μm and the difference in the effective indices between WG_1 and WG_2 are included. The effective indices of WG_1 and WG_2 are then simulated as a stack of periodic dielectric layers with thickness $\Lambda/2$. Therefore, for a waveguide with total grating

length L, the simulation will multiply $2L/\Lambda$ transmission matrices to determine the reflectivity of the structure. Scanning the wavelength, the relevant reflections are determined and the cavity is approximated. Simulations were carried out to predict the anticipated fundamental mode wavelength dependent transmission spectra for various design parameters. Note that the wavelength dependent Sellmeier coefficients were used for ethylene glycol [137] as well as both 5:1 and 10:1 PDMS [116].

$\boldsymbol{d}$ $(\boldsymbol{\mu m})$	0	1.0	2.5	5.0
$\boldsymbol{n_{eff}}$	1.430533	1.430837	1.431028	1.431146
$\boldsymbol{\Delta n}$ $(\mathbf{x\ 10^{-4}})$	0	3.04	4.95	6.13

Table 6.1 A summary of x-polarized effective indices for the design optofluidic cross-sections (see Fig. 6.2, WG_1 and WG_2). w_o = 5.5 μm and the grating depth, d, is varied. The difference in effective indices is taken between the unmodulated and modulated width cross-section.

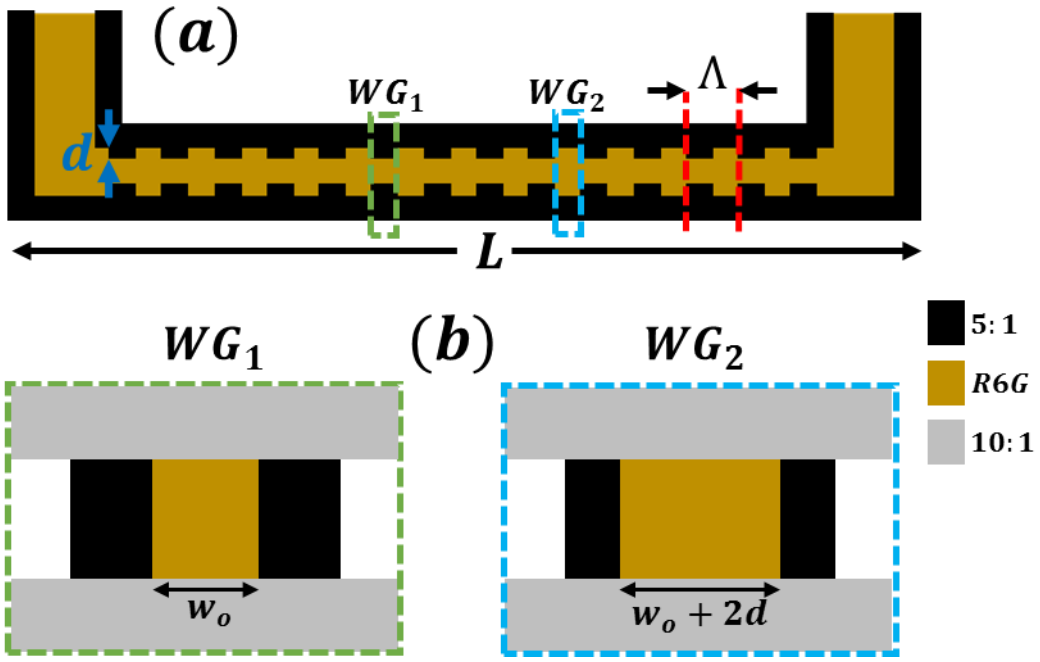

Fig. 6.3 (a) A top-down cartoon of the corrugated sidewall structure. R6G is dissolved in a high index liquid (e.g. ethylene glycol) which fills the corrugated sidewall microfluidic channel. The R6G solution is shown in gold and the 5:1 PDMS sidewalls are black. The grating depth and length are d and L. The corrugated sidewall creates a varied waveguide structure which alternates between WG_1 and WG_2 with periodicity Λ. (b) A cartoon of the two waveguide structures, WG_1 and WG_2 where gold, black and grey denote the R6G solution, 5:1 and 10:1 PDMS, respectively. The waveguide width varies between w_o and $w_o + 2d$ resulting in a periodic variation in effective index of refraction.

The resulting transverse electric field fundamental mode transmission spectra using Rouard's method are found in Fig. 6.4 for several device parameters ($\Lambda = 6, 8, 10\ \mu m;\ d = 5.0\ \mu m;\ \Delta n \approx 6\ x\ 10^{-4}$ – see Table 6.1). The large wavelength scans are shown on the left of Fig. 6.3 and a zoomed in resonance for each structure is plotted on the right. In the next section, experimental results will be presented for some of the mentioned device parameters. As anticipated, *FSR* increases with

decreasing periodicity, Λ (see Fig. 6.2). Note that larger corrugation depth, d, results in greater reflectivity due to a larger change in effective indices between WG_1 and WG_2. This will also result in a slight shift in the resonance wavelength. Experimentally, devices with $\Lambda < 6\ \mu m$ have not yet been successfully fabricated. An optical microscope image can be found in Fig. 6.5 of a device with $\Lambda = 8\ \mu m$, $d = 5.0\ \mu m$ and $L = 4.0\ mm$. The device consists of two symmetric gratings which are coupled to solid-core optical waveguides on either side. These solid-core waveguides carry light to a second microfluidic channel without corrugated sidewalls (the "analyte channel") which can be used to probe fluorescent particles with the on-chip DFB laser.

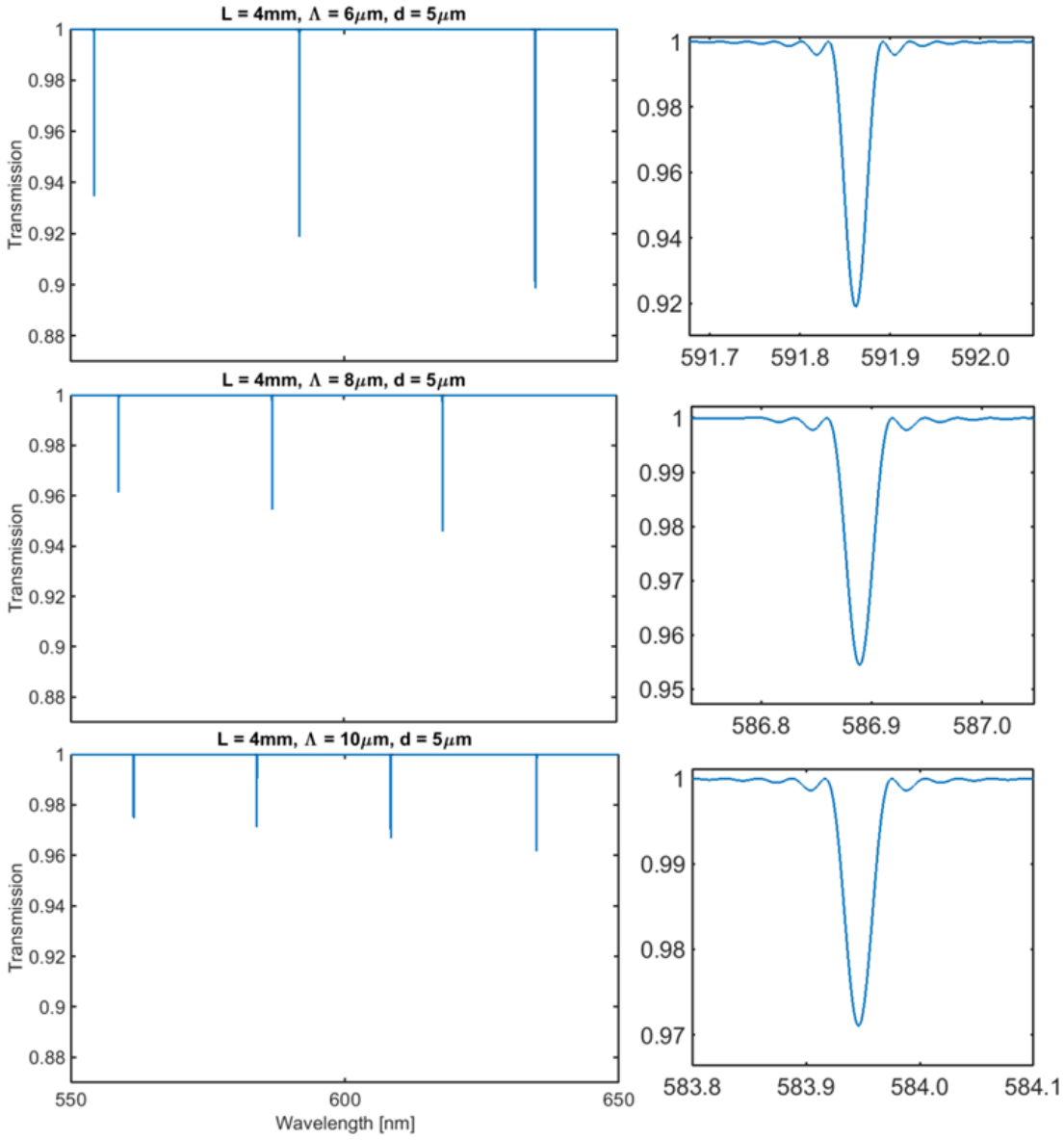

Fig. 6.4 Simulated transmission as a function of wavelength for three different Bragg spacings: $\Lambda = 6, 8$ and 10 μm. All three simulations were performed with corrugation depth of $d = 5\ \mu m$ and length $L = 4mm$. Increasing Λ results in more resonances within the same wavelength span (550 – 650 nm). The resonances become less reflective with increasing Λ. A zoomed-in plot of the relevant resonance for the gain emission spectrum is shown to the right of the full wavelength scans. Between ~ 3 and 8 % reflectivity is found for the simulated designs.

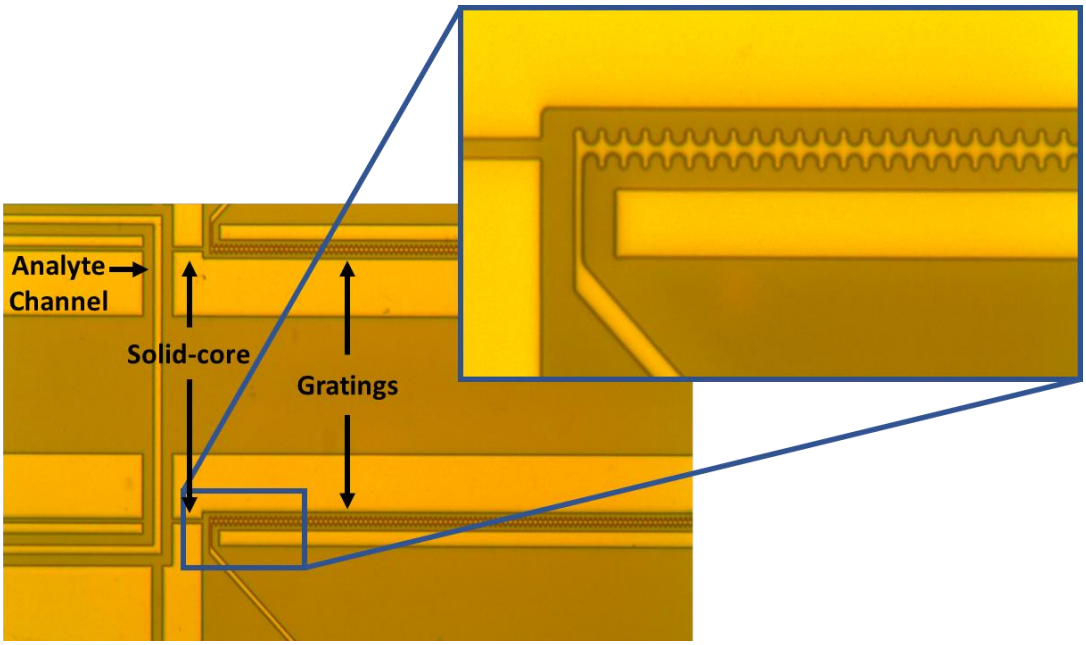

Fig. 6.5 A microscope image of a fabricated device with $\Lambda = 8\ \mu m$, $d = 5.0\ \mu m$ and $L = 4.0\ mm$. Two symmetric grating structures are fabricated on a single chip. The gratings are fabricated in parallel with connecting solid-core optical waveguides to deliver light to a perpendicular analyte channel on the left. To the right of the grating (not imaged), a solid-core optical waveguide is used to guide light to the edge of the device for analysis.

6.2 Results

A cartoon of the experimental setup is found in Fig. 6.6. The devices were fabricated from PDMS as outlined in chapter 3. Devices with varied design parameters have been fabricated ($\Lambda = 6, 8, 10\ \mu m;\ d = 2.5, 5.0\ \mu m$). To test the devices, average output optical powers were measured as a function of average input pump powers and lasing spectra were collected using a spectrometer (Horiba

iHR550). Optical pumping is provided by a passive Q-switched 532 nm source (Teem Photonics Microchip STG-03E-140 with variable repetition rate controller MLC-03A-DP1). The maximum pulse energy is ~ 3 μJ with a temporal pulse width of ~ 500 ns. The laser ("Teem") output profile is shaped using a cylindrical lens such that the pump beam covers the entire microfluidic channel's length to prevent reabsorption by dye outside of the pump beam. After shaping the beam, it is guided to the chip using a mirror. The alignment of the pump beam to the microfluidic channel is monitored from above the chip using a microscope and camera (Andor Zyla sCMOS). As seen in Fig. 6.5, a solid-core optical waveguide is fabricated parallel to the microfluidic DFB structure in order to carry light from the corrugated sidewall microfluidic channel. An optical fiber is coupled to the edge of the chip to collect the output from this solid-core waveguide and is used to guide light to an optical power meter or a spectrometer as seen in Fig. 6.6.

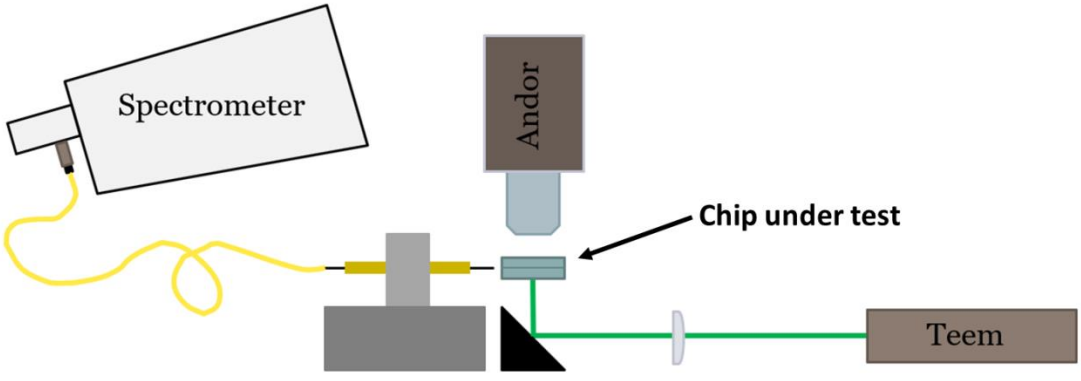

Fig. 6.6 Cartoon of the experimental setup. The pump laser (Teem) operating at 532 nm is shaped using a cylindrical lens. The shaped beam is guided to the chip (blue rectangle) using a mirror below the chip (black triangle). Alignment of the microfluidic channel and pump beam is monitored from above using a microscope and camera (Andor). A solid-core optical waveguide runs from the microfluidic

grating to the edge of the chip where an optical fiber is aligned (using the Andor camera) to collect the output light. This optical fiber is used to guide light to an optical power meter or a spectrometer to measure the average output power and emission spectra, respectively.

Four devices were fabricated and their output powers and emission spectra were collected at varied input pump powers. The devices tested had $\Lambda = 6, 8,$ and $10\ \mu m$. Two $\Lambda = 6\ \mu m$ devices were tested, one with $d = 2.5\ \mu m$ and another with $d = 5.0\ \mu m$. The $\Lambda = 8\ \mu m$ device had $d = 2.5\ \mu m$ and the $\Lambda = 10\ \mu m$ device had $d = 5.0\ \mu m$. All four devices had a grating length, $L = 4\ mm$. The normalized output powers as a function of input pump power show a clear change in slope indicative of lasing as seen in Fig. 6.7. Several data points are linearly fit above and below the input power where the slopes change. The intercept of the two fits is taken as the average threshold pump power (P_T). These fits are seen in the insets of each output vs input power plot in Fig. 6.7. The pump laser beam area ($A \approx \pi \cdot \left(\frac{50\ \mu m}{2}\right) \cdot \left(\frac{4.25\ mm}{2}\right) = 0.0017\ cm^2$) and measured threshold power was then used to approximate the threshold fluence, $F = \frac{Energy}{A} = \frac{1}{A} \cdot \frac{P_T}{RepRate} \approx \frac{P_T}{1.669\ {}^{cm^2}/_{s}}$. The resulting thresholds are summarized in Table 6.2. Experimentally, the device threshold fluences were found to be between 133 and 292 ${}^{\mu J}/_{cm^2}$. Within the literature, for comparable chip-scale DFB dye lasers using R6G, a range of thresholds have been reported for chip-scale DFB dye lasers from tens [80] to thousands [142] of ${}^{\mu J}/_{cm^2}$. Therefore, the presented devices reveal reasonable threshold fluences in comparison with previously reported results.

$\Lambda\ (\mu m)$	$d\ (\mu m)$	Threshold Power (mW)	Threshold Fluence $\left(\mu J/cm^2\right)$
6	2.5	0.488	292
8	2.5	0.295	177
6	5	0.222	133
10	5	0.413	247

Table 6.2 A summary of the experimentally measured threshold powers and fluences for four different device designs (Λ, d as seen in Fig. 6.6 and 6.7).

The lasing spectra are seen in Fig. 6.8. The microfluidic channel dimensions are large enough to sustain multiple modes and therefore multi-mode lasing is not surprising. Additionally, for uniform DFB gratings, there is an anticipated splitting in the lasing modes [85]. A phase shift can be incorporated into the grating design to overcome this degeneracy [76]. In practice however, any unbalanced reflectivity for left and right propagating modes may result in unequal losses for these two modes. The peak emission wavelengths are extracted from the spectra (see Fig. 6.8) and the experimental results are compared with the theoretically anticipated fundamental mode reflectivities as summarized in Table 6.3. The results for periodicities $\Lambda = 8$ and $10\,\mu m$ match the anticipated wavelengths well. However, for $\Lambda = 6\,\mu m$, the expected reflection is at a much higher wavelength. This could perhaps be due to the gain profile not providing much emission at the cavity mode near 591 nm. Additionally, this could explain why the threshold for the $\Lambda = 6\,\mu m; d = 2.5\mu m$ device is higher than for the $\Lambda = 8\,\mu m; d = 2.5\mu m$ device.

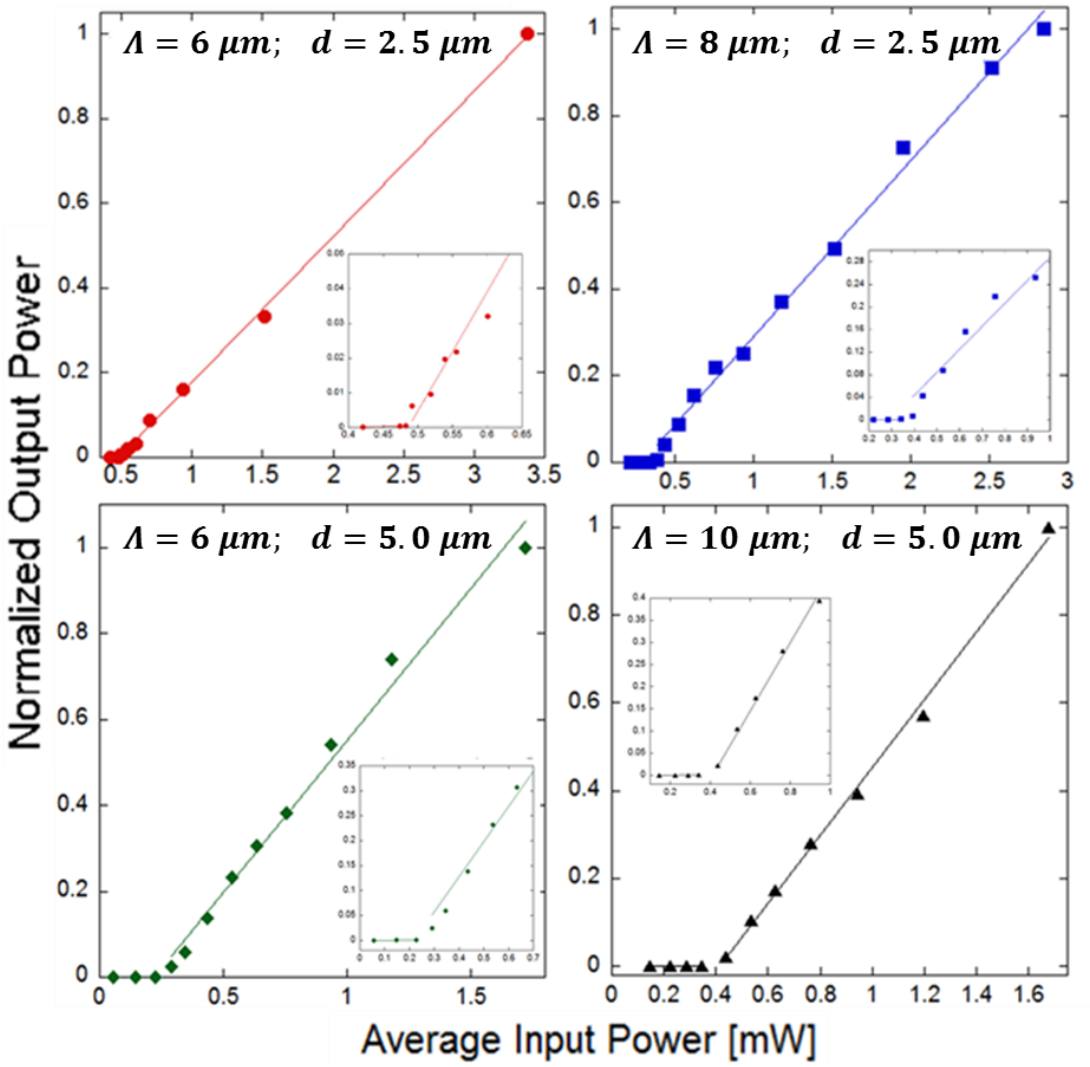

Fig. 6.7 Normalized average output power as a function of average input pump power for four devices. All four devices have a grating length of 4 mm. The emission spectra are collected when 5 mM R6G is dissolved in ethylene glycol. Results for grating depths of $d = 2.5\ \mu m$ and Bragg spacing $\Lambda = 6$ and $8\ \mu m$ are plotted in red and blue, respectively. The results for $d = 5.0\ \mu m$ and $\Lambda = 8$ and $10\ \mu m$ are plotted in green and black, respectively. The linear fits above and below the changing slope are used to fit the threshold pump power (via the fit's intercepts). These threshold powers are used to approximate the threshold fluence as discussed in the text (see Table 6.1).

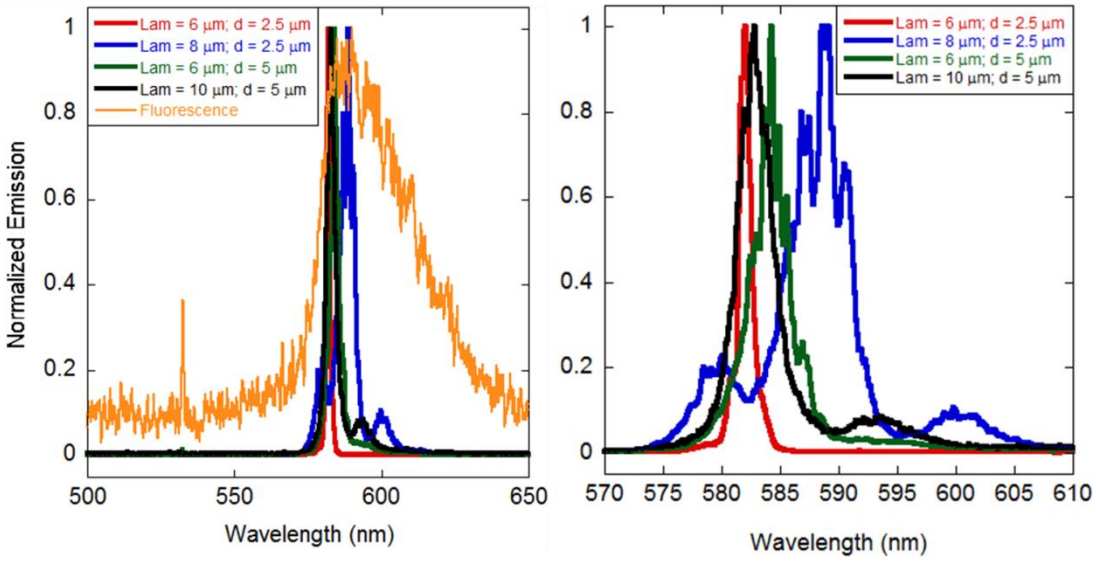

Fig. 6.8 The emission spectra for R6G fluorescence (orange in the left plot) and lasing for the four devices as described in the text. The right plot shows the zoomed-in spectra without fluorescence. The colors match those in Fig. 6.7.

Theoretical Resonance (nm)	591	586	583
Experimental Peak (nm)	581.5 ± 0.5	587.8	580.3
Bragg Spacing, Λ (µm)	6	8	10

Table 6.3 A summary of the experimentally measured peak lasing wavelength (see Fig. 6.7 and the anticipated resonance position from the simulations (see Fig. 6.3)

Thus, lasing has been demonstrated on-chip using a novel corrugated sidewall structure to create distributed feedback. Lasing was demonstrated using a liquid core filled with R6G dissolved in ethylene glycol; however, these devices could be filled with different solvents (or a mixture thereof) to tune the lasing cavity and the number of modes propagating within the structure. Additionally, due to the high m^{th} order structure, various dyes could be used to achieve different color lasing or simultaneous

dual color lasing using a mixture of dyes in a single cavity. Lastly, the integration of a pneumatic layer to the DFB devices could be implemented to create a “lightvalve” [115] which could modulate the output intensity of the laser.

Chapter 7

Summary and Future Work

In conclusion, this thesis has presented several chip-scale optofluidic devices for a variety of applications. First, an all-optical cooling method has was presented which uses an AC Stark shift to compensate for the dynamic Doppler shift [6]. Using this method, two ARROW designs were presented which tailor the intensity profile to provide the appropriate AC Stark shift on-chip for cooling ^{23}Na atoms to final speeds of tens of meters per second. Additionally, experimental slow and stored light was discussed and presented in bulk cell. These techniques could be used to create on-chip photonic devices by integrating multiple atom-filled ARROW waveguides on-chip [7]. Such devices were designed and the fabricated devices demonstrated efficient optical guiding. However, loading the devices with Rb vapor proved challenging and a series of transport studies were carried out to quantify the movement of Rb vapor in tightly confined glass capillaries [131]. These experiments resulted in the design of perforated hollow-core ARROWs on-chip with integrated buried channel solid-core waveguides [132]. The resulting designs demonstrated Rb vapor loading, yielding optical depths up to ~ 0.5 and broad homogeneous linewidths.

Secondly, on-chip biosensing was demonstrated via laser induced fluorescence on two novel all polymer PDMS-based optofluidic devices. Comparable to their ARROW analogues, these devices demonstrated single virus sensitivities. The

optical collection efficiency from chip was enhanced by incorporating hydrodynamic focusing on the device [8]. This is achieved by forcing the fluorescent particles towards the center of a microfluidic channel where the optical collection efficiency is higher. Additionally, a device was presented which demonstrated up to six-fold multiplexing of fluorescent particles using both velocity and spectral discrimination. Three-fold spectral multiplexing was achieved by incorporating a liquid core MMI waveguide to produce different spot patterns for three different wavelengths. Additionally, a novel approach to multiplexing was presented using velocity in a stacked channel design. To do this, a single MMI waveguide spot pattern propagates across two stacked analyte channels which are used to flow particles through the excitation region at different mean speeds. The collected signals are thereby identified by their speed and excitation wavelength [9].

Lastly, a novel PDMS on-chip DFB dye laser was demonstrated using a corrugated sidewall structure. Four different designs comprised of combinations of Bragg spacing ($\Lambda = 6, 8$ and $10\ \mu m$) and corrugation depth ($d = 2.5$ and $5.5\ \mu m$) were fabricated and tested for their lasing threshold. All of the devices had a grating length of $4\ mm$ and were filled with an ethylene glycol solution ($n \approx 1.43$) in which 5 mM of R6G was dissolved. The minimum threshold fluence was found to be $133\ {}^{\mu J}/_{cm^2}$ which is comparable with other reported values for chip-scale lasers of this type. The devices were fabricated in-plane with a perpendicularly intersecting analyte channel which could be used to detect fluorescent particles on-chip. Additional dyes could be incorporated into the channel to produce multi-color lasing

from a single pump laser. Finally, a pneumatic layer can be added to the fabrication procedure [114] in order to control the grating positioning and the transmission of light through the device.

Appendices

Appendix A: Physical Properties of Alkali Atoms

^{23}Na [36]		
Atomic Number		11
Atomic Mass		22.9898u 3.8175×10^{-26} kg
D_1	**Lifetime τ**	16.2992 ns
	Decay Rate (FWHM) Γ	2π(9.765) MHz
	Wavelength λ	508.3325 nm
	Frequency ω	2π(508.3325) THz
	Recoil Velocity v_r	2.9431 cm/s
D_2	**Lifetime τ**	16.2492 ns
	Decay Rate (FWHM) Γ	2π(9.795) MHz
	Wavelength λ	589.1583 nm
	Frequency ω	2π(508.8487) THz
	Recoil Velocity v_r	2.9461 cm/s
^{87}Rb [37]		
Atomic Number		37
Atomic Mass		86.909180520u $1.44316060 \times 10^{-25}$ kg
D_1	**Lifetime τ**	27.70 ns
	Decay Rate (FWHM) Γ	2π(5.746) MHz
	Wavelength λ	794.76569 nm
	Frequency ω	2π(377.1074635) THz
	Recoil Velocity v_r	5.7754 mm/s
D_2	**Lifetime τ**	26.24 ns
	Decay Rate (FWHM) Γ	2π(6.065) MHz
	Wavelength λ	780.241209686 nm
	Frequency ω	2π(384.2304844685) THz
	Recoil Velocity v_r	5.8845 mm/s
^{85}Rb [38]		
Atomic Number		37
Atomic Mass		22.9898u 3.8175×10^{-26} kg
	Lifetime τ	27.679 ns
	Decay Rate (FWHM) Γ	2π(5.7500) MHz

D_1	**Wavelength λ**	794.979014933 nm
	Frequency ω	2π(377.107385690) THz
	Recoil Velocity v_r	5.9113 mm/s
D_2	**Lifetime τ**	26.2348 ns
	Decay Rate (FWHM) Γ	2π(6.0666) MHz
	Wavelength λ	780.241368271 nm
	Frequency ω	2π(384.230406373) THz
	Recoil Velocity v_r	6.0230 mm/s

Appendix B: HC-ARROW Layer Design

The following is the current HC-ARROW design for low loss around the D1 and D2 hyperfine energy levels for Rubidium. The indices and thicknesses are listed from the hollow core outward (six layers). Note that the experimental conformality ratios were used to design the layers. These conformality ratios are also listed for the layers (core outward). If these change, the design will need to change as well. These layers give the loss plots found in Fig. 3.7.

Current Design:

- Top Index

2.05 1.47 2.05 1.47 2.05 1.47 1

- Bottom Index

2.107 1.47 2.107 1.47 2.107 1.47 3.5

- Top Thickness

0.55 0.143 0.085 0.143 0.085 5.92

- Bottom Thickness

0.11 0.184 0.11 0.184 0.11 0.92

- Conformality

1.32 1.69 1.32 1.69 1.32 1.41

Appendix C: Optical Pumping

Optical pumping is an effect where atomic ground state polarization (accumulation of electrons in a particular energy level) is created in the presence of laser light. Optical pumping is a non-linear light-matter interaction and can be useful or detrimental to an experiment. For instance, consider a two level atomic transition between fine states $J = 1$ to $J' = 0$ as seen in Fig. 2.1. Assuming there is no magnetic field present, then the ground state is degenerate with magnetic sublevels $m_J = -1, 0, +1$ [148]. Before an atomic ensemble is illuminated with light, the atoms will have equally distributed ground state levels. Via selection rules, the polarization of the light that excites an electron to the $m_J' = 0$ will determine from what ground state sublevel the electron is moved.

In the case of linearly polarized (π) light, electrons will move from the $m_J = 0$ sublevel (selection rule $\Delta m_J = 0$) as seen in Fig. B.a and if the light is right circularly polarized (σ^+) then electrons will move from the $m_J = -1$ level (selection rule $\Delta m_J = +1$) [148] as seen in Fig. B.b. After excitation, the atoms have equal probability (the decay rate divided by three: $\frac{\Gamma}{3}$) to then decay back to either $m_J = -1, 0, +1$ ground states. Thus, after several cycles of absorption and re-emission, the atoms are depleted from the sublevel connected to the excited state for a particular polarization as seen in Fig. B.c and Fig. B.d. This state is known as a dark state and the light is now allowed to pass by the atom without being absorbed. Note that in

reality there are other mechanisms which will redistribute the atoms to all of the ground state sublevels (e.g. atomic collisions).

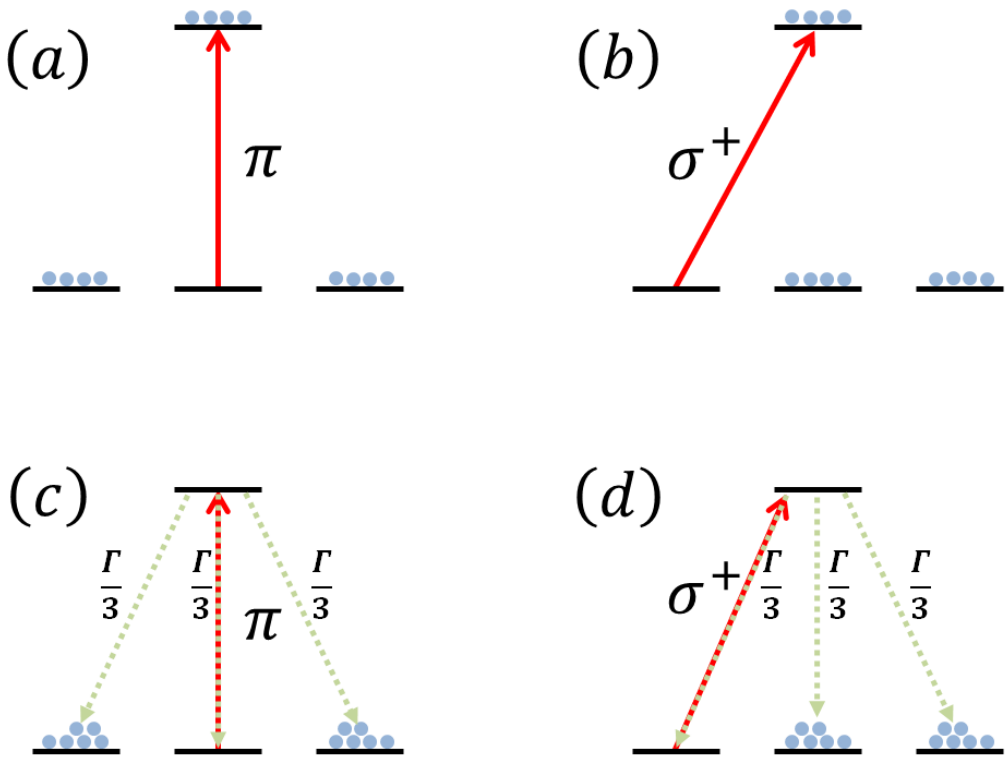

Fig. C: (a) $\boldsymbol{\pi}$ polarized (b) $\boldsymbol{\sigma^+}$ polarized light excites an ensemble of atoms between magnetic fine sublevels according to quantum selection rules. After several cycles, the $\boldsymbol{m_J = 0, -1}$ sublevel is depleted for (c) $\boldsymbol{\pi}$, (d) $\boldsymbol{\sigma^+}$polarized light respectively due to the equal probability ($\frac{\Gamma}{3}$) of the atoms to relax back to any of the sublevels. This creates a so called "dark state" as the light can no longer interact with the atoms.

So, optical pumping can result in dark states in which the atoms can no longer interact with incoming light which may or may not be desirable. This must be carefully considered in any optical experiment. Also, the situation is often much more complicated than the above example. For the hyperfine atomic transitions that we are here considering, the atoms can often decay to a lower ground state from a shared

excited state. In such an experiment, one may consider using a “re-pump” beam. This re-pump would excite the lower and excited state in order to redistribute the population to the upper ground state. Therefore, the lasers and their frequencies used for a particular experiment must be carefully chosen in any optical experiment to prevent unwanted population distribution.

In chapter 4, the optical cooling of ^{23}Na atoms via a Doppler cooling beam and an AC Stark beam was discussed. The relevant hyperfine transitions can be found in Fig. 4.1 (b). However, after re-emission of a photon, the atom can decay not only to the $F = 2$ ground state but also to the $F = 1$ ground state (not shown in Fig. 4.1). Therefore, a re-pump laser beam in the experiment would connect the $F = 1$ ground state with the D_2 $F' = 2$ excited state. This would keep the atoms from evolving into the dark state for the cooling. The power and detuning of this re-pumping beam would need to be properly designed to prevent loss of transverse guiding after each re-pumping event.

Appendix D: Experimental Setup for Slow and Stored Light

The following images were taken of the experimental setup which was used to demonstrate slow and stored light using the lambda energy scheme comprised of the 87Rb isotope in the D1 hyperfine manifold (see Chapter 4). The labelled items in the images are listed below.

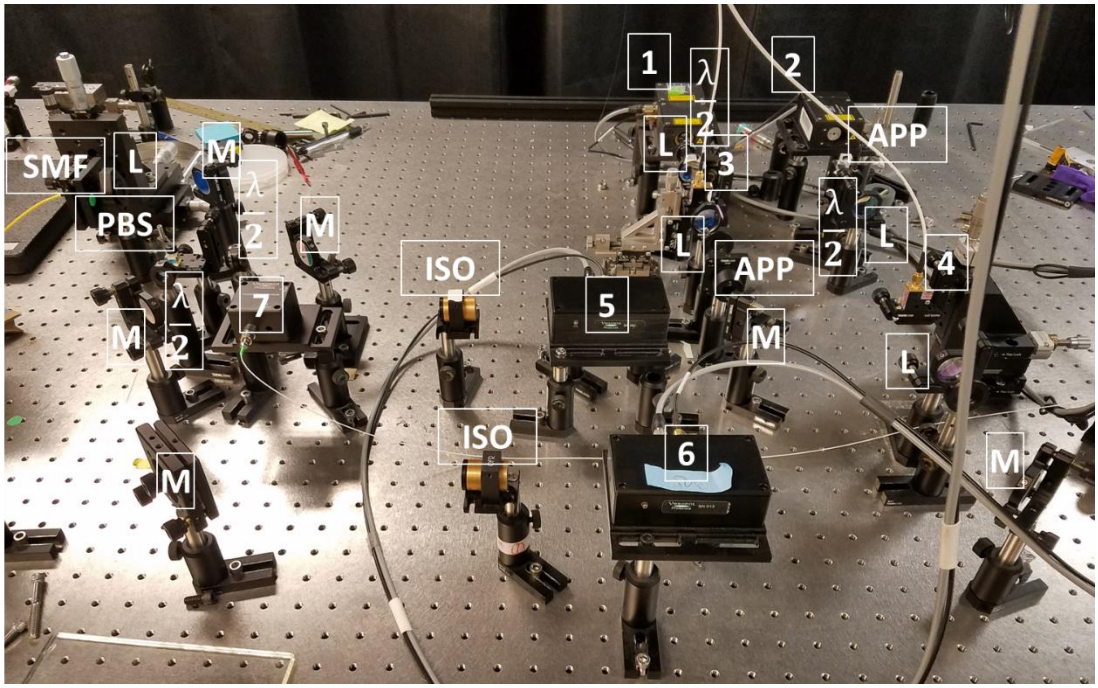

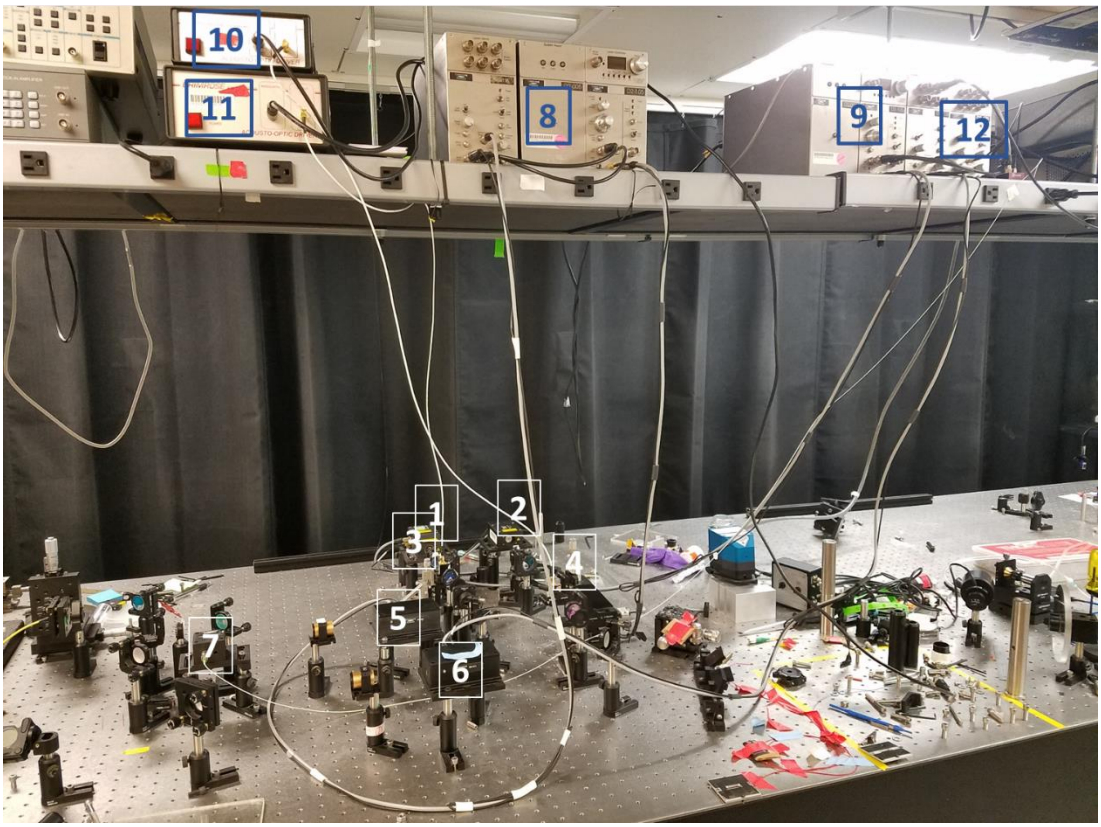

Item list:

- 1) CECL Vescent, 795 nm
- 2) DBR Vescent, 795 nm
- 3) AOM Brimrose, GPM-800-200-780
- 4) AOM Brimrose, GPM-200-50-850
- 5) Spectroscopy module, D2-110 for CECL (1))
- 6) Spectroscopy module, D2-110 for DBR (2))
- 7) Heterodyne module D2-150 offset phase lock servo (OPLS)
- 8) CECL system power, laser servo and controller (via 5))
- 9) DBR system power, laser servo and controller (via 6))
- 10) AOM RF driver for 3) (FFA-200-B1 (5) – F1)

- 11) AOM RF driver for 4) (FFA-800-B1 (200) – F1)
- 12) Offset phase lock servo, Vescent D2-135 for slave laser, 2)
- M) Dielectric mirror
- L) Lens
- λ/2) Half waveplate
- APP) Anamorphic prism pair
- ISO) Optical isolator
- PBS) Polarizing beam splitter
- SMF) Single mode optical fiber

Appendix E: HDF Video Analysis Matlab Script

```
function [ C,t,nu ] = Video_Bead_Analysis(  )
% This script will take in a .tiff video (I converted in Andor
software)
% and go through the frames finding up to 2 beads per frame. The
positions
% in the x-z plane are found as well as a corresponding intensity
found
% from the max point in the frame at the x-z positions (found via a
% gaussian fit). The outputs are:
%
% ---> C: a nx5 matrix with columns = frame no. of bead, time of
beads, x-
% position, z-position and intensities of the beads. If there are
two beads
% in a single frame, there will be a duplicate in the frame no. and
time.
%
% ---> t: the time vector (frame no. * exposure time (for me it's
% 0.009988s). This is the x-axis for the next output....)
%
% ---> nu: The sums of all pixels in each frame. When a bead is
present,
% there is an increase in the sum and this is how we find the
relavent
% frames in which to search for beads. This is the analogue of the
APD
% trace which can be used for cross-correlation with the APD trace
in order
% to assign also velocities from the autocorrelation fits (done
elsewhere).

clear all

DB_V = 0; % double bead conditional to be used later !
DB_H = 0;

%%%%%%%%%%%%%%%%%%%%%%%%%%%%%%%%%%%%%%%%%%%%%%%%%%%%%%%%%%%%%%%%
%___________To Run through the Tiff File_____________
%%%%%%%%%%%%%%%%%%%%%%%%%%%%%%%%%%%%%%%%%%%%%%%%%%%%%%%%%%%%%%%%

uiwait(msgbox('Select appropriate Tiff, Click OK to continue.'));

% Start in the current folder
startingFolder = pwd;

% Get the name of the file that the user wants to use.
defaultFileName = fullfile(startingFolder, '*.*');
[filename,filepath] = uigetfile(defaultFileName, 'Select a file');
fullFileName = fullfile(filepath, filename);
```

```
% Tiff File Properties
InfoImage=imfinfo(fullFileName);
%mImage=InfoImage(1).Width;
%nImage=InfoImage(1).Height;
NumberImages=length(InfoImage);

%%%%%%%%%%%%%%%%%%%%%%%%%%%%%%%%%%%%%%%%%%%%%%%%%%%%%%%%%%%%%%%%%%%%%%%%%%%%%%%
%%%
%_____________________________BackGround and Laser
BackGround__________________
%%%%%%%%%%%%%%%%%%%%%%%%%%%%%%%%%%%%%%%%%%%%%%%%%%%%%%%%%%%%%%%%%%%%%%%%%%%%%%%
%%%

light_starts = 0;

Image_BackGround = imread(fullFileName,1);
[pixelCounts_BackGround , ~] = imhist(Image_BackGround, 256);

p=0; % Laser on threshold. Starts off, p=0
q=1; % Bead present index

% h = waitbar(0,'Please wait...');

   % Find background threshold (while laser off):
    for i=1:20 % 1 to 20 frames as we assume this time has the laser
off...
        f = imread(fullFileName,i); %
        s(i) = sum(sum(f,2),1);
    end

    Back = max(s); % The laser off background is 'Back'

    % %%%%%%%%%%%%%%%%%%
    % The following loop goes through the entire video and finds the
sum of
    % the frames. This should allow us to 1) Find when the laser
turns on
    % and define this threshold, 2) create an APD like trace where
the
    % peaks are frames in which beads are present. We'll take the
resulting
    % trace (nu) and use it below to find the frames where beads
are. Then
    % we'll fit those frames to find the bead positions (in x and z)
as
    % well as their intensites.....

   nbeads=1; % Number of beads index start at 1. Loops below will
increase the
   z=1;
    for i = 1:((NumberImages)/1)
```

```
    %     waitbar(i / (NumberImages-1)/20); % Make a waitbar
        j = imread(fullFileName,i); % Frame i
        [s_j ] = sum(sum(j,2),1); % Sum all the elements o

        if s_j>(1.0025*Back) && p==0 % Finding the laser on time and
index. Might need to tune the background multiplier
            p=1;
            ind_LaserOn = i;
            LonFrame = imread(fullFileName,ind_LaserOn); % Call the
frame in which the laser was found to turn on
            LonH = sum(LonFrame,1); % The histogram for horizontal
direction
            LonV = sum(LonFrame,2); % The histogram for the vertical
direction...
        end

        if s_j>(1.01*Back) && p==1 % higher threshold for a bead and
the laser is on. Might need to tune the background multiplier
           ind(z) = i;
           peak(z) = s_j;
           z = z+1; % This is a vector of the index where the frame
is above a certain
           % amount of background. We expect bead(s) to be in this
frame...
        end
        SUM(i) = s_j;

    end
        locs = ind.*9.988e-3; % Time of bead frames
        t_L_on = ind_LaserOn.*9.988e-3 %time that the laser is
turned on.
        figure(27);plot(linspace(1,numel(SUM),numel(SUM)).*9.988e-
3,SUM,locs,peak,'*')

        model1 = @(p,x) p(1)*exp((-(x - p(3)).^2)/(2*p(2)^2))+p(4);
% Gaussian we'll fit to
        model2 = @(p,x) p(1)*exp((-(x - p(3)).^2)/(2*p(2)^2)) +
p(5)*exp((-(x - p(6)).^2)/(2*p(2)^2)) + p(4); % Gaussianx2 for
fitting doulbe beads
        options=optimset('TolX',0.1e-70);

    for z = 1:numel(ind);
%         z
        frame = imread(fullFileName,single(ind(z))); % Frame for the
found peaks

        % Horizontal Analysis for z-th frame:
        histHraw = sum(frame,1); % Creates a vector along horizontal
direction. Sum the vertical columns
        histH = smoothn(histHraw - LonH); % Subtract laser on
background and then find peaks
```

```
        Hthresh = (max(histH)-min(histH))/5; % Peak if above 25% of
max...?
        x = linspace(1,numel(histH),numel(histH)).*0.55e-6; % x
vector in meter (0.55um/pixel)
%         x = transpose(x);
        [pksH,locsH] = findpeaks(histH,x,'MinPeakHeight',Hthresh); %
Find the peaks for this frame
        figure(39);plot(x,histH)
        hold on


        % Vertical Analysis for z-th frame:
        histVraw = sum(frame,2); % Creates a vector along horizontal
direction. Sum the vertical columns
%         histV = smoothn(histVraw - LonV); % Subtract laser on
background and then find peaks
        histV = histVraw - LonV; % NOTE: sometimes smoothing
eliminates the peak for the vertical sums (narrow peaks)
%         histV = smoothn(histV);
        Vthresh = (max(histV)-min(histV))/5; % Peak if about 25% of
max...?
        y = linspace(1,numel(histV),numel(histV)).*0.55e-6; % x
vector in meter (0.55um/pixel)
        y = transpose(y);
        [pksV,locsV] = findpeaks(histV,y,'MinPeakHeight',Vthresh); %
Find the peaks for this frame
        figure(29);plot(y,histV)
        hold on

        % Convert locs from microns to matrix element for use below:
        fH = single(locsH./0.55e-6);
        fV = single(locsV./0.55e-6);
        [fH_n,fH_m]=size(fH);
        [fV_n,fV_m]=size(fV);

        % index as it is needed....
%%%%%%%%%%%%%% Double beads?
%%%%%%%%%%%%%%%%%%%%%%%%%%%%%%%%%%%%%%%%%%%%%%%%
            if numel(locsV)>=2
%%%%%%%%%%%%% Vertical fits:
%%%%%%%%%%%%%%%%%%%%%%%%%%%%%%%%%%%%%%%%%%%%%%%%
                % Educated guesses:
                qH(1) = 0.75*max(histV); % Amplitude of 1st gaussian
                qH(2) = 1e-6; % STD of 1st guassian (meters)
                qH(3) = locsV(1); % x-offset of 1st guassian from
center
                qH(4) = 0; % y-offset (background)
                qH(5) = 0.75*qH(1); % Amplitude of 2nd gaussian
                qH(6) = locsV(2);  % x-offset of 2nd guassian from
center
```

```
                [finV, RV,JV,CovV,MSEV] =
nlinfit(y,histV,model2,qH,options); % Fit of horizontal histogram
                ciaV = nlparci(finV, RV, 'Jacobian', JV);

                yfV = linspace(y(1),y(numel(y)),1000);
                fitV = model2(finV,yfV);

                DB_V = 1; % Conditional true of double bead in
vertical direction

%                 figure(14); plot(y./1e-6,histV,'*',yfV./1e-
6,fitV);
                hold on
                if numel(locsH)==2

                    DB_H = 1; % Conditional true of double bead in
horizontal direction

                    qH(1) = 0.75*max(histH); % Amplitude of 1st
gaussian
                    qH(2) = 1e-6; % STD of 1st guassian (meters)
                    qH(3) = locsV(1); % x-offset of 1st guassian
from center
                    qH(4) = 0; % y-offset (background)
                    qH(5) = 0.75*qH(1); % Amplitude of 2nd gaussian
                    qH(6) = locsV(2);  % STD of 1st guassian
(meters)


                    [finH, RH,JH,CovH,MSEH] =
nlinfit(x,histH,model2,qH,options); % Fit of horizontal histogram
                    ciaH = nlparci(finH, RH, 'Jacobian', JH);

                    yfH = linspace(x(1),x(numel(x)),1000);
                    fitH = model2(finH,yfH);

%                     figure(15); plot(x./1e-6,histH,'*',yfH./1e-
6,fitH);
                    hold on
                    DB_H = 1;

                        else if numel(locsH) == 1 % So, vertical fit
shows 2 peaks. Horizontal does not (histogram overlap!)

                            % Educated guesses:
                            qH(1) = 0.75*max(histH); % Amplitude of
gaussian
                            qH(2) = 1e-6; % STD ofguassian (meters)
                            qH(3) = locsH(1); % x-offset ofguassian
from center
                            qH(4) = 0; % y-offset (background)
```

```
                            [finH, RH,JH,CovH,MSEH] =
nlinfit(x,histH,model1,qH,options); % Fit of horizontal histogram
                            ciaH = nlparci(finH, RH, 'Jacobian',
JH);

                            yfH = linspace(x(1),x(numel(x)),1000);
                            fitH = model1(finH,yfH);

                            DB_H = 0;

                        end

                    end

                end % End of double bead search and fits....


%%%%%%%%%%%%%% Single bead
%%%%%%%%%%%%%%%%%%%%%%%%%%%%%%%%%%%%%%%%%%%%%%%%%%%%
                if numel(locsV)== 1

                    DB_H = 0; % Conditional false, no doulbe beads.
                    DB_V = 0;

                 %%%%%% Now fit the single beads: %%%%%%%%
                 %%%%%%%%%%%%%%%% Fit of Vertical trace:
%%%%%%%%%%%%%%%%%%%%%%
                    % Educated guesses:
                    qV(1) = 0.75*max(histV); % Amplitude of gaussian
                    qV(2) = 1e-6; % STD ofguassian (meters)
                    qV(3) = locsV(1); % x-offset ofguassian from center
                    qV(4) = 0; % y-offset (background)

                    [finV, RV,JV,CovV,MSEV] =
nlinfit(y,histV,model1,qV,options); % Fit of horizontal histogram
                    ciaV = nlparci(finV, RV, 'Jacobian', JV);

                    yfV = linspace(y(1),y(numel(y)),1000);
                    fitV = model1(finV,yfV);

%%%%%%%%%%%%%%%% Fit of Horizontal trace: %%%%%%%%%%%%%%%%%%%%%%
                    % Educated guesses:
                    qH(1) = 0.75*max(histH); % Amplitude of gaussian
                    qH(2) = 1e-6; % STD ofguassian (meters)
                    qH(3) = locsH(1); % x-offset ofguassian from center
                    qH(4) = 0; % y-offset (background)
```

```
                [finH, RH,JH,CovH,MSEH] =
nlinfit(x,histH,model1,qH,options); % Fit of horizontal histogram
                ciaH = nlparci(finH, RH, 'Jacobian', JH);

                yfH = linspace(x(1),x(numel(x)),1000);
                fitH = model1(finH,yfH);

            end % End of single bead fits.


            %%%%%%%%%%%% NOW we've got to assign all the peak info:
%%%%%%%

            %SINGE BEAD ONLY:
            if DB_V == 0 % This means only a single bead!  (nbeads
increase by 1 only!)
%                 disp('single!')
                % Single bead:
                frameW(nbeads) = (ind(z)); % THe frame where the
bead lives
                timeW(nbeads) = locs(z); % The time at which the
frame arrives in video
                x_W(nbeads) = finV(3); % The x-position of the bead
from fit (above) (Vertical)
                z_W(nbeads) = finH(3); % The z-position of the bead
from fit (above) (Horizontal)
                Int_W(nbeads) = frame(fV(1,1),fH(1,1)); % The
intensity at the bead location (center of fits from above)

                fBr = fV(1,1);
                fBc = fH(1,1);
                nbeads = nbeads + 1; % One bead more!

            end


            % DOUBLE BEAD IN VERTICAL, SINGLE DETECTED IN HORIZONTAL
            if DB_V == 1 && DB_H==0; % This means 2 peaks found
vertical (in x) and only one in z (overlap in histogram)
                % Double bead scenario:
%                 disp('doulbe V; single H')
                % FIRST BEAD: %%%%%%%%%%%%%%%
                frameW(nbeads) = (ind(z)); % THe frame where the
bead leaves
                timeW(nbeads) = locs(z); % The time at which the
frame arrives in video
                x_W(nbeads) = finV(3); % The x-position of the 1st
bead from fit (model2 in Vertical)
                z_W(nbeads) = finH(3); % The z-position of bead from
fit (model1 in Horizontal)
                Int_W(nbeads) = frame(fV(1,1),fH(1,1)); % The
intensity at the 1st bead location (center of fits from above)
```

```
                %%%%%%%%%% SECOND BEAD: %%%%%%
                frameW(nbeads+1) = (ind(z)); % Same frame as above
(2 beads in frame)
                timeW(nbeads+1) = locs(z); % Same as above (again, 2
beads in same frame).
                x_W(nbeads+1) = finV(6); % The x-position of the 2nd
bead from fit (model2 in Vertical)
                z_W(nbeads+1) = finH(3); % The x-position of the
bead from fit (model1 in Horizontal)
                Int_W(nbeads+1) = frame(fV(2,1),fH(1,1)); % The
intensity at 2nd bead location (not, locsH(1)
                % b/c only one peak found in z-direction =
overlapping histogram for beads)
                DBLexamp = z;

                nbeads = nbeads + 2; % Two more Beads!

            end


            % DOUBLE BEAD IN VERTICAL and HORIZONTAL
            if DB_V == 1 && DB_H == 1; % This means 2 peaks found
vertical (in x) and in z
%                 disp('double H & V')
                % Double bead scenario:
                % FIRST BEAD: %%%%%%%%%%%%%%%
                frameW(nbeads) = (ind(z)); % THe frame where the
bead leaves
                timeW(nbeads) = locs(z); % The time at which the
frame arrives in video
                x_W(nbeads) = finV(3); % The x-position of the 1st
bead from fit (model2 in Vertical)
                z_W(nbeads) = finH(3); % The z-position of 1st bead
from fit (model2 in Horizontal)
                Int_W(nbeads) = frame(f(1,1),f(1,1)); % The
intensity at the 1st bead location (center of fits from above)

                %%%%%%%%%% SECOND BEAD: %%%%%%
                frameW(nbeads+1) = (ind(z)); % Same frame as above
(2 beads in frame)
                timeW(nbeads+1) = locs(z); % Same as above (again, 2
beads in same frame).
                x_W(nbeads+1) = finV(6); % The x-position of the 2nd
bead from fit (model2 in Vertical)
                z_W(nbeads+1) = finH(6); % The x-position of the 2nd
bead from fit (model2 in Horizontal)
                Int_W(nbeads+1) = frame(fV(2,1),fH(1,2)); % The
intensity at 2nd bead location in x- and z-direction (H & V)

                nbeads = nbeads + 2; % Two more Beads!
```

```
            end


    end

     nu = SUM;
     t = linspace(1,numel(SUM),numel(SUM)).*9.988e-3;
     numPeaks=numel(ind);
     nbeads;
     numDBL = nbeads-numPeaks;

%     frameSB = imread(fullFileName,single(ind(fSB)));
%     figure(2);imshow(frameSB,[])
%
%     figure(2);histogram((Int_W),100)
%             close(h)

      frame = double(transpose(frameW));
      time = double(transpose(timeW));
      xPos = double(transpose(x_W));
      zPos = double(transpose(z_W));
      Ints = double(transpose(Int_W));

      C = [frame time xPos zPos Ints]; % The results!


end
```

Appendix F: Effective Index Method

Chip-scale waveguides are often rectangular in shape in contrast to circular geometries used for optical fibers. When designing waveguide structures, it is necessary to understand the properties of the guided modes. One important characteristic of a mode is its effective index of refraction (n_{eff}) which is related to a guided mode's propagation constant (β) by:

$$\beta = n_{eff}\frac{\omega}{c}$$

Where ω is the angular frequency of the light and c is the speed of light. To find n_{eff} for a stack of asymmetric dielectrics, one must determine how to solve for β. This three dielectric solution for n_{eff} can be used to approximate n_{eff} for more complex structures (rectangular waveguides) as we will see in Chapter 5. In this section, the approach to solving for n_{eff} in an asymmetric stack of dielectrics is presented. This section follows [119] Chapter 11.2 heavily.

The bedrock of electromagnetism is Maxwell's equations:

$$\vec{\nabla}\cdot\vec{D} = 0 \qquad \vec{\nabla}\cdot\vec{E} = \frac{\rho}{\varepsilon_o} \qquad \vec{\nabla}x\vec{E} = -\frac{\partial\vec{B}}{\partial t} \qquad \vec{\nabla}x\vec{H} = \vec{J} + \frac{\partial\vec{D}}{\partial t}$$

Where $\vec{E}$ and $\vec{B}$ are the electric and magnetic field, ρ and $\vec{J}$ are the charge and current density, $\vec{D}$ and $\vec{H}$ are the electric and magnetic flux densities and are related to $\vec{E}$ and $\vec{B}$ by the following:

$$\vec{D} = \varepsilon_o\vec{E} \qquad\qquad \vec{B} = \mu_o\vec{H}$$

Where ε_o and μ_o are the permittivity and permeability of free space. The wave equation for the electric field can be found by assuming there are no charges present ($\rho = 0$; $\vec{J} = \vec{0}$). The first step involves taking the curl of the third of Maxwell's equations from above:

$$\vec{\nabla} x \vec{\nabla} x \vec{E} = -\vec{\nabla} x \frac{\partial \vec{B}}{\partial t} = -\frac{\partial}{\partial t}\left(\vec{\nabla} x \vec{B}\right) = -\mu_o \frac{\partial}{\partial t}\left(\vec{\nabla} x \vec{H}\right)$$

Recalling our assumption of no charges ($\vec{J} = \vec{0}$) and using the fourth of Maxwell's equations:

$$\vec{\nabla} x \vec{\nabla} x \vec{E} = -\mu_o \frac{\partial^2 \vec{D}}{\partial t^2} = -\frac{1}{c^2}\frac{\partial^2 \vec{E}}{\partial t^2}$$

Where we've used the relationship between ε_o and μ_o and the speed of light (c). Finally, we make use of a vector relationship which surely the reader recalls:

$$\vec{\nabla} x \vec{\nabla} x \vec{E} = \vec{\nabla} \cdot \left(\vec{\nabla} \cdot \vec{E}\right) - \vec{\nabla}^2 \vec{E} = -\vec{\nabla}^2 \vec{E}$$

$$\therefore \vec{\nabla} x \vec{\nabla} x \vec{E} = -\vec{\nabla}^2 \vec{E} = -\frac{1}{c^2}\frac{\partial^2 \vec{E}}{\partial t^2}$$

This is the so-called wave equation because the solutions of which are plane waves. A similar treatment results for the magnetic field by taking the curl of the fourth Maxwell equations above. Now, consider the asymmetric slab structure shown in Fig 2.? in which the refractive index varies along the x-direction. We wish to determine the mode conditions for the structure and we assume that $n_2 > n_1, n_3$. The solution will satisfy the wave equation above with the form:

$$\vec{E}(x,t) = \vec{E}_m(x) e^{i(\omega t - \beta z)}$$

Where we assume monochromatic light (single angular frequency, ω) and β is the propagation constant which is the wave vector component along the z-direction (as discussed in the above section). Running this plane wave solution through the wave equation, we find the following Hemholtz equation in the x-direction (no time dependence):

$$\left[\frac{d^2}{dx^2} + \left(\frac{\omega n}{c}\right)^2 - \beta^2\right]\vec{E}_m(x) = 0$$

This equation is applicable for TE light (TM light has $\vec{H}$ transverse to the x-z plane). For TM light, an analogous Hemholtz equation exists for $\vec{H}_m(x)$. Since $n_2 > n_1, n_3$ then the electric field will be at its maximum where $-d < x < 0$. The wave must decay to positive (negative) x-values when $x > 0$ ($x < -d$). Continuity must exist at the dielectric boundaries for both the fields and their derivatives. To satisfy these conditions, the following piece-wise expression for $\vec{E}_m(x)$ is found:

$$\vec{E}_m(x) = \begin{cases} C \cdot e^{-qx} \;;\; x \geq 0 \\ C\left[\cos(hx) - \frac{q}{h}\sin(hx)\right] \;;\; -d \leq x \leq 0 \\ C\left[\cos(hd) + \frac{q}{h}\sin(hd)\right] e^{p(x+d)} \;;\; x \leq -t \end{cases}$$

Where C is a normalization constant and h, q and p are found by plugging the above equation into the Hemholtz equation:

$$h = \sqrt{\left(\frac{n_2\omega}{c}\right)^2 - \beta^2}$$

$$q = \sqrt{\beta^2 - \left(\frac{n_1\omega}{c}\right)^2}$$

$$p = \sqrt{\beta^2 - \left(\frac{n_3\omega}{c}\right)^2}$$

Using the relevant boundary conditions, the so-called mode condition equation can be found which for a given structure (fixed d, n_1, n_2, n_3) will have solutions for the β. There will exist a set of finite values for β corresponding to available modes which propagate within the structure. Explicitly, at $x = -d$, the derivative of the electric field must be continuous (the derivative of the last two piece-wise $\vec{E}_m(t)$ equations must be equal). This condition leads to:

$$h \cdot \sin(hd) - q \cdot \cos(hd) = p\left[\cos(hd) + \frac{q}{h} si(hd)\right]$$

$$\therefore \tan(hd) = \frac{p + q}{h \cdot \left(1 - {pq}/{h^2}\right)}$$

A similar procedure results in the following TM mode condition equation (where the $\vec{H}_m(x)$ field would instead be considered):

$$\tan(hd) = \frac{h \cdot \left(\frac{{n_2}^2}{{n_3}^2} p - \frac{{n_2}^2}{{n_1}^2} q\right)}{h^2 - \frac{{n_2}^4}{{n_3}^2 {n_1}^2} pq}$$

Both of these equations can be readily solved using computational software. Each solution for β allows the determination of the effective index of refraction, n_{eff}, which again is defined by:

$$\beta = n_{eff} \frac{\omega}{c}$$

As mentioned above, this approach can be used to decompose more complex rectangular waveguide structures in order to approximate the guided mode's effective

index of refraction. In Chapter 5, this approximation will be used to design some on-chip dye lasers.

Bibliography

[1] P. Minzioni *et al.*, "Roadmap for optofluidics," *J. Opt.*, vol. 19, no. 9, p. 093003, 2017.

[2] C. Monat, P. Domachuk, and B. J. Eggleton, "Integrated optofluidics: A new river of light," *Nat. Photonics*, vol. 1, no. 2, pp. 106–114, Feb. 2007.

[3] H. Schmidt and A. R. Hawkins, "The photonic integration of non-solid media using optofluidics," *Nat. Photonics*, vol. 5, no. 10, pp. 598–604, Oct. 2011.

[4] X. Fan and I. M. White, "Optofluidic microsystems for chemical and biological analysis," *Nat. Photonics*, vol. 5, no. 10, pp. 591–597, Oct. 2011.

[5] D. Erickson, D. Sinton, and D. Psaltis, "Optofluidics for energy applications," *Nat. Photonics*, vol. 5, no. 10, pp. 583–590, Oct. 2011.

[6] J. A. Black and H. Schmidt, "Atomic cooling via AC Stark shift," *Opt. Lett.*, vol. 39, no. 3, pp. 536–539, Feb. 2014.

[7] J. A. Black, M. Giraud-Carrier, A. R. Hawkins, and H. Schmidt, "Recent progress in waveguide-based atom photonics," in *Slow Light, Fast Light, and Opto-Atomic Precision Metrology VIII*, 2015, vol. 9378, p. 937803.

[8] J. A. Black, E. Hamilton, R. R. Hueros, J. W. Parks, A. R. Hawkins, and H. Schmidt, "Enhanced Detection of Single Viruses On-Chip via Hydrodynamic Focusing," *IEEE J. Sel. Top. Quantum Electron.*, pp. 1–1, 2018.

[9] Jennifer A. Black, Vahid Ganjalizadeh, Joshua Parks, and Holger Schmidt, "Multi-channel velocity multiplexing of single virus detection on an optofluidic chip," *Opt. Lett.*, vol. (accepted), 2018.

[10] A. C. Menzies, “A Study of Atomic Absorption Spectroscopy,” *Anal. Chem.*, vol. 32, no. 8, pp. 898–904, Jul. 1960.

[11] H. Ito, T. Nakata, K. Sakaki, M. Ohtsu, K. I. Lee, and W. Jhe, “Laser Spectroscopy of Atoms Guided by Evanescent Waves in Micron-Sized Hollow Optical Fibers,” *Phys. Rev. Lett.*, vol. 76, no. 24, pp. 4500–4503, Jun. 1996.

[12] W. C. Stwalley and M. E. Koch, “Alkali Metal Vapors: Laser Spectroscopy And Applications,” *Opt. Eng.*, vol. 19, no. 1, p. 191071, Feb. 1980.

[13] H. Marion *et al.*, “Search for Variations of Fundamental Constants using Atomic Fountain Clocks,” *Phys. Rev. Lett.*, vol. 90, no. 15, p. 150801, Apr. 2003.

[14] G. V. Marr and D. M. Creek, “The photoionization absorption continua for alkali metal vapours,” *Proc R Soc Lond A*, vol. 304, no. 1477, pp. 233–244, Apr. 1968.

[15] L. V. Hau, S. E. Harris, Z. Dutton, and C. H. Behroozi, “Light speed reduction to 17 metres per second in an ultracold atomic gas,” *Nature*, vol. 397, no. 6720, pp. 594–598, Feb. 1999.

[16] D. F. Phillips, A. Fleischhauer, A. Mair, R. L. Walsworth, and M. D. Lukin, “Storage of Light in Atomic Vapor,” *Phys. Rev. Lett.*, vol. 86, no. 5, pp. 783–786, Jan. 2001.

[17] A. L. Bloom, “Principles of Operation of the Rubidium Vapor Magnetometer,” *Appl. Opt.*, vol. 1, no. 1, pp. 61–68, Jan. 1962.

[18] S. L. Cornish, N. R. Claussen, J. L. Roberts, E. A. Cornell, and C. E. Wieman, “Stable ${}^{85}\mathrm{Rb}$ Bose-Einstein Condensates with Widely

Tunable Interactions," *Phys. Rev. Lett.*, vol. 85, no. 9, pp. 1795–1798, Aug. 2000.

[19] T. P. Heavner *et al.*, "First accuracy evaluation of NIST-F2," *Metrologia*, vol. 51, no. 3, p. 174, 2014.

[20] D. B. Pearson, R. R. Freeman, J. E. Bjorkholm, and A. Ashkin, "Focusing and defocusing of neutral atomic beams using resonance-radiation pressure," *Appl. Phys. Lett.*, vol. 36, no. 1, pp. 99–101, 1980.

[21] A. Ashkin, "Acceleration and Trapping of Particles by Radiation Pressure," *Phys. Rev. Lett.*, vol. 24, no. 4, pp. 156–159, Jan. 1970.

[22] A. Ashkin, "Atomic-beam deflection by resonance-radiation pressure," *Phys. Rev. Lett.*, vol. 25, no. 19, pp. 1321–1324, 1970.

[23] A. Imamoğlu, H. Schmidt, G. Woods, and M. Deutsch, "Strongly Interacting Photons in a Nonlinear Cavity," *Phys. Rev. Lett.*, vol. 79, no. 8, pp. 1467–1470, Aug. 1997.

[24] H. Schmidt and A. Imamoglu, "Giant Kerr nonlinearities obtained by electromagnetically induced transparency," *Opt. Lett.*, vol. 21, no. 23, pp. 1936–1938, Dec. 1996.

[25] S. Knappe *et al.*, "Atomic vapor cells for chip-scale atomic clocks with improved long-term frequency stability," *Opt. Lett.*, vol. 30, no. 18, pp. 2351–2353, Sep. 2005.

[26] A. Sargsyan, C. Leroy, Y. Pashayan-Leroy, R. Mirzoyan, A. Papoyan, and D. Sarkisyan, "High contrast <Emphasis

Type="Italic">D</Emphasis><Subscript>1</Subscript> line electromagnetically induced transparency in nanometric-thin rubidium vapor cell," *Appl. Phys. B*, vol. 105, no. 4, pp. 767–774, Dec. 2011.

[27] A. Sargsyan *et al.*, "Hyperfine Paschen–Back regime in alkali metal atoms: consistency of two theoretical considerations and experiment," *JOSA B*, vol. 31, no. 5, pp. 1046–1053, May 2014.

[28] L. Stern, B. Desiatov, I. Goykhman, and U. Levy, "Nanoscale light–matter interactions in atomic cladding waveguides," *Nat. Commun.*, vol. 4, p. 1548, Mar. 2013.

[29] B. Wu, J. F. Hulbert, E. J. Lunt, K. Hurd, A. R. Hawkins, and H. Schmidt, "Slow light on a chip via atomic quantum state control," *Nat. Photonics*, vol. 4, no. 11, pp. 776–779, Nov. 2010.

[30] S. M. Spillane *et al.*, "Observation of Nonlinear Optical Interactions of Ultralow Levels of Light in a Tapered Optical Nanofiber Embedded in a Hot Rubidium Vapor," *Phys. Rev. Lett.*, vol. 100, no. 23, p. 233602, Jun. 2008.

[31] P. S. Light, F. Benabid, F. Couny, M. Maric, and A. N. Luiten, "Electromagnetically induced transparency in Rb-filled coated hollow-core photonic crystal fiber," *Opt. Lett.*, vol. 32, no. 10, pp. 1323–1325, May 2007.

[32] P. S. Light, F. Benabid, G. J. Pearce, F. Couny, and D. M. Bird, "Electromagnetically induced transparency in acetylene molecules with counterpropagating beams in V and Λ schemes," *Appl. Phys. Lett.*, vol. 94, no. 14, p. 141103, Apr. 2009.

[33] A. D. Slepkov, A. R. Bhagwat, V. Venkataraman, P. Londero, and A. L. Gaeta, "Generation of large alkali vapor densities inside bare hollow-core photonic band-gap fibers," *Opt. Express*, vol. 16, no. 23, pp. 18976–18983, Nov. 2008.

[34] E. M. Guild, "Diffusion of Rubidium Vapor through Hollow-Core Fibers for Gas-Phased Fiber-Lasers," AIR FORCE INST OF TECH WRIGHT-PATTERSON AFB OH GRADUATE SCHOOL OF ENGINEERING AND MANAGEMENT, AIR FORCE INST OF TECH WRIGHT-PATTERSON AFB OH GRADUATE SCHOOL OF ENGINEERING AND MANAGEMENT, AFIT/OSE/ENP/11-M01, Mar. 2011.

[35] D. Budker, D. F. Kimball, D. Kimball, and D. P. DeMille, *Atomic Physics: An Exploration Through Problems and Solutions*. Oxford University Press, 2004.

[36] D. A. Steck, "Sodium D Line Data." Dec-2010.

[37] D. A. Steck, "Rubidium 87 D Line Data." Jan-2015.

[38] D. A. Steck, "Rubidium 85 D Line Data." Sep-2013.

[39] W. D. Phillips and H. Metcalf, "Laser deceleration of an atomic beam," *Phys. Rev. Lett.*, vol. 48, no. 9, pp. 596–599, 1982.

[40] M. A. Joffe, W. Ketterle, A. Martin, and D. E. Pritchard, "Transverse cooling and deflection of an atomic beam inside a Zeeman slower," *J. Opt. Soc. Am. B*, vol. 10, no. 12, pp. 2257–2262, Dec. 1993.

[41] K. J. Gunter, "Design and implementation of a Zeeman slower for 87Rb," Ecole Normale Superieure, Paris, 2004.

[42] W. D. Phillips, “Nobel Lecture: Laser cooling and trapping of neutral atoms,” *Rev. Mod. Phys.*, vol. 70, no. 3, pp. 721–741, Jul. 1998.

[43] J. V. Prodan and W. D. Phillips, “Chirping the light—fantastic? Recent NBS atom cooling experiments,” *Prog. Quantum Electron.*, vol. 8, no. 3–4, pp. 231–235, 1984.

[44] W. Ertmer, R. Blatt, J. L. Hall, and M. Zhu, “Laser Manipulation of Atomic Beam Velocities: Demonstration of Stopped Atoms and Velocity Reversal,” *Phys. Rev. Lett.*, vol. 54, no. 10, pp. 996–999, Mar. 1985.

[45] M. Fleischhauer, A. Imamoglu, and J. P. Marangos, “Electromagnetically induced transparency: Optics in coherent media,” *Rev. Mod. Phys.*, vol. 77, no. 2, pp. 633–673, Jul. 2005.

[46] P. Siddons, C. S. Adams, C. Ge, and I. G. Hughes, “Absolute absorption on the rubidium D lines: comparison between theory and experiment,” *J. Phys. B At. Mol. Opt. Phys.*, vol. 41, no. 15, p. 155004, Aug. 2008.

[47] P. L. Knight and P. W. Milonni, “The Rabi frequency in optical spectra,” *Phys. Rep.*, vol. 66, no. 2, pp. 21–107, Dec. 1980.

[48] E. B. Alexandrov *et al.*, “Light-induced desorption of alkali-metal atoms from paraffin coating,” *Phys. Rev. A*, vol. 66, no. 4, p. 042903, Oct. 2002.

[49] K. Nasyrov *et al.*, “Antirelaxation coatings in coherent spectroscopy: Theoretical investigation and experimental test,” *Phys. Rev. A*, vol. 92, no. 4, p. 043803, Oct. 2015.

[50] R. W. Boyd and D. J. Gauthier, “Chapter 6 - ‘Slow’ and ‘fast’ light,” in *Progress in Optics*, vol. 43, E. Wolf, Ed. Elsevier, 2002, pp. 497–530.

[51] I. Novikova, R. l. Walsworth, and Y. Xiao, “Electromagnetically induced transparency-based slow and stored light in warm atoms,” *Laser Photonics Rev.*, vol. 6, no. 3, pp. 333–353, 2012.

[52] M. Fleischhauer and M. D. Lukin, “Dark-State Polaritons in Electromagnetically Induced Transparency,” *Phys. Rev. Lett.*, vol. 84, no. 22, pp. 5094–5097, May 2000.

[53] N. B. Phillips, A. V. Gorshkov, and I. Novikova, “Optimal light storage in atomic vapor,” *Phys. Rev. A*, vol. 78, no. 2, p. 023801, Aug. 2008.

[54] I. Novikova, A. V. Gorshkov, D. F. Phillips, A. S. Sørensen, M. D. Lukin, and R. L. Walsworth, “Optimal Control of Light Pulse Storage and Retrieval,” *Phys. Rev. Lett.*, vol. 98, no. 24, p. 243602, Jun. 2007.

[55] M. Bajcsy, A. S. Zibrov, and M. D. Lukin, “Stationary pulses of light in an atomic medium,” *Nature*, vol. 426, no. 6967, pp. 638–641, Dec. 2003.

[56] G.-B. Lee, C.-C. Chang, S.-B. Huang, and R.-J. Yang, “The hydrodynamic focusing effect inside rectangular microchannels,” *J. Micromechanics Microengineering*, vol. 16, no. 5, p. 1024, 2006.

[57] Y. K. Suh and S. Kang, “A Review on Mixing in Microfluidics,” *Micromachines*, vol. 1, no. 3, pp. 82–111, Sep. 2010.

[58] S.-Y. Teh, R. Lin, L.-H. Hung, and A. P. Lee, “Droplet microfluidics,” *Lab. Chip*, vol. 8, no. 2, pp. 198–220, 2008.

[59] H.-D. Xi *et al.*, “Active droplet sorting in microfluidics: a review,” *Lab. Chip*, vol. 17, no. 5, pp. 751–771, 2017.

[60] G. Testa, Y. Huang, P. M. Sarro, L. Zeni, and R. Bernini, “High-visibility optofluidic Mach–Zehnder interferometer,” *Opt. Lett.*, vol. 35, no. 10, p. 1584, May 2010.

[61] G. Testa, G. Persichetti, P. M. Sarro, and R. Bernini, “A hybrid silicon-PDMS optofluidic platform for sensing applications,” *Biomed. Opt. Express*, vol. 5, no. 2, pp. 417–426, Feb. 2014.

[62] D. Ozcelik *et al.*, “Dual-core optofluidic chip for independent particle detection and tunable spectral filtering,” *Lab. Chip*, vol. 12, no. 19, pp. 3728–3733, 2012.

[63] M. Lee and P. M. Fauchet, “Two-dimensional silicon photonic crystal based biosensing platform for protein detection,” *Opt. Express*, vol. 15, no. 8, pp. 4530–4535, Apr. 2007.

[64] P. S. Nunes, N. A. Mortensen, J. P. Kutter, and K. B. Mogensen, “Photonic crystal resonator integrated in a microfluidic system,” *Opt. Lett.*, vol. 33, no. 14, pp. 1623–1625, Jul. 2008.

[65] W. Z. Song, X. M. Zhang, A. Q. Liu, C. S. Lim, P. H. Yap, and H. M. M. Hosseini, “Refractive index measurement of single living cells using on-chip Fabry-Pérot cavity,” *Appl. Phys. Lett.*, vol. 89, no. 20, p. 203901, Nov. 2006.

[66] A. A. Yanik, M. Huang, A. Artar, T.-Y. Chang, and H. Altug, “Integrated nanoplasmonic-nanofluidic biosensors with targeted delivery of analytes,” *Appl. Phys. Lett.*, vol. 96, no. 2, p. 021101, Jan. 2010.

[67] C. Escobedo, A. G. Brolo, R. Gordon, and D. Sinton, “Flow-Through vs Flow-Over: Analysis of Transport and Binding in Nanohole Array Plasmonic Biosensors,” *Anal. Chem.*, vol. 82, no. 24, pp. 10015–10020, Dec. 2010.

[68] K. Kneipp *et al.*, “Single Molecule Detection Using Surface-Enhanced Raman Scattering (SERS),” *Phys. Rev. Lett.*, vol. 78, no. 9, pp. 1667–1670, Mar. 1997.

[69] S. Nie and S. R. Emory, “Probing Single Molecules and Single Nanoparticles by Surface-Enhanced Raman Scattering,” *Science*, vol. 275, no. 5303, pp. 1102–1106, Feb. 1997.

[70] O. Schmidt, M. Bassler, P. Kiesel, N. M. Johnson, and G. H. Döhler, “Guiding light in fluids,” *Appl. Phys. Lett.*, vol. 88, no. 15, p. 151109, Apr. 2006.

[71] H. Cai *et al.*, “Optofluidic analysis system for amplification-free, direct detection of Ebola infection,” *Sci. Rep.*, vol. 5, p. 14494, Sep. 2015.

[72] D. Yin, D. W. Deamer, H. Schmidt, J. P. Barber, and A. R. Hawkins, “Integrated optical waveguides with liquid cores,” *Appl. Phys. Lett.*, vol. 85, no. 16, pp. 3477–3479, Oct. 2004.

[73] J. Godin, C.-H. Chen, S. H. Cho, W. Qiao, F. Tsai, and Y.-H. Lo, “Microfluidics and photonics for Bio-System-on-a-Chip: A review of advancements in technology towards a microfluidic flow cytometry chip,” *J. Biophotonics*, vol. 1, no. 5, pp. 355–376.

[74] D. Ozcelik *et al.*, “Optofluidic wavelength division multiplexing for single-virus detection,” *Proc. Natl. Acad. Sci.*, vol. 112, no. 42, pp. 12933–12937, Oct. 2015.

[75] D. Ozcelik *et al.*, "Scalable Spatial-Spectral Multiplexing of Single-Virus Detection Using Multimode Interference Waveguides," *Sci. Rep.*, vol. 7, no. 1, p. 12199, Sep. 2017.

[76] Z. Li and D. Psaltis, "Optofluidic dye lasers," *Microfluid. Nanofluidics*, vol. 4, no. 1–2, pp. 145–158, Jan. 2008.

[77] Z. Li, Z. Zhang, T. Emery, A. Scherer, and D. Psaltis, "Single mode optofluidic distributed feedback dye laser," *Opt. Express*, vol. 14, no. 2, pp. 696–701, Jan. 2006.

[78] W. Lee, H. Li, J. D. Suter, K. Reddy, Y. Sun, and X. Fan, "Tunable single mode lasing from an on-chip optofluidic ring resonator laser," *Appl. Phys. Lett.*, vol. 98, no. 6, p. 061103, Feb. 2011.

[79] A. Bakal, C. Vannahme, A. Kristensen, and U. Levy, "Tunable on chip optofluidic laser," *Appl. Phys. Lett.*, vol. 107, no. 21, p. 211105, Nov. 2015.

[80] Z. Li, Z. Zhang, A. Scherer, and D. Psaltis, "Mechanically tunable optofluidic distributed feedback dye laser," *Opt. Express*, vol. 14, no. 22, pp. 10494–10499, Oct. 2006.

[81] W. Song and D. Psaltis, "Pneumatically tunable optofluidic dye laser," *Appl. Phys. Lett.*, vol. 96, no. 8, p. 081101, Feb. 2010.

[82] S. K. Y. Tang *et al.*, "A multi-color fast-switching microfluidic droplet dye laser," *Lab. Chip*, vol. 9, no. 19, pp. 2767–2771, 2009.

[83] H. Chandrahalim and X. Fan, "Reconfigurable Solid-state Dye-doped Polymer Ring Resonator Lasers," *Sci. Rep.*, vol. 5, p. 18310, Dec. 2015.

[84] G. G. Stokes, “XVI. On the change of refrangibility of light.—No. II,” *Philos. Trans. R. Soc. Lond.*, vol. 143, pp. 385–396, Jan. 1853.

[85] Safa O. Kasap and Ravindra Kumar Sinha, *Optoelectronics and photonics: principles and practices*. New Jersey: Prentice Hall, 2001.

[86] L. B. Soldano and E. C. M. Pennings, “Optical multi-mode interference devices based on self-imaging: principles and applications,” *J. Light. Technol.*, vol. 13, no. 4, pp. 615–627, Apr. 1995.

[87] N.-T. Nguyen and S. T. Wereley, *Fundamentals And Applications of Microfluidics*. Artech House, 2002.

[88] Longwell, Paul A, *Mechanics of fluid flow*. New York: McGraw Hill, 1966.

[89] S. Attiya *et al.*, “Design of an interface to allow microfluidic electrophoresis chips to drink from the fire hose of the external environment,” *ELECTROPHORESIS*, vol. 22, no. 2, pp. 318–327.

[90] M. L. Shuler, R. Aris, and H. M. Tsuchiya, “Hydrodynamic Focusing and Electronic Cell-Sizing Techniques,” *Appl. Microbiol.*, vol. 24, no. 3, pp. 384–388, Sep. 1972.

[91] X. Mao *et al.*, “An integrated, multiparametric flow cytometry chip using ‘microfluidic drifting’ based three-dimensional hydrodynamic focusing,” *Biomicrofluidics*, vol. 6, no. 2, p. 024113, Apr. 2012.

[92] J. B. Knight, A. Vishwanath, J. P. Brody, and R. H. Austin, “Hydrodynamic Focusing on a Silicon Chip: Mixing Nanoliters in Microseconds,” *Phys. Rev. Lett.*, vol. 80, no. 17, pp. 3863–3866, Apr. 1998.

[93] X. Mao, S.-C. Steven Lin, C. Dong, and T. Jun Huang, “Single-layer planar on-chip flow cytometer using microfluidic drifting based three-dimensional (3D) hydrodynamic focusing,” *Lab. Chip*, vol. 9, no. 11, pp. 1583–1589, 2009.

[94] T. W. Hänsch, I. S. Shahin, and A. L. Schawlow, “High-Resolution Saturation Spectroscopy of the Sodium D Lines with a Pulsed Tunable Dye Laser,” *Phys. Rev. Lett.*, vol. 27, no. 11, pp. 707–710, Sep. 1971.

[95] T. W. Hänsch, “Repetitively Pulsed Tunable Dye Laser for High Resolution Spectroscopy,” *Appl. Opt.*, vol. 11, no. 4, pp. 895–898, Apr. 1972.

[96] Q. Kou, I. Yesilyurt, and Y. Chen, “Collinear dual-color laser emission from a microfluidic dye laser,” *Appl. Phys. Lett.*, vol. 88, no. 9, p. 091101, Feb. 2006.

[97] S. Balslev and A. Kristensen, “Microfluidic single-mode laser using high-order Bragg grating and antiguiding segments,” *Opt. Express*, vol. 13, no. 1, pp. 344–351, Jan. 2005.

[98] B. S. Kawasaki, K. O. Hill, D. C. Johnson, and Y. Fujii, “Narrow-band Bragg reflectors in optical fibers,” *Opt. Lett.*, vol. 3, no. 2, pp. 66–68, Aug. 1978.

[99] F. X. Kärtner *et al.*, “Design and fabrication of double-chirped mirrors,” *Opt. Lett.*, vol. 22, no. 11, pp. 831–833, Jun. 1997.

[100] N. Matuschek, F. X. Kartner, and U. Keller, “Analytical design of double-chirped mirrors with custom-tailored dispersion characteristics,” *IEEE J. Quantum Electron.*, vol. 35, no. 2, pp. 129–137, Feb. 1999.

[101] S. Wang, “Principles of distributed feedback and distributed Bragg-reflector lasers,” *IEEE J. Quantum Electron.*, vol. 10, no. 4, pp. 413–427, Apr. 1974.

[102] W. Huang, R.M. Shubair, A. Nathan and L. Chow, “The Modal Characteristics of ARROW Structures,” *J. Lighwave Technol.*, vol. 10, no. 8, pp. 1015–1022, 1992.

[103] Pochi Yeh, *Optical waves in layered media*, vol. 61. Wiley-Interscience, 2005.

[104] P. Yeh, A. Yariv, and C.-S. Hong, “Electromagnetic propagation in periodic stratified media. I. General theory,” *J. Opt. Soc. Am.*, vol. 67, no. 4, pp. 423–438, Apr. 1977.

[105] J. C. Knight, T. A. Birks, P. S. J. Russell, and D. M. Atkin, “All-silica single-mode optical fiber with photonic crystal cladding,” *Opt. Lett.*, vol. 21, no. 19, pp. 1547–1549, Oct. 1996.

[106] S. G. Johnson, P. R. Villeneuve, S. Fan, and J. D. Joannopoulos, “Linear waveguides in photonic-crystal slabs,” *Phys. Rev. B*, vol. 62, no. 12, pp. 8212–8222, Sep. 2000.

[107] M. A. Duguay, Y. Kokubun, T. L. Koch, and L. Pfeiffer, “Antiresonant reflecting optical waveguides in SiO2-Si multilayer structures,” *Appl. Phys. Lett.*, vol. 49, no. 1, pp. 13–15, Jul. 1986.

[108] P. Yeh, *Optical waves in layered material*. Wiley-Interscience, 2005.

[109] W. Yang, D. B. Conkey, B. Wu, D. Yin, A. R. Hawkins, and H. Schmidt, “Atomic spectroscopy on a chip,” *Nat. Photonics*, vol. 1, no. 6, pp. 331–335, Jun. 2007.

[110] D. Yin, E. J. Lunt, M. I. Rudenko, D. W. Deamer, A. R. Hawkins, and H. Schmidt, “Planar optofluidic chip for single particle detection, manipulation, and analysis,” *Lab. Chip*, vol. 7, no. 9, pp. 1171–1175, Aug. 2007.

[111] D. Yin, E. J. Lunt, A. Barman, A. R. Hawkins, and H. Schmidt, “Microphotonic control of single molecule fluorescence correlation spectroscopy using planar optofluidics,” *Opt. Express*, vol. 15, no. 12, pp. 7290–7295, Jun. 2007.

[112] D. Ozcelik, H. Cai, K. D. Leake, A. R. Hawkins, and H. Schmidt, “Optofluidic bioanalysis: fundamentals and applications,” *Nanophotonics*, vol. 6, no. 4, pp. 647–661, 2017.

[113] T. Fujii, “PDMS-based microfluidic devices for biomedical applications,” *Microelectron. Eng.*, vol. 61–62, pp. 907–914, Jul. 2002.

[114] G. M. Whitesides, “The origins and the future of microfluidics,” *Nature*, vol. 442, no. 7101, pp. 368–373, Jul. 2006.

[115] J. W. Parks and H. Schmidt, “Flexible optofluidic waveguide platform with multi-dimensional reconfigurability,” *Sci. Rep.*, vol. 6, p. 33008, Sep. 2016.

[116] Z. Cai, W. Qiu, G. Shao, and W. Wang, “A new fabrication method for all-PDMS waveguides,” *Sens. Actuators Phys.*, vol. 204, pp. 44–47, Dec. 2013.

[117] M. A. Ol’Shanii, Y. B. Ovchinnikov, and V. S. Letokhov, “Laser guiding of atoms in a hollow optical fiber,” *Opt. Commun.*, vol. 98, no. 1–3, pp. 77–79, Apr. 1993.

[118] M. J. Renn, D. Montgomery, O. Vdovin, D. Z. Anderson, C. E. Wieman, and E. A. Cornell, "Laser-Guided Atoms in Hollow-Core Optical Fibers," *Phys. Rev. Lett.*, vol. 75, no. 18, pp. 3253–3256, Oct. 1995.

[119] C. A. Christensen *et al.*, "Trapping of ultracold atoms in a hollow-core photonic crystal fiber," *Phys. Rev. A*, vol. 78, no. 3, p. 033429, Sep. 2008.

[120] M. Bajcsy *et al.*, "Efficient All-Optical Switching Using Slow Light within a Hollow Fiber," *Phys. Rev. Lett.*, vol. 102, no. 20, p. 203902, May 2009.

[121] T. Takekoshi and R. J. Knize, "Optical Guiding of Atoms through a Hollow-Core Photonic Band-Gap Fiber," *Phys. Rev. Lett.*, vol. 98, no. 21, p. 210404, May 2007.

[122] M. J. Renn, E. A. Donley, E. A. Cornell, C. E. Wieman, and D. Z. Anderson, "Evanescent-wave guiding of atoms in hollow optical fibers," *Phys. Rev. A*, vol. 53, no. 2, pp. R648–R651, Feb. 1996.

[123] A. D. Slepkov, A. R. Bhagwat, V. Venkataraman, P. Londero, and A. L. Gaeta, "Spectroscopy of Rb atoms in hollow-core fibers," *Phys. Rev. A*, vol. 81, no. 5, p. 053825, May 2010.

[124] V. Venkataraman, P. Londero, A. R. Bhagwat, A. D. Slepkov, and A. L. Gaeta, "All-optical modulation of four-wave mixing in an Rb-filled photonic bandgap fiber," *Opt. Lett.*, vol. 35, no. 13, pp. 2287–2289, Jul. 2010.

[125] M. Ocegueda, E. Hernandez, S. Stepanov, P. Agruzov, and A. Shamray, "Nonstationary coherent optical effects caused by pulse propagation through

acetylene-filled hollow-core photonic-crystal fibers," *Phys. Rev. A*, vol. 89, no. 6, p. 063403, Jun. 2014.

[126] L. Stern, B. Desiatov, N. Mazurski, and U. Levy, "Strong coupling and high-contrast all-optical modulation in atomic cladding waveguides," *Nat. Commun.*, vol. 8, p. 14461, Feb. 2017.

[127] L. Stern, R. Zektzer, N. Mazurski, and U. Levy, "Enhanced light-vapor interactions and all optical switching in a chip scale micro-ring resonator coupled with atomic vapor," *Laser Photonics Rev.*, vol. 10, no. 6, pp. 1016–1022.

[128] R. Ritter *et al.*, "Coupling Thermal Atomic Vapor to Slot Waveguides," *Phys. Rev. X*, vol. 8, no. 2, p. 021032, May 2018.

[129] R. Shankar, *Principles of Quantum Mechanics*, Second. Springer.

[130] I. Novikova, N. B. Phillips, and A. V. Gorshkov, "Optimal light storage with full pulse-shape control," *Phys. Rev. A*, vol. 78, no. 2, p. 021802, Aug. 2008.

[131] M. Giraud-Carrier *et al.*, "Temperature and wall coating dependence of alkali vapor transport speed in micron-scale capillaries," *J. Vac. Sci. Technol. Vac. Surf. Films*, vol. 35, no. 3, p. 031602, Mar. 2017.

[132] M. Giraud-Carrier *et al.*, "Nondiffusive rubidium vapor transport in confined glass channels," *J. Vac. Sci. Technol. A*, vol. 34, no. 3, p. 031602, Apr. 2016.

[133] M. Giraud-Carrier, C. Hill, T. Decker, J. A. Black, H. Schmidt, and A. Hawkins, "Perforated hollow-core optical waveguides for on-chip atomic

spectroscopy and gas sensing," *Appl. Phys. Lett.*, vol. 108, no. 13, p. 131105, Mar. 2016.

[134] S. Liu, T. A. Wall, D. Ozcelik, J. W. Parks, A. R. Hawkins, and H. Schmidt, "Electro-optical detection of single λ-DNA," *Chem. Commun.*, vol. 51, no. 11, pp. 2084–2087, Jan. 2015.

[135] D. D. Carlo, "Inertial microfluidics," *Lab. Chip*, vol. 9, no. 21, pp. 3038–3046, 2009.

[136] D. Magde, E. Elson, and W. W. Webb, "Thermodynamic Fluctuations in a Reacting System---Measurement by Fluorescence Correlation Spectroscopy," *Phys. Rev. Lett.*, vol. 29, no. 11, pp. 705–708, Sep. 1972.

[137] E. Sani and A. Dell'Oro, "Optical constants of ethylene glycol over an extremely wide spectral range," *Opt. Mater.*, vol. 37, pp. 36–41, Nov. 2014.

[138] W. Wang, C. Zhou, T. Zhang, J. Chen, S. Liu, and X. Fan, "Optofluidic laser array based on stable high- Q Fabry–Pérot microcavities," *Lab. Chip*, vol. 15, no. 19, pp. 3862–3869, 2015.

[139] H. Chandrahalim, S. C. Rand, and X. Fan, "Fusion of Renewable Ring Resonator Lasers and Ultrafast Laser Inscribed Photonic Waveguides," *Sci. Rep.*, vol. 6, p. 32668, Sep. 2016.

[140] J. D. Suter, W. Lee, D. J. Howard, E. Hoppmann, I. M. White, and X. Fan, "Demonstration of the coupling of optofluidic ring resonator lasers with liquid waveguides," *Opt. Lett.*, vol. 35, no. 17, pp. 2997–2999, Sep. 2010.

[141] J. C. Galas, J. Torres, M. Belotti, Q. Kou, and Y. Chen, “Microfluidic tunable dye laser with integrated mixer and ring resonator,” *Appl. Phys. Lett.*, vol. 86, no. 26, p. 264101, Jun. 2005.

[142] M. Gersborg-Hansen and A. Kristensen, “Optofluidic third order distributed feedback dye laser,” *Appl. Phys. Lett.*, vol. 89, no. 10, p. 103518, Sep. 2006.

[143] W. Song, A. E. Vasdekis, Z. Li, and D. Psaltis, “Low-order distributed feedback optofluidic dye laser with reduced threshold,” *Appl. Phys. Lett.*, vol. 94, no. 5, p. 051117, Feb. 2009.

[144] C. Peroz, J.-C. Galas, L. Le Gratiet, Y. Chen, and J. Shi, “Compact dye laser on a chip fabricated by ultraviolet nanoimprint lithography,” *Appl. Phys. Lett.*, vol. 89, no. 24, p. 243109, Dec. 2006.

[145] R. F. Kubin and A. N. Fletcher, “Fluorescence quantum yields of some rhodamine dyes,” *J. Lumin.*, vol. 27, no. 4, pp. 455–462, Dec. 1982.

[146] Z. Li, “Optofluidic dye lasers,” phd, California Institute of Technology, 2008.

[147] L. A. Weller-Brophy and D. G. Hall, “Analysis of waveguide gratings: application of Rouard’s method,” *JOSA A*, vol. 2, no. 6, pp. 863–871, Jun. 1985.

[148] M. Auzinsh, D. Budker and S.M. Rochester, *Optically Polarized Atoms*, 1st ed. Oxford University Press, 2010.